VILNIUS UNIVERSITY

Life Sciences Center

Master of Science in Neurobiology, 2nd year student

Arnas KUNEVIČIUS

Master's Thesis

Developing tools to investigate neuronal activity in synaptic pruning

Research supervisor:

Dr. Urtė Neniškytė

Research advisor:

Lina Saveikytė, MSc

Vilnius, 2020

CONTENTS

ABBREVIATIONS

AC – adenylyl cyclase
CA – *Cornu Ammonis*
CamK – calcium/calmodulin-dependent protein kinase
cAMP – cyclic adenosine monophosphate
CA_v – voltage-gated calcium channel
CF – climbing fibers
CNO – clozapine-N-oxide
CRE – cAMP response element
CREB – CRE-binding protein
Cx3cr1 – fractalkine receptor
DA – dentate gyrus
DAG – diacylglycerol
DGC – dentate granule cell
DMSO – dimethyl sulphoxide
DREADD – designer receptor exclusively activated by designer drugs
ER – endoplasmic reticulum
GDP – guanosine diphosphate
GIRK – G protein-gated inwardly rectifying potassium channels
GTP – guanosine triphosphate
Iba1 – ionized calcium-binding adapter molecule 1
IP_3 – inositol triphosphate
MMP – matrix metalloproteinase
Na_v – voltage-gated sodium channel
OHSC – organotypic hippocampal slice cultures
PC – Purkinje cells
PFA – paraformaldehyde
PKA – protein kinase A
PKC – protein kinase C
PLC-β – β-isoform of phospholipase C
PS – phosphatidylserine
SIRPα – signal regulatory protein alpha
SUB – subiculum
Thy1 – thymocyte differentiation antigen 1
TTX – tetrodotoxin

INTRODUCTION

During early postnatal development neurons form more synaptic connections than it is maintained in the mature brain. The elimination of these excess synapses is an essential process for neural circuitry to mature (Park and Poo, 2013a). The primary effector of this process is microglia which exhibit increased phagocytic activity during the period of synaptic pruning (Weinhard et al., 2018). The activity of microglia is mostly determined by specific ligand-receptor interaction between microglia and their target (Li, 2012). However, emerging data suggest that neuronal activity might be the driving force behind the selection of which synapses are going to be removed (Leslie and Nedivi, 2011). Neuronal activity regulates pruning through competition-based mechanism. This results in less active synapses pruned while active ones strengthened (Rivest, 2018). However, mimicking the conditions where a subset of synapses is inhibited and others are relatively more active could simplify the experimental conditions and help to analyze how neuronal activity affect synaptic pruning.

In this study we developed tools and strategies to investigate the role of neural activity in synaptic pruning. We established organotypic hippocampal slice cultures using *Thy1*::EGFP mouse line. It provided an experimental setting for the alteration of neuronal activity *in vitro* using DREADDs and morphological analysis of axonal boutons and dendritic spines. *Thy1*::EGFP, *RC*::LSL-tdTomato, *Cx3cr1*::Cre triple transgene mouse line was developed to analyze active interactions between neurons and microglia. Then, we optimized the conditions of AAV application for the visualization of DREADD-expressing neurons and for the inhibition of their activity by using AAV8/2-CaMKIIα::hM4Di(Gi)-mCherry-WPRE-hgHp(A) DREADD. Finally, we proposed a strategy for morphological analysis of axonal boutons and dendritic spines of neurons inhibited during peak synaptic pruning utilizing co-localization of EGFP and mCherry signals.

AIM AND OBJECTIVES

The aim of this study was to develop tools to investigate the role of neuronal activity in synaptic pruning.

Objectives:

1. To establish organotypic hippocampal slice cultures and to maintain slice viability for sufficient period to investigate synaptic pruning.
2. To visualize neurons, microglia and their interactions utilizing organotypic cultures established using *Thy1*::EGFP, *RC*::LSL-tdTomato, *Cx3cr1*::Cre triple transgenic mouse line.
3. To express AAV8/2-CaMKIIα::hM4Di(Gi)-mCherry-WPRE-hgHp(A) DREADD in a subset of pyramidal neurons and to visualize their axonal boutons and dendritic spines.

1. LITERATURE REVIEW

1.1. Physiological significance of synaptic pruning

The formation of established neuronal connections in the developing brain is considered to be crucial for the consciousness. Neural circuits are established by successive processes that include neuronal process growth, cell migration, target recognition and synaptogenesis (Low et al., 2008). During the early phase of neurogenesis, neurons tend to establish excessive connections. The role of excess primary connections is still to be explained; however, one theory states that it is caused by the limited presence of specific guidance cues (Tillo et al., 2012). Another hypothesis states that exuberant number of synapses encourages activity-dependent pruning and allows competition-driven refinement of developing circuitry (Rubenstein and Rakic, 2013). It has been shown that regressive activity is essential for neural circuit refinement pruning (Park and Poo, 2013b). Additionally, surplus connections could perform significant physiological and structural role during early development and especially during prenatal period (Riccomagno and Kolodkin, 2015). Developmental circuitry refinement includes synapse elimination, dendritic severing, axon and dendrite pruning. All of these mechanisms remove superfluous neuronal material, but preserve parental neuron with its typical signaling (Yu and Schuldiner, 2014). The pruning takes place in most parts of the nervous system, most notably, in the cortex, hippocampus, spinal cord and neuromuscular junction (Schuldiner and Yaron, 2015).

In vertebrates, the removal of excess connections is largely restrained to postnatal development. Humans exhibit the elimination of connections in neural network for the first four to six years after birth and then cortical areas are additionally modified during puberty (Tierney and Nelson, 2009). The process is so intense that about 50% of previously emerged neurons are removed during postnatal growth (Cowan et al., 1984).

The impairment in synaptic pruning was linked to a variety of pathological conditions including schizophrenia, autism spectrum disorders and Alzheimer's disease. Notably, loss of synapses in the mature brain is an indicator for many neurodegenerative diseases (Presumey et al., 2017). More specifically, genome-wide association studies have showed a strong link between immune system specific (*Trem2, CR1, CD33*) and microglia specific (*TYR-OBP*) gene single-nucleotide polymorphisms and the late onset Alzheimer's disease (Hong et al., 2016). Immune system specific markers also are important for

pathogenesis of schizophrenia and loss of grey matter (Mayilyan et al., 2008). Overall, increasing amount of research highlights the significance of synaptic pruning during the development.

1.2. The role of microglia in synaptic pruning

The molecular and cellular mechanisms involved in the remodeling neuronal network are have only be researched for the last few decades. The removal of excess synapses are mediated by microglia, astrocytes, Schwann cells and by neurons themselves through a processes that shares its molecular hallmarks with apoptosis (Eroglu and Barres, 2010). However, due to direct phagocytosis of synaptic terminals, microglia remain the principal cells responsible for neural network formation (Šišková and Tremblay, 2013).

Microglia are a type of glial cells that descended from the myeloid hematopoietic lineage. Microglia colonize the developing CNS and takes a long-lasting residence in the brain (Kettenmann et al., 2011). In the pre-activation state, microglia have ramified morphology and can produce neurotrophic factors, for example, nerve growth factor (NGF), brain derived neurotrophic factor or insulin-like growth factor which induce neurogenesis (Bessis et al., 2007). They also continuously "scan" surrounding environment for signs of any disturbance and migrate to the location of infection or injury where they become activated, clear cellular debris and restructure surrounding cells. Activation of microglia is an intricate multistage process. The transformation from stable ramified to activated amoeboid morphology is achieved by retracting microglial processes and later extending dynamic protrusions for active cell locomotion (Davis et al., 2017). However, the functions of microglia go beyond their immunological duties. Microglia regulate synaptic homeostasis and the concentration of the neurotransmitters in the synaptic cleft highlighting its importance to neuron network function (Wake et al., 2012).

The modification of neuronal network by glial cells has been observed in a number of model systems, ranging from peripheral synapses in the neuromuscular junction to central synapses in the cortex, hippocampus, thalamus and cerebellum. The increase of phagocytic activity during the postnatal development in these locations seems to support microglial role in synaptic pruning (Paolicelli et al., 2011).

The action of microglia seems to be determined by specific ligand-receptor interactions. To simplify, these cues are classified as "eat-me" and "don't eat me" signals (Li.

2012). ”Eat-me” signals enable synaptic material engulfment and/or promote phagocytic activity. Microglial phagocytic receptors are activated by direct interaction with neuronal molecules or through accessory proteins called opsonins (Fu et al., 2014). For example, phosphatidylserine (PS) (one of the essential phospholipid components of plasma membrane) can be recognized by multiple opsonins: milk fat globule EGF factor 8, growth arrest-specific protein 6 or protein S (Fricker et al., 2012; Grommes et al., 2008). Microglial activation by these molecules leads to the changes of cytoskeleton structure and increases phagocytic activity of microglia (Brown and Neher, 2014). On the contrary, transmembrane immunoglobulin superfamily protein CD47directly binds to the signal regulatory protein alpha (SIRPα) receptor located on professional phagocytes and inhibits phagocytosis (Okazawa et al., 2005). These examples show plethora of molecules and their interactions important for synaptic pruning.

However, the interactions of specific molecules on the surface of neurons and microglia do not tell the full story. Emerging research hints that synaptic activity could be the driving force underlying the presentation of molecules on neuronal surface (Wu et al., 2015). For example, the density of displayed CD47 is higher on more active synapses, thus protecting synapses from microglia engulfment in retinal ganglion cells (Lehrman et al., 2018). Also, fractalkine receptor (Cx3cr1) is important for the engulfment and phagocytosis of immature connections in the hippocampus. Reduced microglia engulfment and higher density of dendritic spines in hippocampus CA1 region has been observed in Cx3cr1 knock-out animals (Paolicelli et al., 2011). Paolicelli and colleagues also reported that these excessive connections had immature connectivity with reduced frequency and amplitude of synaptic currents (Paolicelli et al., 2011). Overall, neuronal activity change interactions between neurons and microglia by regulating presented molecules.

1.3. Neuronal activity during the maturation of neural circuits

Neuronal activity is crucial during postnatal development when pruning of neuronal material is the most pronounced. The strengthening or weakening of individual synapses significantly regulate overall circuit organization and function (Leslie and Nedivi, 2011). Synaptic activity is important for the maturation of neural circuits both at the level of single synapse and on that of systemic network. Activity-dependent changes regulate calcium

sensitive proteins which in turn activate different molecular pathways important for synaptic maturation (Fig. 1.1).

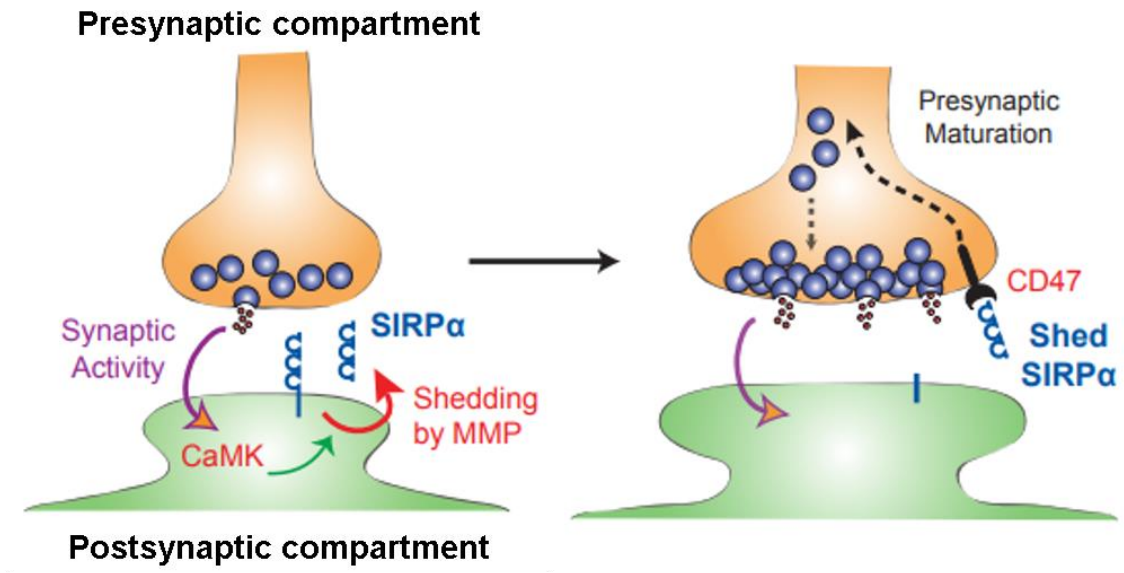

Figure 1.1. Presynaptic neural activity induces SIRPα shedding and interaction with CD47 receptor providing a feedback loop for presynaptic maturation. CamK – Calmodulin kinase. SIRPα – signal regulatory protein alpha (Toth et al., 2013).

Synaptic activity upregulates calcium/calmodulin-dependent protein kinase (CamK) which in turn upregulates matrix metalloproteinase (MMP). MMP mediates the cleavage of the ectodomain of SIRPα and then SIRPα is able to bind CD47 receptor on the presynaptic compartment (Toth et al., 2013). SIRPα$^{-/-}$ mice showed decreased neurotransmitter release, diminished LTP and lower impaired basal transmission (Toth et al., 2013). These findings revealed the significance of neural activity for synaptic maturation at an individual synapse.

Neural activity also has a wider effect on the structure of developing neural networks. For example, activity-dependent synaptic refinement shapes the development of the climbing fibers (CF) in the cerebellum (Hashimoto and Kano, 2013). CFs derive from the inferior olive and continue to Purkinje cells (PC) in the cerebellum. During the prenatal development, every PC is innervated by multiple CFs of comparable strength. However, following the first few weeks after birth, CF go through large-scale axon pruning and synapses formed by the CFs with lower activity are successively eliminated (Watanabe and Kano, 2011). In mature human cerebellum, a winning CF with a particularly high activity secures its entire dendritic tree with a myriad of synapses on the proximal dendrite of the PC. Strong CF easily depolarizes the PC it connects to and triggers the influx of Ca^{2+} ions, thus

ensuring swift and precise signal transmission (Hashimoto et al., 2009a). Neural activity is the prime cause of the CF network sculpting, as demonstrated by the administration of ion channel blockers. For example, CF, inhibited by AMPA receptor blockers, were more actively eliminated. Reduced number of CF remained even in adult rodents (Hashimoto et al., 2011). Moreover, when ordinary activity pattern is changed during early postnatal development by using pharmacological agents or by the overexpression of chloride channel proteins, numerous CFs remain innervating individual PCs (Lorenzetto et al., 2009). Similarly, the deletion of calcium voltage-gated channel subunit alpha 1 (CAv2.1) results in the disruption of CF synapse removal in the primary pruning phase (Hashimoto et al., 2011). Another factor affecting elimination of the CF is the location of the connection. Weaker synapses tend to attach on the soma and are subsequently pruned while stronger connections are more likely to be added on the dendritic tree of PCs. Meanwhile, more powerful dendritic synapses are strengthened even more and weaker somatic connections are removed (Hashimoto et al., 2009b).

Other researchers (Markwardt et al., 2009; Piatti et al., 2011) point to the relevance of inhibition and GABA signaling. This is further supported by the fact that hippocampal progenitor cells establish GABAergic connections before excitatory glutamatergic synapses are formed (Wadiche et al., 2005). Furthermore, during neurogenesis new dentate granule cells (DGCs) display high excitability, and a lower threshold to start long term potentiation. Therefore, immature DGCs are process information in early stages of development (Espósito et al., 2005; Wadiche et al., 2005). On the contrary, during later part of maturation, when functional connectivity increases, the excitability of DGCs decreases. (Laplagne et al., 2007). These findings show that the development of hippocampal synaptic network is regulated by both excitatory and inhibitory activity.

1.4. Methods for the visualization of neuronal activity

The activity of neurons is important for the maturation of the entire neural network. Hence, it is crucial to identify the activity levels of individual synapses. This would allow to investigate whether less active synapses are more preferentially approached by microglia to potentially be removed or modified. Thus, methods designed to visualize the activity of neurons and synapses are in high demand.

Calcium imaging allows to directly measure the activity of both subcellular compartments of individual neuron and the populations of neurons. Calcium is required for the exocytosis of synaptic vesicles in the presynaptic terminal (Neher and Sakaba, 2008). Also, calcium spikes regulate the initiation of activity-dependent synaptic plasticity in the postsynaptic terminal (Zucker, 1999). The earliest calcium indicators were bioluminescent calcium-binding photoproteins, such as aequorin (Shimomura, Johnson, and Saiga 1962). These calcium sensors provided early understanding of activity-dependent neuronal regulation. However, these indicators had poor sensitivity and difficult implementation (Llinas and Nicholson, 1975). Novel calcium indicators have been constructed by fusing calcium-selective chelators with a fluorescent marker. They provide a wide sensitivity range and can to be used in a wide concentration range from 50 nM to 50 μM (Oliver et al., 2000). The variety of calcium indicators (fura-2, indo-1, fluo-3, fluo-4 quin-2, Oregon Green BAPTA, X-rod-1) allows the choice of a wide range of excitation wavelengths (315nm – 615 nm) (Paredes et al., 2008). Furthermore, calcium indicators are divided into single wavelength and ratiometric. Single wavelength calcium indicators display significant changes in fluorescence intensity after binding Ca^{2+} without any changes in the excitation or emission wavelengths (Nicotera and Rossi, 1994). On the other hand, ratiometric calcium indicators exhibit the change in excitation or emission spectra after binding Ca^{2+} (Thestrup et al., 2014). This provides a greater accuracy and avoids any drawbacks of single wavelength indicators such as, the leakage of dye, the changes in cell volume, photobleaching and uneven dye loading (Paredes et al., 2008). High variety of calcium indicators provides accurate and sensitive tool for investigation of neuronal activity.

Another widely used tool for the analysis of neuronal activity is FM dyes. FM dyes (named after their creator Fei Mao) specifically label synaptic vesicles in live samples (Betz and Bewick, 1992). Their unique characteristics are defined by the structural features of the molecule. The tail region of the FM molecule interacts with lipids or other hydrophilic domains. The central region contains two aromatic rings connected by a bridge which form a fluorophore. Finally, the head group has a positive charge and helps the dye to stay inside the vesicle (Gaffield and Betz, 2007). The dye can only leave the synaptic vesicles by exocytosis. Once exocytosed, they quickly diffuse into extracellular space and lose their fluorescence (Richards et al., 2005). FM dyes are non-toxic, stable and dye-loaded vesicles can be released by artificial stimulation of presynaptic terminals (Richards et al., 2000). The main disadvantage of FM dyes is their broad emission spectra. When used with another fluorescent dye this might cause the bleed-through into other emission channels (Gaffield and Betz,

2007). Also, it was reported that FM dyes shifts emission spectrum based on the environment they enter into (Johnson and Betz, 2008). Despite these drawbacks, FM dyes remain one of the most convenient methods for the staining of synaptic vesicles and the only method that displays the capability to visualize the unloading of synaptic vesicles (Kraszewski et al., 1995).

1.5. Methods for the modification of neuronal activity

Changing neuronal activity of could mimic the conditions during synaptic maturation when neurons of different activity compete for incoming connections (Cancedda and Poo, 2008). One of the oldest and well understood tools for the alteration of neural activity are pharmacological agents. Pharmacologically-induced inhibition of neuronal activity has been studied for decades utilizing selective voltage-gated sodium channel (Na_v) blocker tetrodotoxin (TTX) (Sci and 1939). TTX is synthesized by bacteria most commonly located in puffer fish (Miyazawa et al., 1987). The inhibition strength of TTX differs on different subtypes of sodium channels with the most effective inhibition on Na_v 1.1, 1.2, 1.3, 1.6, 1.7 subtypes (Wakita et al., 2015). Also, the location of voltage-gated sodium channels is important for the kinetics of the inhibition. Presynaptic Na_v have faster inactivation kinetics compared to the somatic channels. Besides, presynaptic terminals have high density of these Na_v further facilitating the inhibition of synaptic currents (Engel and Jonas, 2005). All of these properties made TTX one of the most widely used drugs for the inhibition of neuronal activity. However, pharmacological agents are poorly suited for targeted inhibition of neuronal activity since it inhibits all neurons expressing Na_v channels.

On the other hand, optogenetics is a modern technique that allows to control neural activity with high temporal and spatial precision (Lyon, 2013). Optogenetics utilize light-sensitive proteins opsins (transmembrane proteins) that are genetically engineered to be expressed in neurons of interest. Opsins work as light-sensitive ion channels (Boyden et al., 2005). Neurons can be engineered to express opsins by using viral vectors, transgenic knock-in animals or Cre-recombinase based mouse lines. All of these systems enable the expression of an optogenetic construct in a specific neuronal population (Yi Liu et al., 2018). The activity of opsin-expressing neurons can be modified by the illumination with light of specific wavelength. Opsins can induce single or multiple action potentials. The frequency and the pattern of these spikes can be regulated by the wavelength of the opsin-activated light.

Opsins are categorized into two major groups. Type I opsins are found in microbial organisms and consist of a single membrane-bound protein (Oesterhelt and Stoeckenius, 1973). These proteins work as a pump or as an ion channel. Type I opsins remain used mainly due to the ease of genetic engineering and their fast kinetics (Nagel et al., 2003). Type II opsins are found in animal cells and are G protein–coupled receptors. After the activation, they initiate a signaling cascade and subsequently generate slow changes in neural activity (Guru et al., 2015). Both types can effectively alter neuronal activity. However, optogenetic alteration of neuronal activity suffers from multiple disadvantages. Most notably, optogenetic tools synchronize the activity of all targeted neurons. Such synchronization is not physiological as any individual firing patterns are lost (Yizhar et al., 2011). Also, optogenetic inhibitors can force neurons into supra-physiological hyperpolarization, which can result in rebound excitation after the end of inhibition (Kravitz and Bonci, 2013). Finally, non-specific integration of opsins in the cell membrane can cause antidromic activation of neuronal bodies and collaterals (Tye et al., 2011). Overall, optogenetic technique is a useful tool to alter neuronal activity. However, it has number of experimental limitations.

The most recent and very promising technique for the alteration of neuronal activity is designer receptors exclusively activated by designer drugs (DREADD). DREADD-based chemogenetic tools provide the opportunity to both analyze neuron – microglia interactions and to mimic the conditions during the formation of CNS when some synapses are strengthened and others are weakened (Roth 2016). DREADDs circumvent a lot of limitations of optogenetic techniques without the need of the light source for the change in neuronal activity (Vlasov et al., 2018).

DREADDs were developed by the means of directed molecular evolution in genetically engineered yeast by applying small pharmacologically inert molecules to activate G protein-coupled receptors. Originally, human M3 muscarinic receptor was subjected to many trials of selection and mutagenesis. After extensive bioinformatic and pharmacological characterization M3 muscarinic receptor with two pivotal mutations (Y149C, A239G) was selected (Sternson and Roth, 2014). This receptor called hM3Dq is activated by synthetic ligand clozapine-n-oxide (CNO), has relative insensitivity to the native ligand acetylcholine, is absent of any detectable spontaneous activity. Since, previously mentioned mutations are highly conserved in muscarinic receptors in most species, researchers created a plethora of DREADDs (hM1Dq, hM2Di, hM3Dq, hM4Di, hM5Dq) with the variety of molecular effects (Urban and Roth, 2015).

Since DREADDs are the descendants of native GPCRs, they contribute to the same cellular regulatory processes. For example, their activity might be modulated by phosphorylation, internalization, desensitization and other structure-altering molecular modifications (Rajagopal and Shenoy, 2018). Similarly, their mechanism of action is identical to that of the original GPCR. For instance, activating Dq (equivalent to Gq) group (Fig. 1.2 A, B), induces the release of guanosine diphosphate (GDP) and the binding of guanosine triphosphate (GTP) (catalyzed by the guanine nucleotide exchange factor) on G protein α subunit which separates Gαβγ complex into Gαq and Gβγ parts (Trzaskowski et al., 2012). Both segments stimulate β-isoform of phospholipase C (PLC-β), which catalyzes the hydrolysis of phosphatidylinositol biphosphate (Alexander et al., 2009a). The products of this reaction are inositol triphosphate (IP_3) and diacylglycerol (DAG). IP_3 travels through the cytoplasm and binds to specific receptors in the membrane of endoplasmic reticulum (ER). Receptor-ligand interaction opens tetrameric ER Ca^{2+} channels and increases intracellular Ca^{2+} concentration, which modulates other ion channel kinetics and the function of the enzymes. DAG increases the probability for protein kinase C (PKC) to be transported to the cell membrane, which is required to activate it (Gurevich and Gurevich, 2017; Tuteja, 2009). Slightly different molecular pathway applies to the inhibitory group Di (equivalent to Gi) (Fig. 1.2 A, B). In this case, receptor activation Gα is dissociated, but the detached subunit acts through adenylyl cyclase (AC) dependent pathway (Montminy et al., 1990). First, Gα binds to the inhibitory domain of adenylate cyclase and suppress its activity, thus decreasing the generation of cyclic adenosine monophosphate (cAMP) from ATP. Reduced amount of cAMP lower transcription of distinct genes encompassing regulatory cAMP response element (CRE) (van Keulen and Rothlisberger, 2017). In addition, the reduction of cAMP weakens the activity of many phosphorylating kinases, in particular protein kinase A (PKA). Reduced cAMP levels slow down PKA activation and change of conformation to phosphorylate CRE-binding protein (CREB) (Sassone-Corsi, 2012; Yan et al., 2016). Unphosphorylated CREB can't form cAMP-responsive transcription complex, which regulates genes responsible for cell survival, differentiation and survival. The Gβγ complex, disconnected by Gi, activates other inhibitory downstream effectors, especially, G protein-gated inwardly rectifying potassium channels (GIRK). Opening of GIRKs increase concentration of intracellular potassium and hyperpolarize the cell. Finally, activity of GPCRs end when intrinsic GTPase activity of Gα hydrolyze GTP to GDP and Gα-GDP rejoins Gβγ to form Gαβγ (Cooper, 2000).

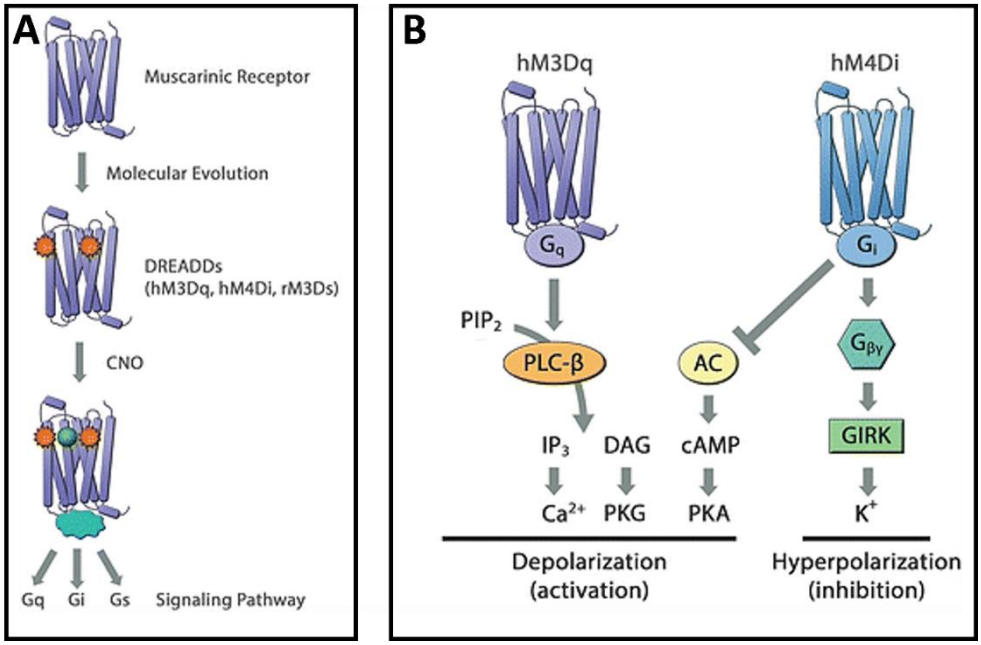

Figure 1.2. The development of DREADDs and their intracellular signaling cascades. A – Muscarinic receptors were evolved to DREADDs that are activated by CNO; B – Molecular pathways involved in the activity of hM3Dq and hM4Di. Adapted from Michaelides and Hurd, 2015 (Michaelides and Hurd, 2015). CNO – clozapine-N-oxide; Gq,Gi,Gs – types of G protein-coupled receptors; IP_3 – inositol triphosphate; PIP_2 – phosphatidylinositol 4,5-bisphosphate; PLC – phospholipase C; DAG – diacylglycerol; AC – adenylyl cyclase; PKA – protein kinase A; cAMP - cyclic adenosine monophosphate; GIRK – G protein-coupled inwardly-rectifying potassium channels.

Different DREADDs utilize different regulatory processes to specifically affect neuronal activity. Activating receptor hM3Dq depolarize the cell increase firing frequency in various neuronal populations throughout central nervous system, including the neurons of raphe, arcuate nuclei and hippocampal CA1 excitatory pyramidal neurons (Atasoy and Sternson, 2018). Activation of hM3Dq in *in vivo* studies show changes in social behavior, feeding, energy expenditure, locomotion and memory (Roth, 2016). On the other hand, inhibiting receptor hM4Di decreases neuron firing, causes modest hyperpolarization and can cause complete neuron silencing. (Agulhon et al., 2013; Scofield et al., 2015). Silencing of neurons is achieved not only by the hyperpolarization by GIRKs but mainly by the inhibition of neurotransmitter release from the presynaptic compartment (Zhu and Roth, 2014).

DREADDs are not affected by neuromediators and are activated by pharmacologically inert drugs. For example, the compound most often used for DREADD activation is CNO which has no native receptors in mice and rats that have not received DREADD treatment (Armbruster et al., 2007). CNO is affected by reverse transformation to

pharmacologically active clozapine that can affect behavior of humans, primates and guinea pigs (Jann et al., 1994). Researchers employ a wide range of doses from 0,5 µM to 200 µM with noticeable electrophysiological effects in acute slices (Pati et al., 2019). Other notable DREADD activating drugs are N-desmethyl-clozapine, salvinorin b, compound 21 and perlapine (Roth, 2016). These chemicals have less pharmacological data and further studies are needed to establish their suitability for DREADD activation.

The expression of DREADDs in a specific population of neurons is ensured using the same methods as in optogenetics. Most widely used targeting system remains viral vectors that ensure good spatial control of expression with relatively low costs (Campbell and Marchant, 2018). Other notable expression systems are tetracycline regulated promoters and Cre-mediated recombination. Using these methods, hM3Dq and hM4Di maintain life-long high levels of expression without any basal behavioral, electrophysiological or anatomical anomalies. (Alexander et al., 2009b; Zhu et al., 2014).

Overall, DREADDs are considered an effective and convenient tool for the alteration of neuronal activity. They are utilized to change the activity of neurons in many different neuronal populations, including the hippocampus (Tuscher et al., 2018). However, further studies are required to develop optimal conditions for DREADD expression and visualization in neurons.

2. MATERIALS AND METHODS

2.1. Materials

The following tables list and specify materials, equipment and software used in this study.

2.1.1. Chemical reagents

Reagents	Manufacturer
AAV8/2-CaMKIIα::Hm4Di(Gi)-mCherry-WPRE-hgHp(A)	Neuroscience Center Zurich
Acetone	Roth
BME (1X)	Gibco
Clozapine N-Oxide (CNO)	Tocris
Clozapine-N-oxide	Tocris
DAPI (4',6-Diamidino-2-Phenylindole, Dihydrochloride)	Sigma-Aldrich
Dimethyl sulphoxide (DMSO)	Roth
Glucose	Sigma-Aldrich
GlutaMAX (100X)	Gibco
Glycine	Sigma-Aldrich
HBSS	Gibco
HEPES	Gibco
Horse Serum	Gibco
MEM (10X)	Gibco
Mowiol	Calbiochem
Normal Donkey Serum	Abcam
Normal Goat Serum	Abcam
Paraformaldehyde (PFA)	Sigma-Aldrich
PBS tablets pH 7.4	Sigma-Aldrich
Penicillin/streptomycin (100X)	Gibco
Sodium azide	Merck Group
Sodium bicarbonate ($NaHCO_3$)	Roth
Sodium Chloride (NaCl)	Roth

Sodium Hydroxide (NaOH)	Roth
TRIS-HCl	Roth
Triton X-100	Merck

2.1.2. Media, buffers and solutions

Name	Composition
Dissection medium	Penicillin/streptomycin (100X) 1 %, HEPES 15 mM, glucose 0.5 % in HBSS filtered after.
Maintaining medium	BME (1X) 25 %, horse serum 25 %, MEM (10X) 5 %, penicillin/streptomycin (100X) 1 %, GlutaMAX 2 mM, glucose 0.65 %, sodium bicarbonate 9 mM in ddH_20 and filtered after.
PB 0.4 M	16.1 g/l KH_2PO_4, 56.8 g/l Na_2HPO_4 in ddH_20.
PFA 4%	PFA 4%, 0.1 M PB, 50ml ddH_2O.
PFA 8%	8 g PFA added drop wise NaOH (stock 1 M) to dissolve, adjusted to 100 ml with ddH_2O, drop wise HCL adjusted pH to 7,2 – 7,4.
Triton-X/PBS	0,5 % of Triton-X slowly added into PBS while mixing.
Clozapine-N-oxide	CNO 20 mM in DMSO

2.1.3. Mouse lines

Genotype	Description	Reference
Thy1::EGFP	*Thy1*:EGFP mouse line has *Thy1* promoter region required for neuronal expression of EGFP in excitatory pyramidal neurons in the hippocampus	JAX Nº 003709
Thy1::EGFP *Cx3cr1*::Cre *RC*::LSL-tdTomato	Triple transgene mouse line with EGFP labeled excitatory pyramidal neurons in the hippocampus and tdTomato labeled microglia. Density of the labeling is controlled by estrogen receptor agonist tamoxifen. Expression of Cre recombinase is under control of fractaline promoter Cx3Cr1. When *Cx3cr1*::Cre mice are bred with mice containing floxed sequence its offsprings will have the floxed sequence removed.	JAX Nº 003709 006148 007905

	This mice line contains *Rosa-CAG*-LSL-tdTomato-WPRE conditional allele. When bred with mouse containing Cre recombinase, emerging pups will have STOP fragment removed in Cre expressed tissues and will start expressing tdTomato.	

2.1.4. Consumables

Name	Manufacturer
Double-sided stainless-steel blades	Personna
6-well cell culture plates	Costar
24-well cell culture plates	Costar
Coverslips (24x60mm)	Roth
Dick Blick Wonder White brush	Dick Blick
Sharp surgical forceps	ThermoScientific
Bent surgical forceps	ThermoScientific
Narrow end surgical scissors	ThermoScientific
Microscope slides (76x26mm)	Roth
Multi®SafeSeal® Tubes, 1.7ml, natural	Roth

2.1.5. Equipment

Name	Manufacturer
McILWAIN Tissue Chopper	The Mickle Laboratory Engineering Co.LTD
Leica EZ4 stereoscopic microscope	Leica
Microprocessor pH Meter	Hanna Instruments
Horizontal shaker	ThermoScientific
Peristaltic pump	ThermoScientific
EVOS FL Auto Live Cell Imaging System	ThermoScientific
Leica TCS SP5 Confocal microscope	Leica

2.1.6. Software

Name	Manufacturer
Microsoft office	Microsoft Inc.
LAS AF	Leica
ImageJ version 1.52p	NIH Image
GraphPad Prism6	GraphPad Software

2.1.7. Antibodies

Name	Manufacturer
Polyclonal rabbit Anti-RFP (N° 600-401-379)	Rockland
Polyclonal goat Alexa Fluor 568 (N° A11011)	Invitrogen

2.2. Methods

2.2.1. Organotypic hippocampus slice culture

Organotypic hippocampal slice cultures (OHSC) were prepared using three day old mouse pups. Before dissection, number of preparations were done. First, cell culture membranes were placed in the 6-well plates using sterile forceps. Specific OHSC maintaining medium (preparation described in chapter 2.1.2.) was added to the plates and plates were placed in 35 °C 5% CO_2 incubator. Dissection was performed with 4 pairs of sharp forceps, dissection spatula, a pair of curved tweezers, scalpel, sharp dissection scissors and a Dick Blick Wonder White brush. All metal tools were sterilized using autoclave at 121 °C and 311 kPa for 40 min. Before the experiment, the brush was kept in 70 % ethanol for 5 min, air dried and kept in HBSS during the procedure. 150 mm petri dish was filled with ice to get a cool working surface. Isolated brain and hippocampi were always kept in ice cold dissection medium (preparation described in chapter 2.1.2.). Hippocampi were sliced with McIlwain tissue chopper. Before using the chopper, its blade was washed for 5 min in acetone followed by 2 min in 99% ethanol and finished by 2 min in 70% ethanol.

Procedure started with cervical dislocation, followed by decapitation. Then, head was placed into a 60 mm Petri plate, sprayed with ethanol and moved into the flow cabinet for all following procedures. Before continuing the preparation, gloves were changed which ensured

sterility. Petri dish with mouse head was placed on ice and dissection was started by inserting one pair of sharp forceps into the eye sockets of the pup to achieve stable fixation of the head. Another pair was used to remove skin and skull (which at this point is only a thin layer of cartilage). The skull was removed by a gentle low angle puncture of the skull at the midline and then turning horizontally towards periphery. After exposing the brain, it was extracted by gently placing dissection spatula at the bottom of skull cavity. Isolated brain was placed in a new 60 mm Petri dish filled with ice cold dissection medium. Next, brain was placed on the ventral surface and from the superior view incisions were made between the hemispheres and in the space of transverse sinus just above the superior colliculus. Cuts were made in a bent coronal manner to reduce the amount of midbrain tissue covering hippocampus. Cut hemispheres were placed on a ventral surface. Hippocampal site was located on the medial side of the hemisphere.

Next, meninges and blood vessels were removed using bent sharp forceps. After that, hippocampus was rolled out using curved forceps and entorhinal cortex was nipped of. After both hippocampi were removed, they were moved onto the platform of the McIlwain tissue chopper. The tissue was sliced into 300 μm slices using 50 strokes/min slicing speed and setting "1" for blade force. Slices were delicately collected from the cutting surface using the brush and moved back to the dissection medium. Then, slices were examined for any signs of damage. Cuts with damage to CA1, CA3 or dentate gyrus were immediately rejected. Intact slices were carefully planted on previously prepared cell culture inserts with maintaining medium in a 6-well plate. One cell culture insert was sufficient to place 6 – 8 slices. Medium was changed 24 h after the planting and every 2-3 days during culture maintenance. OHSC were maintained in an incubator at 35 °C with 5% CO_2.

2.2.2. Fixation, staining and mounting of organotypic slices

Before fixation 4% PFA 0,1 M PB solution was made (preparation described in chapter 2.1.2.). Fixation was performed in the fume hood to avoid the exposure to PFA. 3 ml of 4% PFA was added to each well with cell culture inserts (2 ml on the bottom of the well and 1 ml into the insert itself) to submerge the slice and incubated in the RT for 30 min. During this step it was crucial to keep the plate still because any movement can disrupt tissue polymerization caused by the PFA. Next, slices were washed once with PBS followed by a 2-time wash with 30 mM Glycine/PBS for 15 min (3 ml into all wells). Finally, slices were

washed twice with PBS for 15 min. Every step of the washing was performed using a horizontal shaker. After fixing, cell culture inserts were placed on a dark surface to carefully cut out individual slices and placed in individual wells into a 24-well plate. Samples were kept in PBS/Sodium azide solution at 4 °C until further staining.

Slices were stained with DAPI fluorescent staining to visualize the structure and distribution of cells within the slices. DAPI has high affinity to adenine – thymine rich regions of the DNA and is widely used for nuclear staining (Jang et al., 2018). Each slice was treated with 0,5 ml of 0,1% DAPI and incubated for 15 min at RT on the horizontal shaker. From now on, slices had to be protected from light to maintain fluorescent signal. After incubation, samples were washed 3 times for 15 min using PBS on horizontal shaker. Slices were kept in PBS/Sodium azide solution at 4 °C, in the dark until further notice.

Immunofluorescent staining was performed utilizing the following protocol:

1. Blocking and permeabilization:

Slices were placed into a 24-well cell culture plate (up to 4 slices per well). 500 µl of permeabilization buffer, consisting of 400 µl 0,5% Triton-X/PBS (preparation described in chapter 2.1.2.) and 100 µl of normal goat serum was pipetted in to the well. Slices were incubated in the buffer for 16 h on a shaker at 4 °C.

2. Incubation with primary antibodies:

After the permeabilization, slices were incubated in 250 µl of primary antibody solution for 24 h on a shaker at 4 °C. Primary antibody solution consisted of 185 µl PBS, 50 µl 0,5% Triton-X/PBS, 12,5 µl normal goat serum and 2,5 µl primary rabbit polyclonal anti-RFP antibodies (dilution 1:100). After the incubation slices were washed three times using 1 ml of PBS per well for 15 min each wash.

3. Incubation with secondary antibodies:

Next, slices were incubated in 250 µl of secondary antibody solution for 4h at RT. Solution consisted of 237 µl PBS, 12,5 µl normal goat serum, 0,625 µl secondary goat polyclonal Alexa Fluor 568 antibodies (dilution 1:400). After incubation slices were washed three times using 1ml of PBS per well for 15min each wash.

Slices were mounted onto the microscope slides for confocal microscopy. First, MOWIOL solution was prepared using procedure described in chapter 2.1.2. Slices were placed on the microscope slides and were left to air dry (drying is over when membrane that slice resides on turns completely white). 5 µl drop of MOWIOL was applied on the dried slice using a 200 µl pipette tip (it was important to prevent the formation of bubbles). One microscope slide usually supported up to 8 samples. Dried slices covered with MOWIOL

were covered with a coverslip and left to dry for 24 h in the dark at RT. Later, samples were stored at 4 °C.

2.2.3. OHSC treatment with AAV-hM4D construct and DREADD activation by CNO

OHSC were treated with AAV8/2-CaMKIIα::Hm4Di(Gi)-mCherry-WPRE-hgHp(A) construct to establish experimental conditions in which neuron activity could have been inhibited. DREADD was administered at various time points (DIV 1, 5, 7, 12). Different concentrations (9 x 10^8 vg, 3,6 x 10^8 vg, 1,8 x10^8 vg) were tested. 1 µl of AAV-hM4D was applied on top of each slice. Medium was changed 2 days after infection. Later medium was changed as usual, every 2-3 days.

After hM4D DREADD expression CNO was administered to OHSC to inhibit hM4D-mCherry expressing neuron activity. CNO was mixed with pre-warmed maintaining medium to obtain 10 µM CNO concentration. 1.2 ml of this mixture was added under culturing membrane and additional 10 µl drop was added on top of each OHSC. Medium was changed to the maintaining medium after 24 h.

2.2.4. Imaging of OHSC using EVOS live imaging system

EVOS® FL Cell Imaging System was used to monitor *Thy1* mediated EGFP expression in pyramidal neurons, OHSC viability, neuronal network development and AAV-hM4D fluorescence in organotypic slices. EGFP signal labelled excitatory pyramidal hippocampal neurons and mCherry signal allowed to detect hM4D-mCherry-expressing neurons.

EVOS® FL Cell Imaging System utilizes light-emitting diode to provide multi-channel fluorescence imaging. For all acquired images 10× magnification objective was used. Visualization of EGFP-expressing excitatory pyramidal neurons was obtained using light cube providing excitation at 459 – 481 nm wavelenghts at following parameters: light intensity – 45, exposition – 137 ms, gain – 1.6. For EGFP signal 500 – 550 nm wavelenght emision was registered. hM4D-mCherry expressing neurons were imaged using light cube providing excitation at 570 – 599 nm wavelght range using following parameters: light

intensity – 45, exposition – 1100 ms, gain – 7. For mCherry signal 612 – 644 nm wavelenght emision was registered. Base settings for all imaging were set to: brightness – 63, contrast – 58. Different imaging parameters were used to acquire high-detail images of both EGFP and mCherry fluorescence signals and to accomodate for the fact that quantum yield and fluorescence intensity of mCherry are much lover compared to EGFP (Shaner et al., 2005).

2.2.5. Imaging of OHSC using confocal fluorescent microscopy

Confocal imaging was performed on the Leica TCS SP5 confocal microscope with 63×/1.4 oil immersion objective. DAPI staining was visualized using 405 nm diode laser at 20% power. Emission was registered at 415 nm – 460 nm wavelengths. DAPI stained nuclei were imaged using 1.7× optical zoom (pixel size 141×141 nm^2).

EGFP-expressing neuron images were acquired using argon diode laser with 488 nm excitation wavelength at 20% power. Emission was registered at 500 – 550 nm wavelengths. Neuron soma was imaged with 1.7× optical zoom (pixel size 141×141 nm^2) while axonal boutons and dendritic spines were imaged using 5× optical zoom (pixel size 46×46 nm^2) with z-axial step size 118 nm.

hM4D-mCherry-expressing neurons were imaged using diode pumped solid state (DPSS) laser with 561 nm excitation wavelength. Emission was registered at 570 – 630 nm wavelengths. Neuron soma was imaged with 1.7× optical zoom (pixel size 141×141 nm^2) while dendrites with 5× (pixel size 46×46 nm^2) and z-axial step size 118 nm.

tdTomato-expressing microglia were imaged using DPSS laser with 561 nm excitation wavelength. Emission was registered at 570 – 650 nm wavelengths. Microglia was imaged with 1.7× optical zoom (pixel size 141×141 nm^2) and z-axial step size 118 nm.

2.2.6. Image analysis

Analysis of images was performed using ImageJ version1.52p software.

2.2.6.1. Analysis of images acquired on EVOS live imaging system

Background from images with mCherry signal was subtracted using Process>Subtract background>Set rolling ball radius to 50 pixels. mCherry signal grey values were represented from 0 to 40 using Brightness and contrast>Set>Min:0, Max:40 (8 bit format images).

2.2.6.2. Protocol for counting tdTomato-expressing microglia

tdTomato-expressing microglia were counted using the following protocol:

1. Image background was subtracted to reduce background noise and to ensure better segmentation of individual cells (Fig. 2.1.) using Process>Subtract background>Set rolling ball radius to 50 pixels.

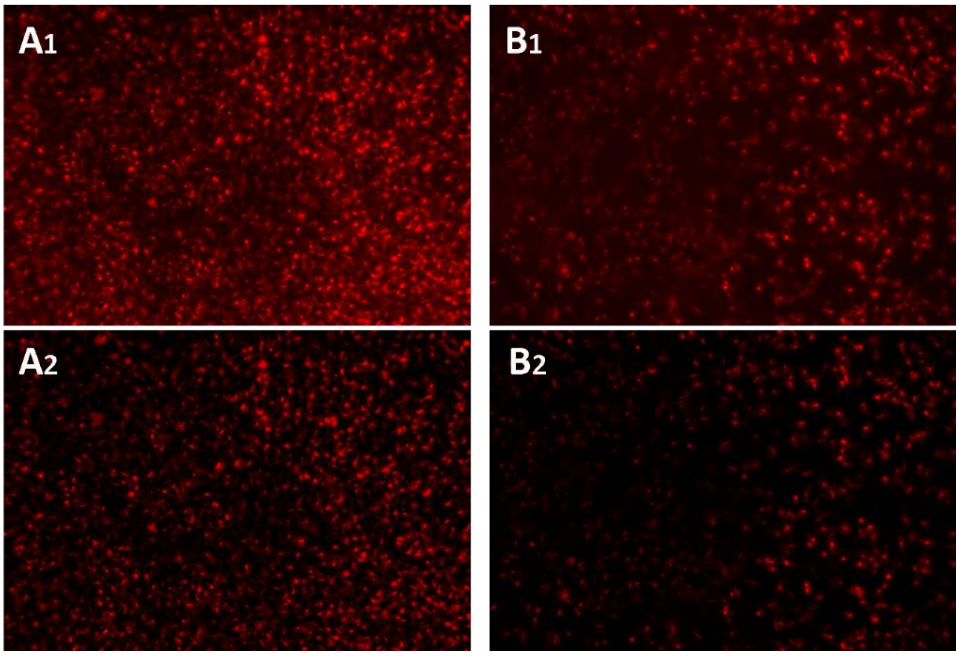

Figure 2.1. The effect of background subtraction. OHSC images before (1) and after (2) background subtraction. A – without tamoxifen and B – treated with tamoxifen.

2. Individual microglia were counted (Fig. 2.2.) using Process>Find Maxima>Set prominence to 30. Prominence was selected to obtain individual selection of microglia cells. Edge maxima were excluded to count only fully visible cells.

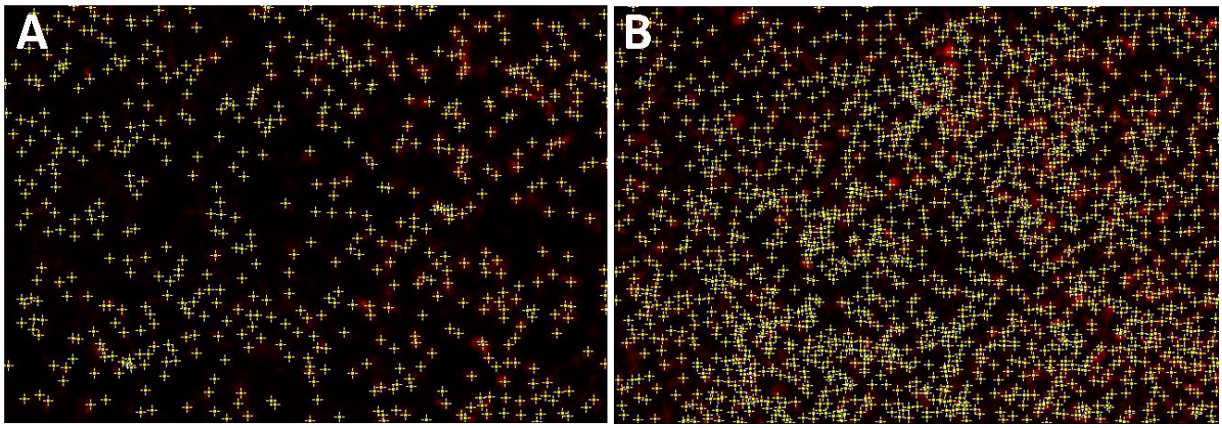

Figure 2.2. Marked individual microglia. A – without tamoxifen. B – treated with tamoxifen.

2.2.6.3. Quantitative analysis of hM4D-mCherry fluorescence

Measurements were performed using the following protocol:

1. To observe weak signal grey values were displayed from 0 to 20 using Brightness and contrast>Set>Min:0, Max:20.
2. To align of major regions of the hippocampus in all the slices (Fig. 2.3.) images were flipped using Image>Transform>Flip Vertically/Horizontally. Next, smaller adjustments were made with Image>Transform>Rotate to achieve optimal alignment.

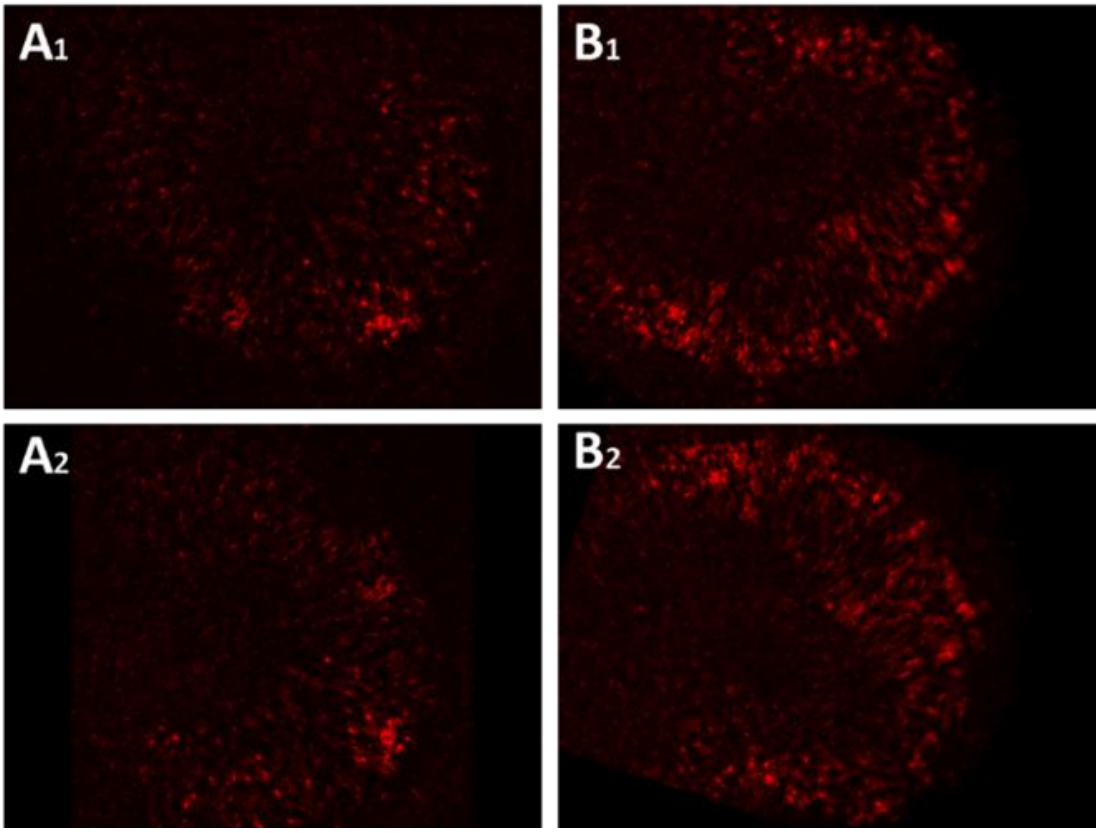

Figure 2.3. OHSC alignment procedure. 1. A and B images before alignment. 2. A and B images after alignment.

3. To measure the exact area ROI was created. The process of creating ROI used in measurements was described in chapter 3.3.2. ROI was applied and aligned to hippocampal regions.
4. ROI was added to the ROI manager using Analyze>Tools>ROI Manager>Add.
5. Entire picture was selected by using Edit>Selection>Select all and added to the ROI manager.
6. In the ROI manager, ROI of interest and the entire picture was selected and XOR function was used to only select the background.
7. Background was removed using Selection>Select None.
8. Threshold was set to 13-255. Threshold was set by Image>Adjust>Threshold.
9. Set required measurements. We used:
    a. Area – to measure area of selection signal in square pixels.
    b. Mean gray value – average signal value in the selection.
    c. Integrated density – the sum of pixel values of the signal in the selection.

Measurements were limited to the threshold.

10. ROI (preparation described in 3.3.2) was added back to the image.
11. Measurements were made using Analyze>Measure.

2.2.6.4. Processing of images acquired with confocal fluorescent microscope

All 3D confocal images were represented as one z plane using Image>Stacks>Z Project>Projection type: Max intensity.

2.2.7. Statistical analysis

All data are shown either as individual samples and mean or as mean ± SD. All points represented individual organotypic slices. Means of variables (area of signal, total signal intensity and mean signal intensity) obtained from analysis of the identical conditions were compared using paired parametric one-tailed t-test analysis. Means of variables obtained from the comparison of different hM4D-mCherry virus loads were compared using unpaired parametric one-tailed t-test analysis. Differences were considered statistically significant when $*p < 0.05$ and very significant when $**p < 0.005$. These tests were performed using GraphPad Prism v6.0. software.

3. RESULTS

In this study we aimed to implement a novel approach to analyze activity-dependent synaptic pruning in developing hippocampus. Synaptic pruning is a complex process mediated by a variety of factors but the most important one is considered to be microglia. Microglia is essential for normal synaptic network maturation and can phagocytose entire dendritic spines (Schafer et al., 2012) or axonal boutons as well as modify synaptic terminals (Weinhard et al., 2018). However, how exactly microglia choose which synapses are going to be modified is still unclear. Emerging research (Ge et al., 2006; Watanabe and Kano, 2011) indicates that neuronal activity might be the driving force behind this process and it works in a competition-driven mechanism. We hypothesized that microglia preferentially select and remove less active synapses reducing the density of axonal boutons and dendritic spines. Therefore, we aimed to develop an experimental approach to evaluate and to modify neuronal activity in developing hippocampus and to define its role in neuron-microglia interaction.

Our experimental workflow was divided into three distinct parts. First, we established organotypic hippocampus slice cultures. Second, we visualized interactions between neurons and microglia. Finally, we optimized the conditions for the expression of designer receptor activated by designer drug that can be used to inhibit neuronal activity and to visualize axonal boutons and dendritic spines and that is delivered by utilizing AAV8/2-CaMKIIα::hM4Di(Gi)-mCherry-WPRE-hgHp(A) DREADD construct (thereafter referred to as AAV-hM4D).

3.1. Establishing experimental setting for the visualization of maturing neurons during the period of synaptic pruning

3.1.1. Establishing organotypic hippocampus slice cultures

Specific and complex environment is required to support neurons and microglia for prolonged period of time. OHSC is a well-known experimental 3D model for functional and morphological analysis of the nervous tissue (Linsley et al., 2019). It is known that OHSC undergo remarkably similar developmental steps in respective time periods compared to those

observed *in vivo* (Muller et al., 1993). Implementing slice cultures is a challenging task and many different protocols exits (Gogolla et al., 2006; Jang et al., 2018; Simoni and Yu, 2006).

We based our protocol on two major research papers (Gogolla et al., 2006; Simoni and Yu, 2006). OHSC was prepared from postnatal day three (P3) mouse pups to ensure that we would be able to track and modify neuron activity during the peak period of synaptic pruning. Main steps of OHSC harvesting were the removal of skin and skull (Fig. 3.1 A,B), transfer of the brain to the dissection medium and cutting off the hemispheres (Fig. 3.1 C), extraction of the hippocampus (Fig. 3.1 D), slicing of the hippocampus to 300 μm slices (Fig. 3.1 E) and placing slices on cell insert membrane (Fig. 3.1 F). Slices were cultured at 35 °C temperature to reduce microglial activation and phagocytic activity (Seo et al., 2012). Healthy slices showed typical hippocampal structure with distinguishable CA and DG regions (Fig. 3.1 F). We observed slices for any signs of degradation or excess activation of microglia indicated by cell infiltration and change in morphology.

Even though we based our protocol on published ones (Gogolla et al., 2006; Simoni and Yu, 2006), we believe we made several improvements. Previous studies have used a "cool-down" period after the dissection to reduce the inflammation and the activation of microglia. On the contrary to the published data, we observed significant reduction of slice viability after any increase in the length of dissection procedure. Furthermore, we believe our protocol has simplified the procedure and put a higher emphasis on speeding up the whole process.

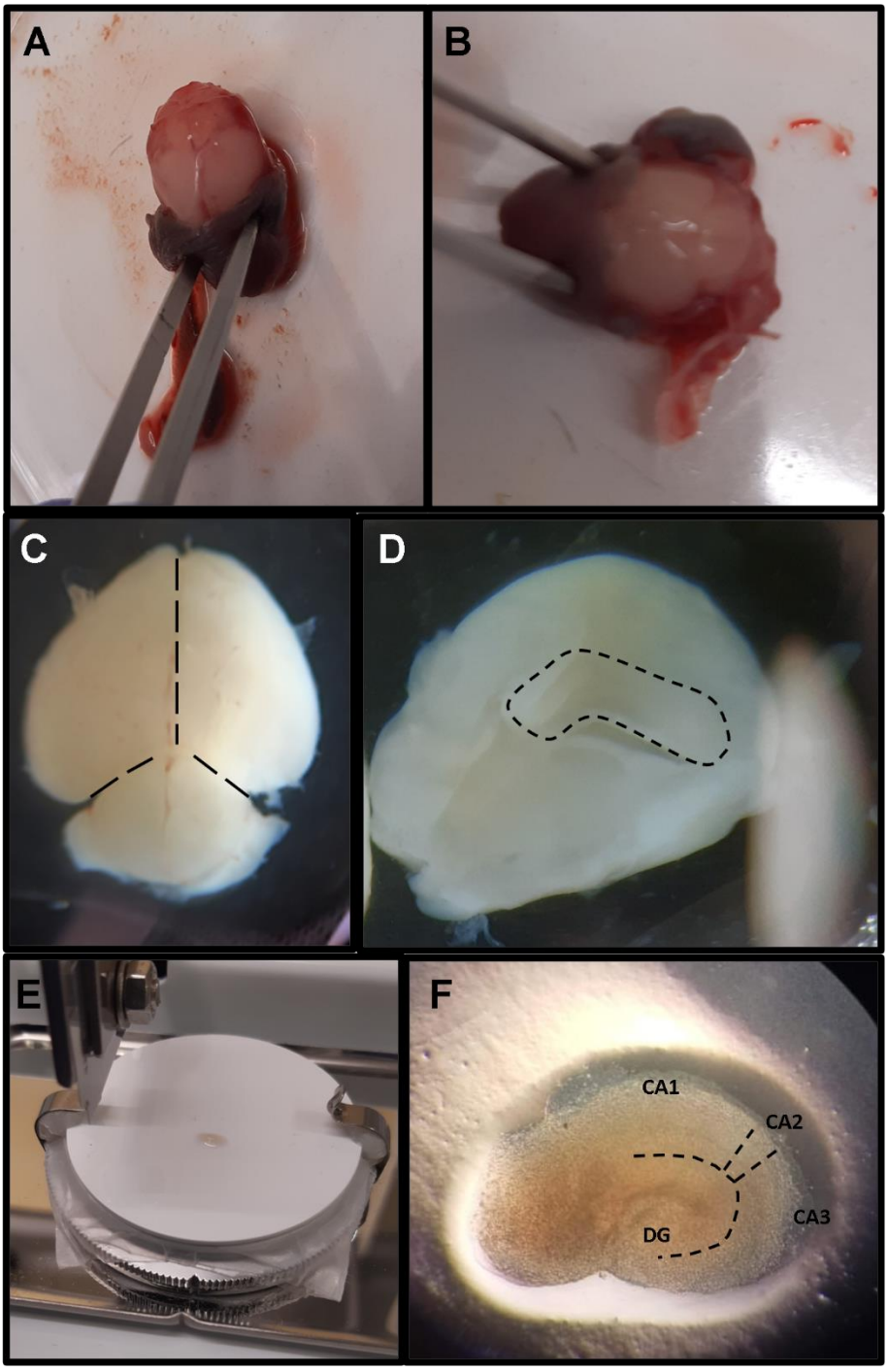

Figure 3.1. Main steps of OHSC preparation: A – Removal of the skin from the skull; B – Removal of cartilage with exposed brain ready for extraction; C – Extracted brain in the dissection medium. Dashed lines shows the relative cut lines for separation of hemispheres, 8× magnification; D – Medial side of cerebral hemisphere with exposed hippocampus marked with dashed lines, 12,5× magnification; E – Hippocampus placed on a tissue chopper ready for slicing; F – OHSC (DIV23) placed on a cell culture insert, magnification 40×. CA – *Cornu Ammonis*, DG – dentate gyrus.

Refined protocol allowed us to harvest organotypic slices and to culture them for extended periods of time (up to DIV23). Cultured slices preserved typical hippocampal slice structure (Fig. 3.1F). Distinguishable regions and normal neuron growth were observed (Fig. 3.2).

3.1.2. Visualization of developing excitatory pyramidal neurons

To visualize excitatory pyramidal neurons *Thy1::EGFP* mice (Feng et al., 2000a) was utilized to prepare OHSC. This mouse line expresses EGFP in sparse populations of excitatory pyramidal neurons of the hippocampus. The expression of fluorescent protein was mediated by modified *Thy1* gene regulatory elements and its expression increases during development (Feng et al., 2000). The density of EGFP-expressing neurons can be reduced by using heterozygous animals (Feng et al., 2000b). EGFP expression allowed us to visualize the maturation of CA1 neurons and their development over time (Fig. 3.2). Even in early days of culturing (DIV4-6, equivalent to P7-P9 *in vivo*) the increase of EGFP-expressing neurons was observed. The trend continued over the next 12 days with a significant increase in both the number and the fluorescence intensity of EGFP-expressing neurons.

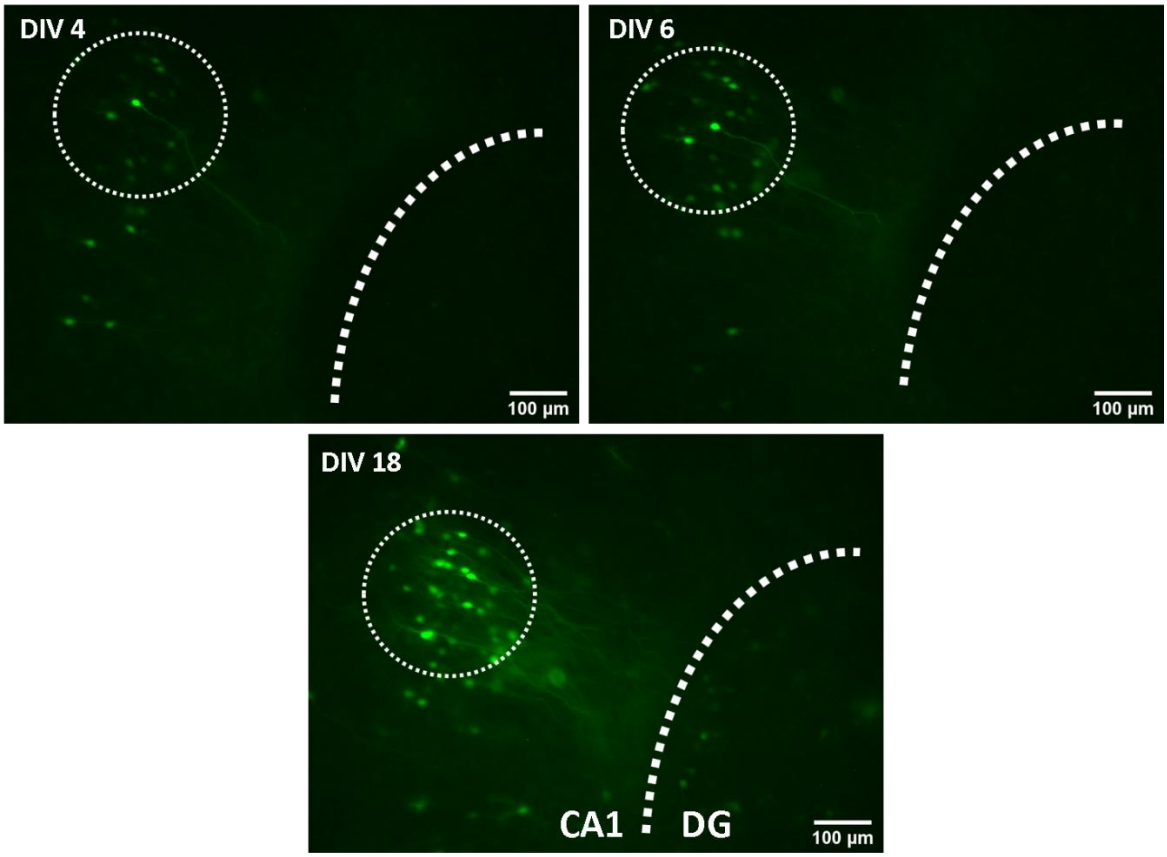

Figure 3.2. Early EGFP expression in CA1 excitatory pyramidal neurons over DIV18. OHSC from *Thy1*::EGFP/+ animal. Circles highlight the area with the significant increase of EGFP-expressing neurons. Wide-field fluorescence imaging.

The number of EGFP-expressing neurons increased considerably (Fig. 3.2). This signifies that cultures remained viable during 18 DIV culturing. Emerging fluorescent neurons may also reflect neurogenesis. Under physiological conditions, there is no neurogenesis in the CA1 region of the hippocampus. However, neurogenesis of the CA1 pyramidal neurons has been previously reported as a result of hypoxia and tissue damage (as in the case of OHSC preparation) (Bendel et al., 2005; Nakatomi et al., 2002). In the future we intend to address this question by performing Ki-67 staining to check for the proliferation of neurons (Weissleder et al., 2016).

After we showed that slices developed and remained viable during early culturing period, subsequently, we analyzed the viability of EGFP-expressing neuron over the period of synaptic pruning. It has been reported that synaptic pruning occurs between P15 (Paolicelli et al. 2011) and P21 (Jawaid et al. 2018) *in vivo* or at DIV16 – DIV19 in OHSC (unpublished data from our group) and is mostly finished by 28 days *in vivo* (Paolicelli et al. 2011). These

findings were supported by Weinhard and colleagues stating that phagocytic activity of microglia peaks at postnatal day 15 and drops by the day 28 of postnatal development (Weinhard et al., 2018). Hence, we cultured OHSC to DIV23 which is equivalent to P26 *in vivo* to include the period of the peak synaptic pruning (Fig. 3.3).

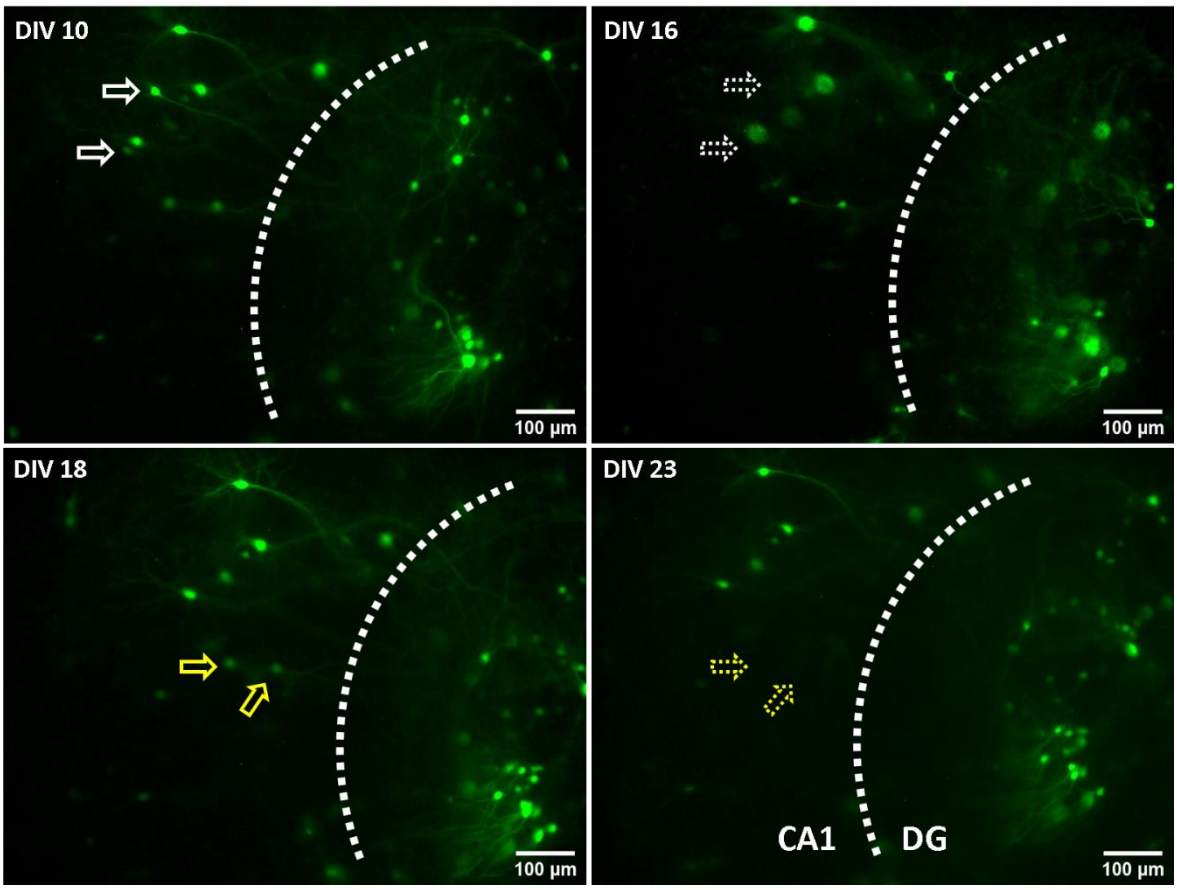

Figure 3.3. Visualization of EGFP-expressing pyramidal neurons in the OHSC throughout the period of synaptic pruning. OHSC was prepared from *Thy1*::EGFP/+ animal. Expression of EGFP is controlled by *Thy1* promoter regulatory units. Solid line arrows mark initially live neurons. Dashed arrows mark the spot where previously live neurons were located. Wide-field fluorescence imaging.

The visualization of neurons was facilitated by *Thy1* promoter regulatory units that provided lifelong expression of EGFP. Majority of neurons maintained their viability throughout the entire experiment (up to DIV23) (Fig. 3.3). However, a small number of neurons could not be visualized during repeated imaging (Fig. 3.3) and thus were presumed to have been lost during culturing. Compared to early culture development, number of EGFP-expressing neuron stayed similar. The distribution of EGFP-expressing neurons was sparse

during the period of intense synaptic pruning. This provided the possibility to track the maturation of the same neurons over time.

Overall, OHSC maintained sufficient neuron viability during the period of synaptic pruning and therefore could be used to investigate neuron-microglia interactions in developing hippocampus.

3.1.3. Visualizing dendritic spines and axonal boutons

Next, we used confocal imaging to acquire high resolution images of OHSC. For confocal imaging *Thy1*::EGFP/+ samples have been fixed and placed on microscope slides. Confocal microscope has produced high resolution images through multiple vertical planes (Fig. 3.4 A, B). Such images allowed us to visualize and evaluate the morphology of axonal boutons and dendritic spines (Fig 3.4 C, D).

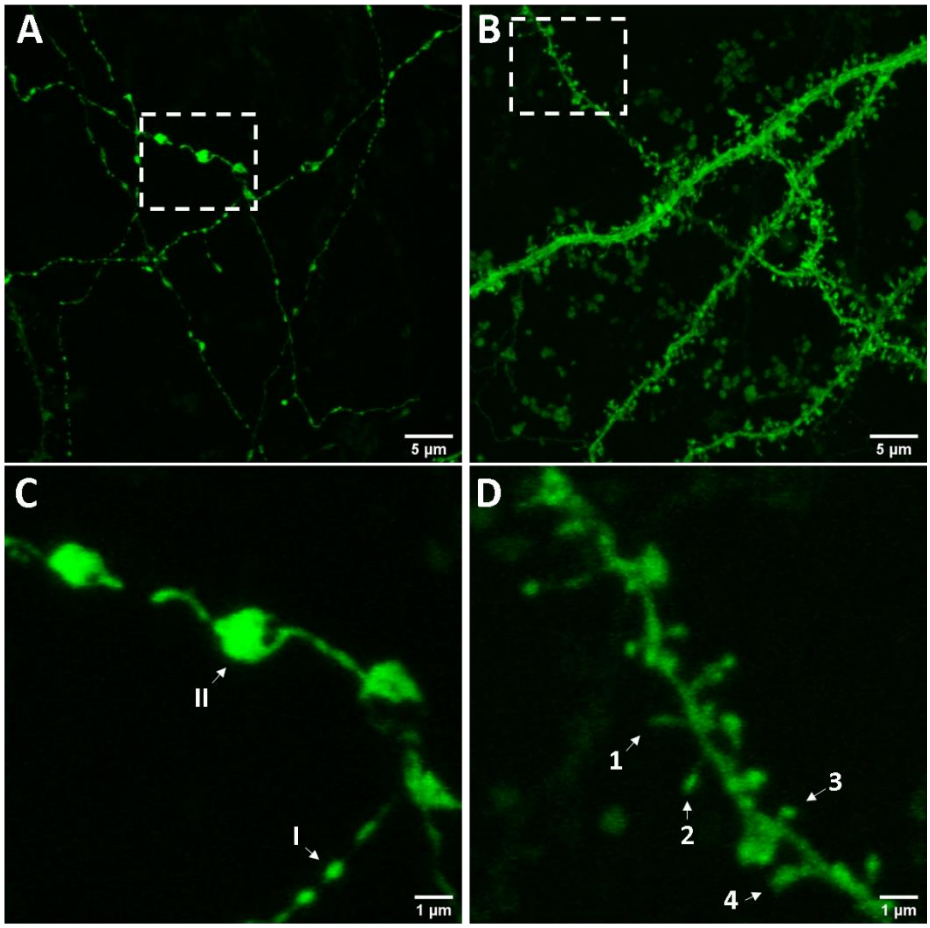

Figure 3.4. Visualization of (A) axonal boutons and (B) dendritic spines at DIV21. C – 4× zoom of axonal bouton demonstrating their state of maturation. I – small bouton. II – large multisynaptic bouton. D – 4× zoom of dendritic spines demonstrating their morphology.1 – dendritic filopodium, 2 – thin spine, 3 – stubby spine, 4 – mushroom-shaped mature spine. OHSC was prepared from *Thy1*::EGFP/+ animal and cultured for DIV21. A – projected from 26 planes. B – projected from 24 planes. Confocal fluorescence imaging.

Axonal boutons (Fig. 3.4 A, C) and dendritic spines (Fig. 3.4 B) with their characteristic variety of shapes were recognized in confocal images. It has been well established that there is a close relationship between axonal bouton and dendritic spine morphology and their function (Heck and Benavides-Piccione, 2015). Hence, we can investigate the function of axonal boutons and dendritic spines by analyzing their morphological characteristics. Acquired images showed small possibly less mature (Murthy et al., 2001) (Fig. 3.4 C, I) and significantly bigger multisynapse boutons (Fig 3.4 C, II) (Zhan et al., 2014). High number of dendritic spines observed in the sample suggested that culturing of the OHSC did not interfere with developmental synapse formation. Dendritic spines were observed in multiple stages of their maturation from synaptic precursors dendritic filopodia

(Fig. 3.4 D, 1) to already mature mushroom-shaped spines (Fig. 3.4 D, 4) (Lai and Ip, 2013). Acquired images were suitable for morphological assessment of synaptic morphology and did not require any signal-enhancing tools.

3.2. Co-visualization of neurons and microglia

Thy1::EGFP, *RC*::LSL-tdTomato, *Cx3cr1*::Cre triple transgenic mouse line was used to establish OHSC, in which both neurons and microglia could be imaged interacting with each other. This provided a unique system to investigate the function of microglia in 3D setting. Visualization of microglia is enabled by a red fluorescent tag tdTomato. The expression of tdTomato is initally blocked by a stop codon surrounded by loxP sequences (Luche et al., 2007). Induction of the tdTomato expression in microglia is regulated by an estrogen receptor modulator tamoxifen (Andersson et al., 2010). Fluorescence is activated only when the active form of tamoxifen, 4-hydroxytamoxifen, activates estrogen receptor (fused with Cre recombinase) and Cre is translocated into the nucleus . In the nucleus Cre removes the stop codon and enables tdTomato expression (Zhong et al., 2015). However, the inhibition of this expression is only partial and the system is considered to be “leaky” (Zhao et al., 2019).

In our study, tamoxifen was added at DIV0 and OHSC were cultured for further 18 days. We compared the density of microglia in organotypic slices with and without tamoxifen treatment (Fig. 3.5). Microglia density of tamofixen-treated OHSC was 18 cells/100 μm^2. In contrast, in slices without tamoxifen density of microglia was 6.4 cells/100 μm^2. Overall, the application of tamoxifen increased the number of visible microglia by 2.8 times in DIV18 samples.

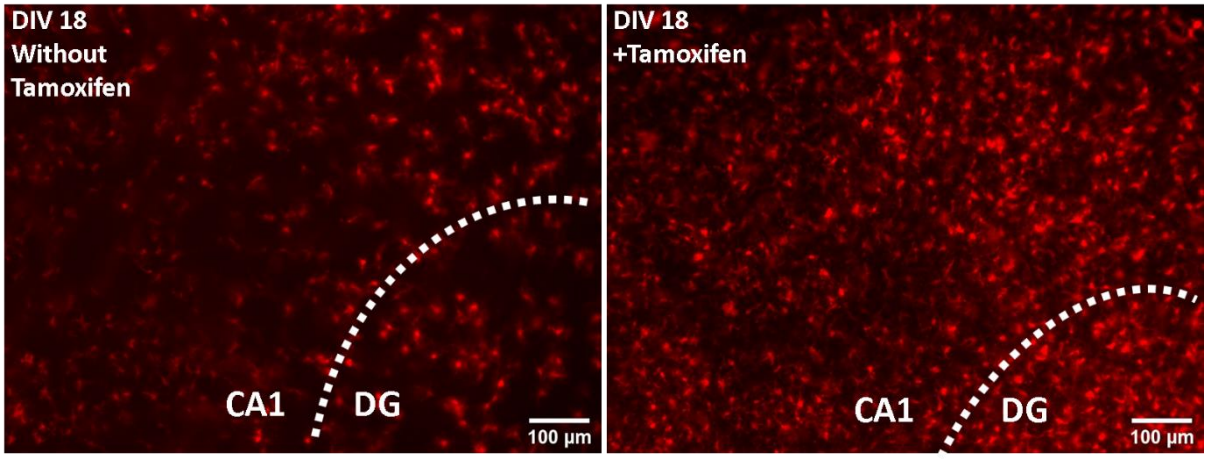

Figure 3.5. OHSC from *Thy1::EGFP, RC::LSL-tdTomato, Cx3cr1::Cre* with and without tamoxifen treatment at DIV18. tdTomato-expressing microglia in CA1 and DG regions of the hippocampus. CA – *cornu Ammonis*, DG – dentate gyrus. Wide-field fluorescence imaging.

Due to a "leaky" promoter we had different microglia densities with and without tamoxifen treatment. Therefore we could investigate microglia in two different ways. First, without tamoxifen, the density of microglia remained relatively low and we could investigate the morphology of individual microglia, which is closely related to their function (Fernández-Arjona et al., 2017). Second, the addition of tamoxifen increases the number of visible microglia to almost 90% (Álvarez-Aznar et al., 2020) and is better suited to analyze direct contacts between neurons and microglia due to increased density of such contacts. To confirm the published data of tamoxifen efficiency we are planning to perform microglia-specific Iba1 co-staining to quantify tdTomato-positive microglia (Fernández-Arjona et al., 2017).

Confocal imaging of slices without tamoxifen was performed to acquire high-detail image of microglia (Fig. 3.6). EGFP signal showed healthy maturing synaptic network (Fig. 3.6 A). Imaging of tdTomato signal allowed for better inspection of complex morphology of microglial protrusions (Fig. 3.6 B). The overlay of EGFP and tdTomato allowed us to inspect direct points of neuron-microglia interaction (Fig. 3.6 C, D).

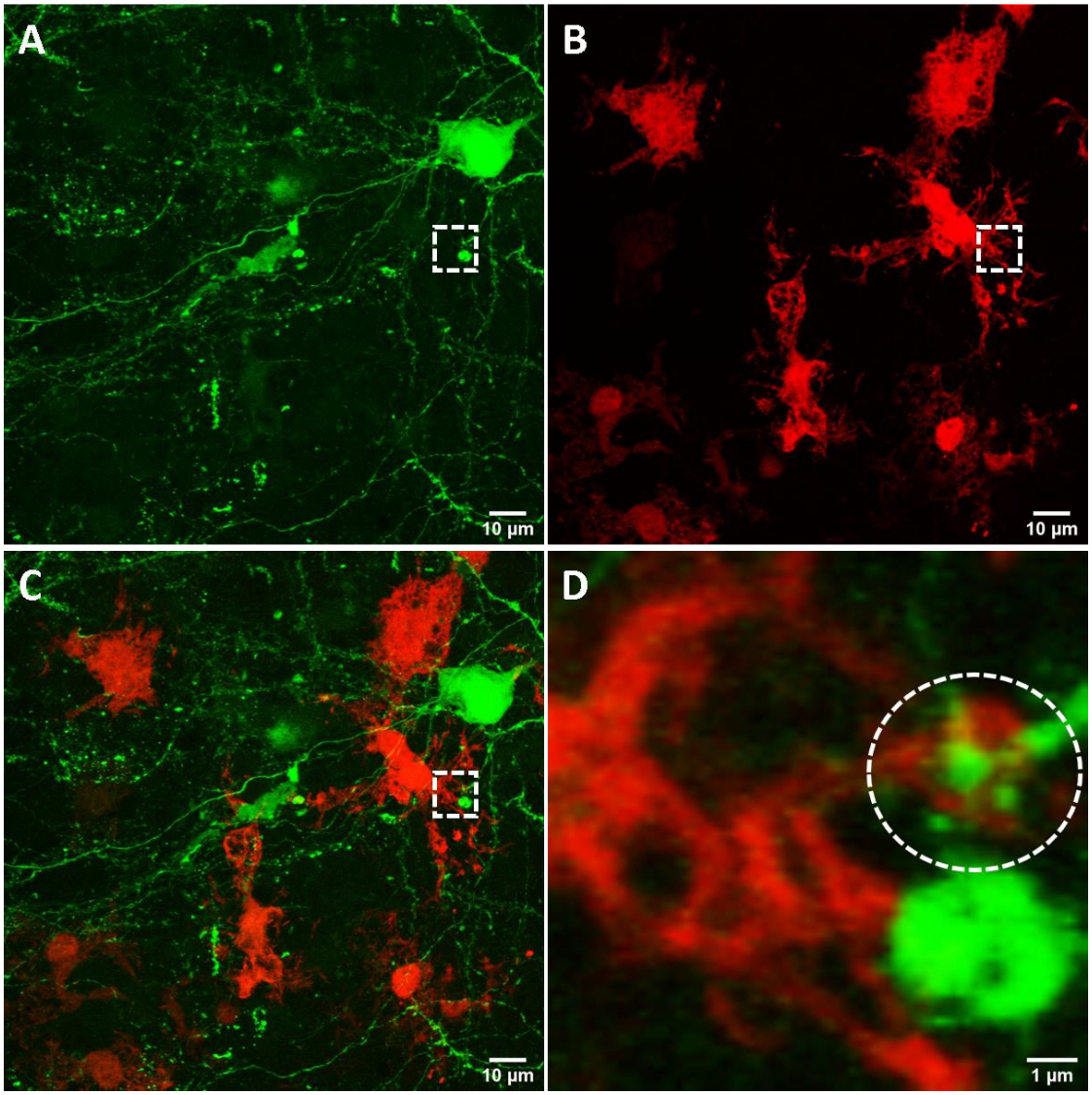

Figure 3.6. Neurons and microglia maintain close connections in OHSC. A – EGFP-expressing pyramidal excitatory neurons. B – tdTomato labels intricate structure of microglia. C – the overlay of EGFP and tdTomato signals shows overall distribution of microglia and neurons. D – 16× zoomed protrusion of microglia co-localized with a dendrite. Dashed square shows magnified area in D. Dashed oval highlights the co-localization of microglia and neuron. CA1 region in the hippocampus. Images projected from 28 planes. Confocal fluorescence imaging.

Furthermore, OHSC with labeled microglia and neurons can be combined with a variety of different molecular tools desgined to modify or visualize the activity of neurons. It provides unique opportunity to observe active role of microglia in the remodelling of synaptic networks.

3.3. Setting up DREADD-mediated inhibition of neural activity

After we have established a method for long term culturing and visualization of neurons and microglia, we used inhibitory DREADD (hM4D) to examine the effect of reduced neuronal activity for developmental remodeling of the circuitry. We chose AAV8/2-CaMKIIα::Hm4Di(Gi)-mCherry-WPRE-hgHp(A) DREADD construct. Adeno associated virus serotype 8 was used to ensure high level of infection in neurons (Hammond et al., 2017). Our AAV-hM4D construct had calmodulin kinase II α promoter, which is expressed in excitatory pyramidal hippocampal neurons. Our AAV-hM4D construct had fluorescent protein mCherry which is fused with DREADD to track its localization and the level of expression. Woodchuck hepatitis virus posttranscriptional regulatory element (WPRE) increases the expression of the whole construct (Zufferey et al., 1999). Human growth hormone polyadenylation signal (hgHp(A)) enhanced polyadenylation and termination of construct sequence (Gubler et al., 1983). Activation of our AAV-hM4D construct was mediated by a synthetic ligand CNO (Zhu and Roth, 2014).

Our DREADD allowed us to specifically analyze pyramidal neuron circuitry preserved in the organotypic slices. Specifically, we investigated the synapses between the pyramidal neurons from CA3 region, which project axons, called Shaffer collaterals, and pyramidal neurons of CA1 region. Since, both CA1 and CA3 neurons can potentially be inhibited by the DREADD, it provides a suitable research setting to analyze both presynaptic (axonal boutons) and postsynaptic (dendritic spines) compartments. All following experiments were performed using OHSC harvested from *Thy1::EGFP* mouse line in which EGFP worked as an internal control to establish the morphology of axonal boutons and dendritic spines with unaffected synaptic activity.

Optimized conditions for AAV-hM4D infection of OHSC were vital for the best possible artificial receptor expression. Expression of hM4D-mCherry was tracked using fluorescent protein mCherry which has a physical link with the artificial receptor. Expression of hM4D-mCherry has been paramount for successful inhibition of neuronal activity. Also, we expected that reliable expression of hM4D- would allow us to visualize dendritic spines and axonal boutons and to enable their morphological evaluation after the alteration of neuronal activity. To achieve this goal many practical and physiological considerations have been addressed. First, inhibition of neuronal activity by the activation of hM4D should correspond to the peak of synaptic pruning which is known to occur between P15 (Paolicelli et al., 2011) and P21 (Jawaid et al., 2018) *in vivo* or at DIV16 – DIV19 in OHSC

(unpublished data from our group). Second, experimental timeline has to end before DIV25 (which corresponds to P28 for live animals) which marks the end of significant synaptic remodeling in the hippocampus (Paolicelli et al., 2011). Third, the integration, synthesis and transportation of the hM4D-mCherry into the distal parts of the neuron could take up to 7 – 14 days (Călin et al., 2018; Lu et al., 2011). Also, in published studies inhibition of neural activity by CNO has been usually maintained for 24 h (López et al., 2016a) and then samples had to be cultured for 3 more days to achieve observable morphological changes (Koyama et al., 2017). According to these criteria primary experimental scheme was constructed (Fig. 3.7).

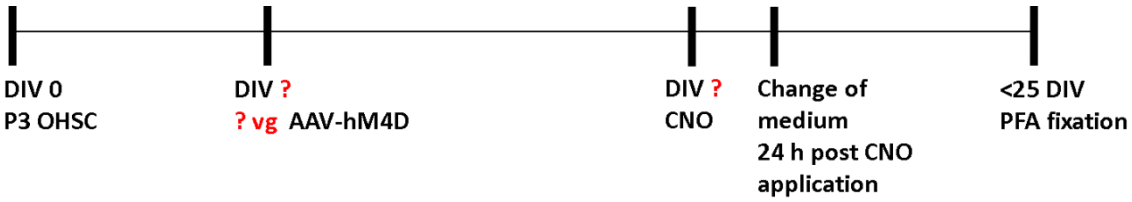

Figure 3.7. Experimental timeline for hM4D-mCherry expression in OHSC.

First, we decided to gather OHSC from 3 day old mice. Second, we had to decide on the day of infection and the amount of AAV-hM4D construct that would yield optimal expression of hM4D-mCherry. Third, we had to determine time required for sufficient hM4D-mCherry expression to inhibit neuronal activity using CNO. OHSC had to be cultured with CNO for 24 h and further 3 days of culturing were required for morphological changes in axonal boutons and dendritic spines. Finally, the experiment must be finished before DIV25.

3.3.1. Selecting the day for AAV-DREADD infection

To optimize the timeline of AAV-DREADD experiment, first we had to decide on which day after slice preparation the virus should be added to OHSC. On one hand, the earliest possible infection day provides us with the longest period of DREADD expression. Therefore, it ensures that DREADD is efficiently transported into distal parts of dendrites and axons. Furthermore, it provides artificial receptors with enough time to be integrated into the membrane, which is required to exert their inhibition of neural activity. Finally, viral particles penetrate organotypic slices easier on earlier days of infection due to the fact glial scar

continues to form until DIV5 (Gerlach et al., 2016). However, early day of infection might impede efficient expression of hM4D-mCherry. First, harvesting of OHSC produces significant amount of cell debris on top of the slice. These remains of neurons get infected by AAV-hM4D and reduce virus load on the healthy neurons located deeper in the slice. Later during culturing, this debris gets removed. Second, dissection damages the tissue, stimulating inflammatory microglial activation, increasing phagocytic activity and thus hindering effective AAV infection. Later day of infection reduces the time allowed for DREADD expression but mostly bypasses the infection of debris and initial microglia activation problems.

First, early date of infection (DIV1) (Avaliani et al., 2016; Weinhard et al., 2018) and 9 x 10^8 vg virus load were selected based on research made using similar AAV-DREADD constructs (Boehringer et al., 2017) (Fig. 3.8).

Figure 3.8. Timeline of DREADD experiment with DIV1 AAV-hM4D treatment date, 9 x 10^8 vg virus load and confocal fluorescence imaging at DIV12.

Selected virus load (9 x 10^8 vg) was higher compared to that used by other researchers (Alberto J López with collegues used 2.3 x 10^8 vg) in experiments utilizing similar DREADD constructs (López et al., 2016a) . This ensured more than sufficient amount of viral particles for every slice. However, 11 days after infection (DIV12) there was no mCherry expression as evaluated by confocal microscopy, even though the slices maintained normal viability and morphology of *Thy1*::EGFP neurons (Fig. 3.9). This lack of hM4D-mCherry fluorescence was likely caused by the majority of viral particles infecting cellular debris.

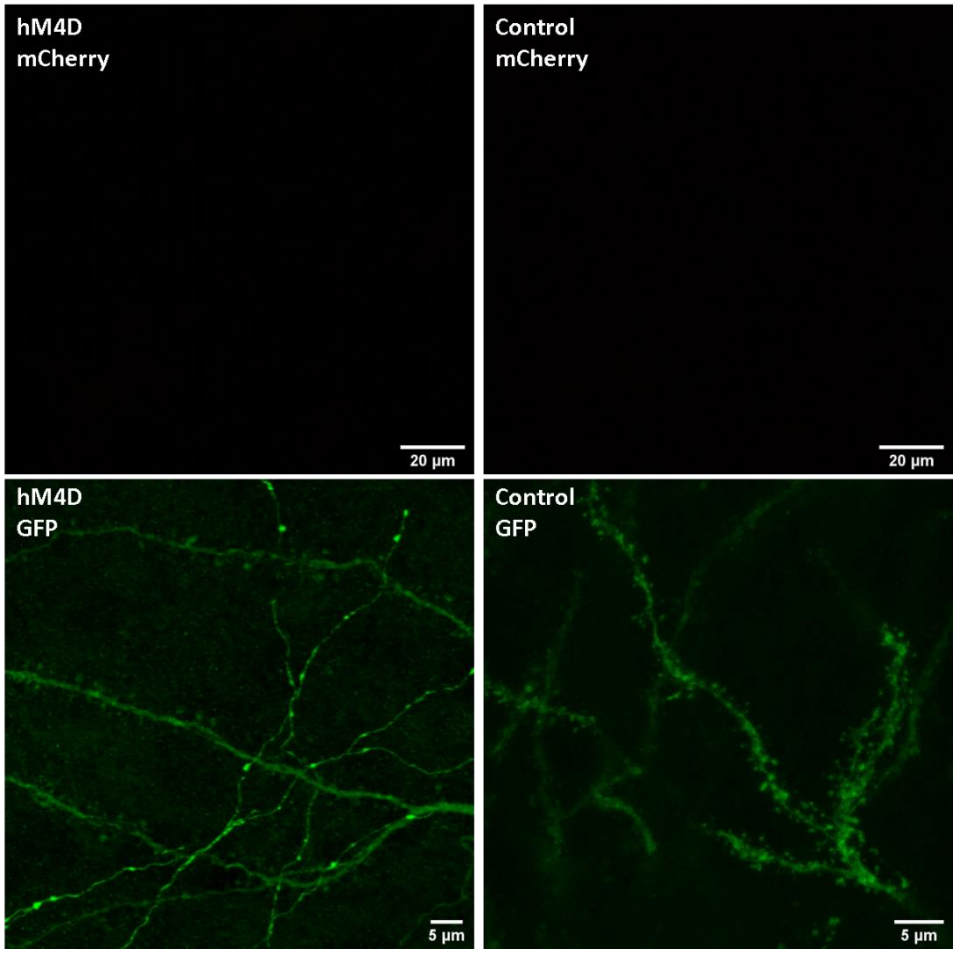

Figure 3.9. No mCherry expression was observed after 11 days of DIV1 AAV-hM4D infection. Control sample was cultured without any treatment. EGFP images projected from 33 planes. mCherry images projected from 24 planes. Confocal fluorescence imaging.

Next, we decided to delay the infection to DIV5 using the same AAV-hM4D virus load (9 x 10^8 vg) and evaluated the slices on DIV12 using wide-field microscopy (Fig. 3.10).

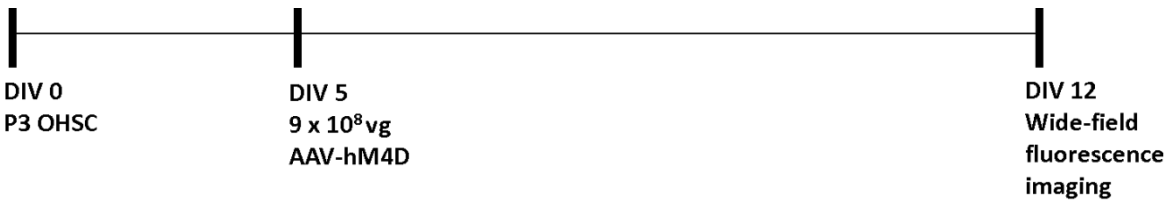

Figure 3.10. Timeline of DREADD experiment with AAV-hM4D infection at DIV5 and wide-field fluorescence imaging at DIV12.

DIV5 for AAV-hM4D infection was chosen due to several reasons. First, cellular debris and dead cells are removed during the first week *in vitro* (Simoni and Yu, 2006). Second, the expression of CamKIIα which was employed as a promoter to regulate expression of our AVV-hM4D construct is low at P4 (DIV1) (Kelly and Vernon, 1985). CamKIIα expression in excitatory pyramidal neurons of hippocampus is minimal in the first postnatal days and starts to increase by fifth postnatal day (Kelly and Vernon, 1985). Seven days after infection (at DIV12) weak but observable mCherry fluorescent signal was seen in infected slices (Fig. 3.11).

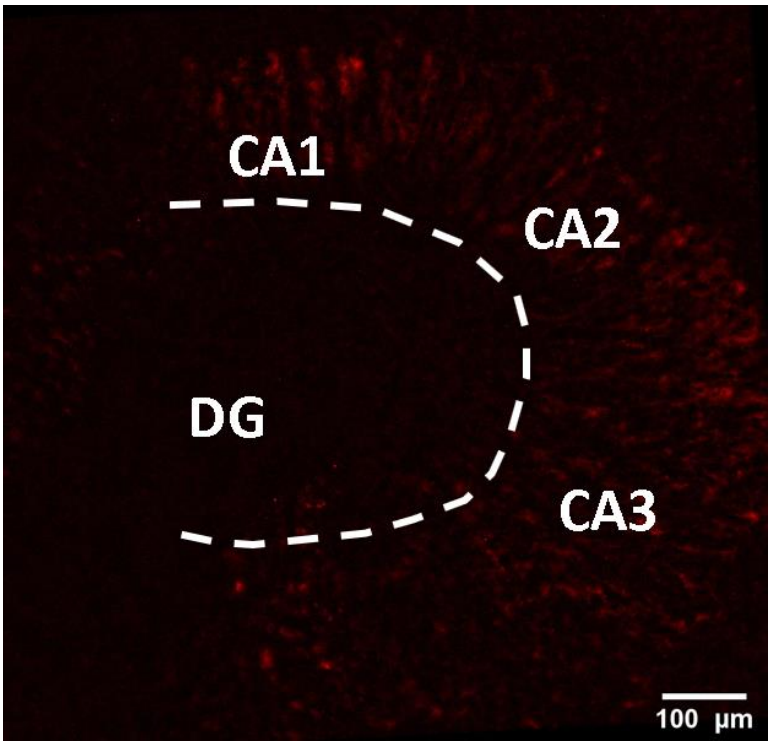

Figure 3.11. mCherry expression after 7 days of DIV5, 9 x 10^8 vg virus load infection of AAV-hM4D. Wide-field fluorescence imaging.

hM4D-mCherry was distributed throughout the entire *cornu Ammonis* and dentate gyrus. Overall, primary data showed that detectable hM4D-mCherry expression could be seen after 7 days of expression when OHSC treatment was performed at DIV5. These results strongly suggested that infection of slices should be performed no earlier than DIV5.

3.3.2. Time profile of hM4D-mCherry expression

Next, we evaluated the expression profile of hM4D-mCherry. Since our construct has a physical link between fluorescent tag mCherry and the artificial receptor we expected that better neuronal inhibition could be achieved when higher mCherry fluorescence was observed. DREADD expression is regulated by CamKIIα promoter which activity is known to increase 10-fold from P5 to P25 (Kelly and Vernon, 1985), therefore AAV-hM4D expression should also significantly increase during the same period. We showed observable mCherry signal 7 days (DIV12) after infection (Fig 3.11). To define whether expression continues to grow till the start of peak synaptic pruning (DIV16) (unpublished data from our group), three time points were chosen: 8, 10, 11 days after infection (DIV13, DIV15, DIV16) to follow the expression of AAV-hM4D over time and to select the time for hM4D activation (Fig 3.12).

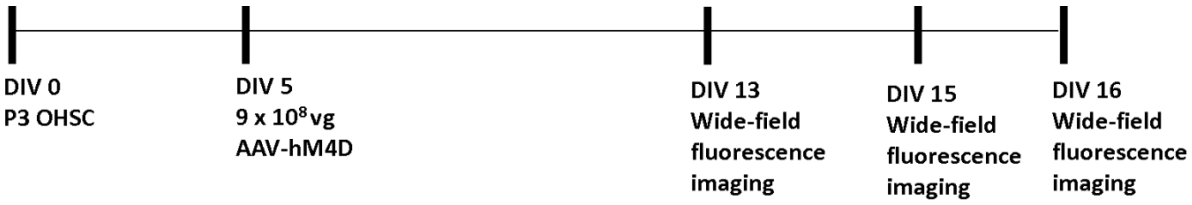

Figure 3.12. Timeline to establish time profile of AAV-hM4D expression using DIV5 treatment of AAV-hM4D and 9 x 10^8 vg virus load.

The expression of AAV-hM4D was analyzed in three slices (S1, S2, S3) (Fig. 3.13). The fluorescence of mCherry was observed in the CA1, CA2, CA3 and DG regions of the hippocampus and a consistent growth of signal was detected from day 8 to day 11 after infection with 9 x 10^8 vg virus load AAV-hM4D at DIV5.

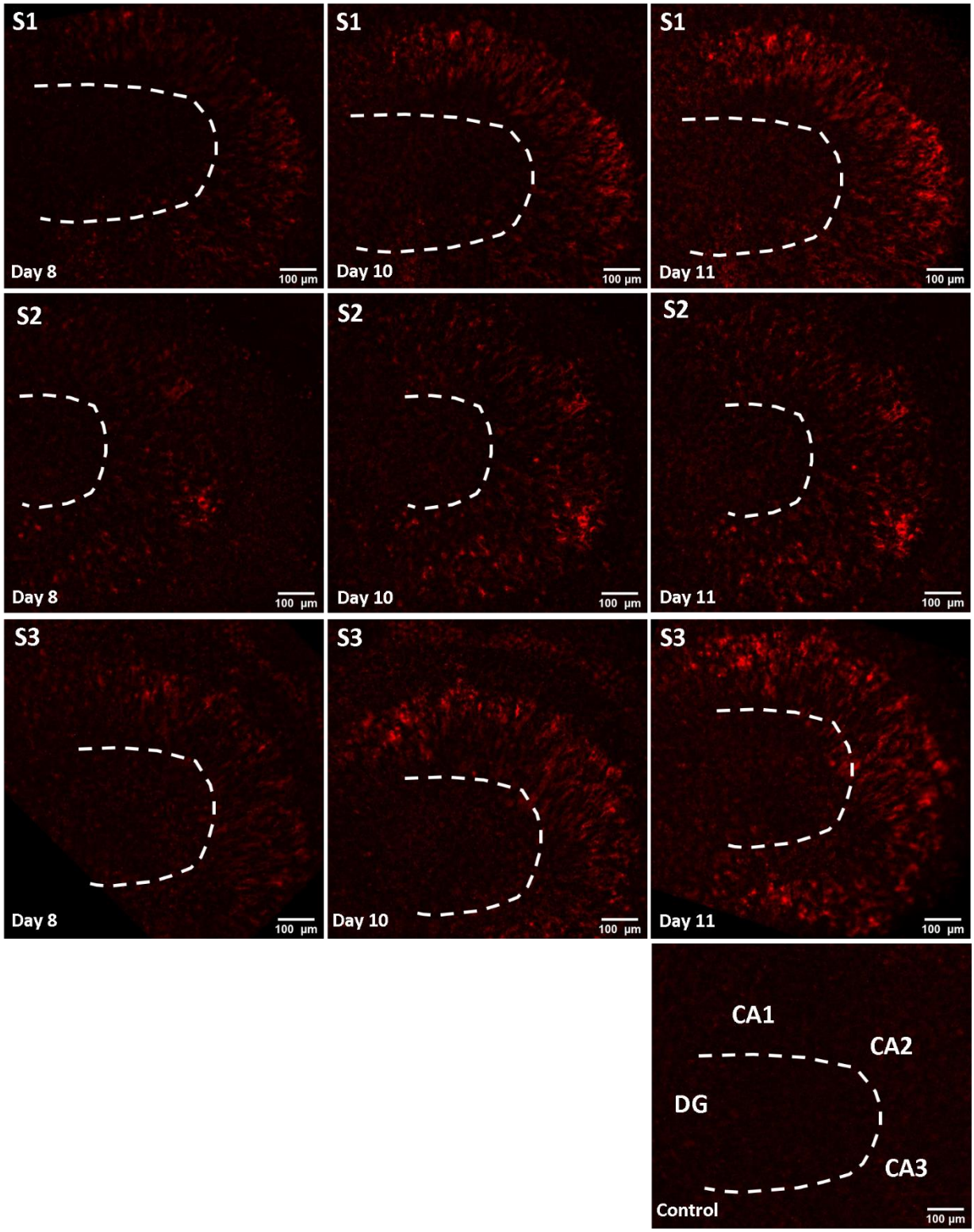

Figure 3.13. mCherry expression over time. Three slices (S1, S2, S3) were imaged 8, 10, 11 days (DIV13,15,16) after 9 x 10^8 vg load of AAV-hM4D infection at DIV5. DG – dentate gyrus, CA – *cornu Ammonis*. Wide-field fluorescence imaging.

The fluorescence of hM4D-mCherry over time was then measured to obtain quantitative data. We were not able to segment individual cells expressing mCherry fluorescent protein, in wide-field EVOS microscope images; therefore, we evaluated total fluorescence in CA1 – CA3 region of hippocampus. The ROI was designed based on hippocampal circuitry data (Fig. 3.14 A, B), individual shape of the slices (Fig. 3.14 C) and the rotation of slices (Fig. 3.14 D). ROI was selected to include CA1b-CA3b (Fig. 3.14 A) *str. pyramidale, str. radiatum, str. lacunosum-moleculare* molecular layers of the hippocampus (Fig. 3.14 B). *Str. pyramidale* contains cell bodies of the excitatory pyramidal neurons, *str. radiatum* and *str. lacunosum-moleculare* holds the entire dendritic tree of the same neurons which form synapses with Schaffer collaterals that are forward projections of CA3 pyramidal neurons. Selected ROI was customized to all slices analyzed in our experiments (6 slices) over time (Supp. Fig. 1).

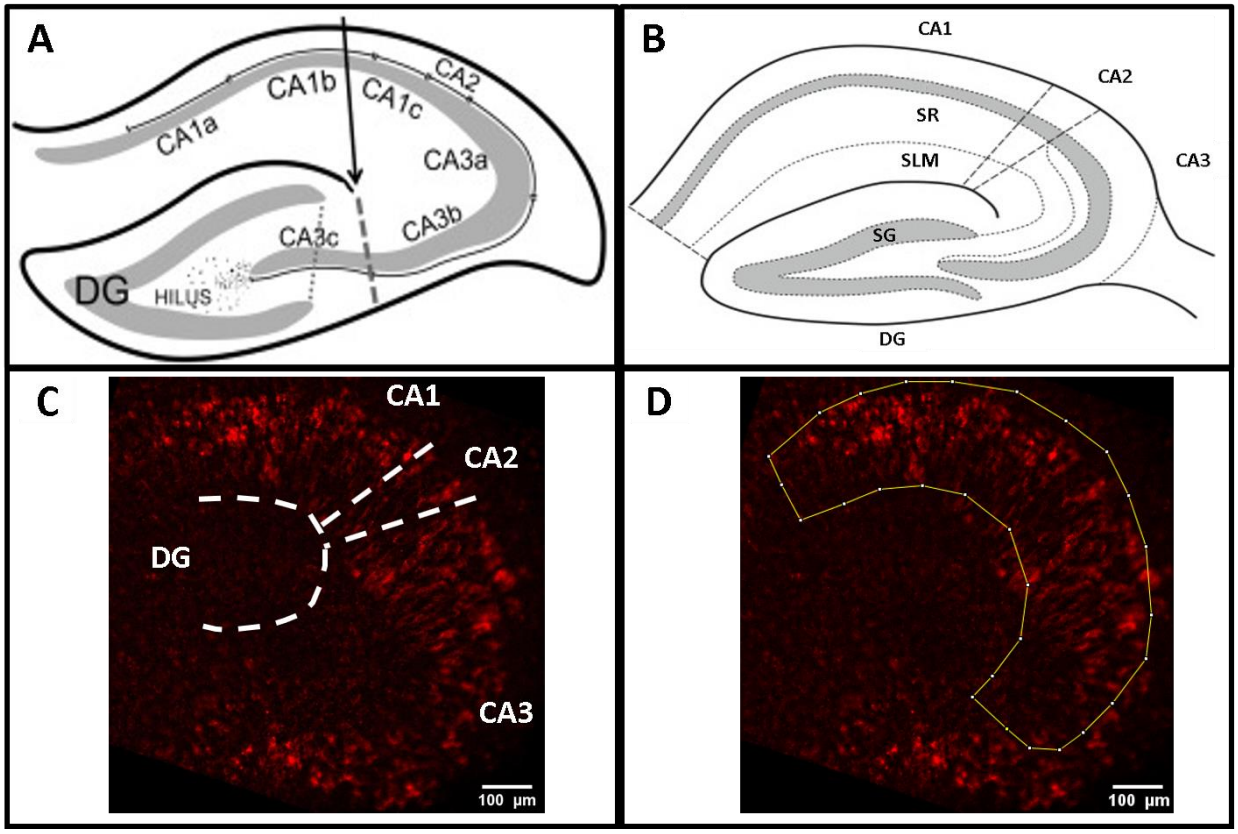

Figure 3.14. Defining ROI for OHSC image analysis. CA – *cornu ammonis*, DG – dentate gyrus, SP – *stratum pyramidale*; SR – *stratum radiatum*, SLM – *stratum lacunosum-moleculare*, SL – *stratum lucidum*, SG – *stratum granulosum*. A – distribution of CA regions throughout hippocampus (Conrad, Ortiz, & Judd, 2017). B – molecular layers of the hippocampus, adapted from Li and Pleasure, 2013 (Li and Pleasure, 2013). C – establishing hippocampal regions in OHSC. D – adjusting ROI to individual images. Wide-field fluorescence imaging.

Subsequently, ROI was applied to OHSC of 9 x 10^8 vg virus load group (three slices 8, 10, 11 days after AAV-hM4D infection at DIV5) (Fig. 3.15). Fluorescent area, normalized fluorescence intensity and mean fluorescence intensity were measured in this ROI.

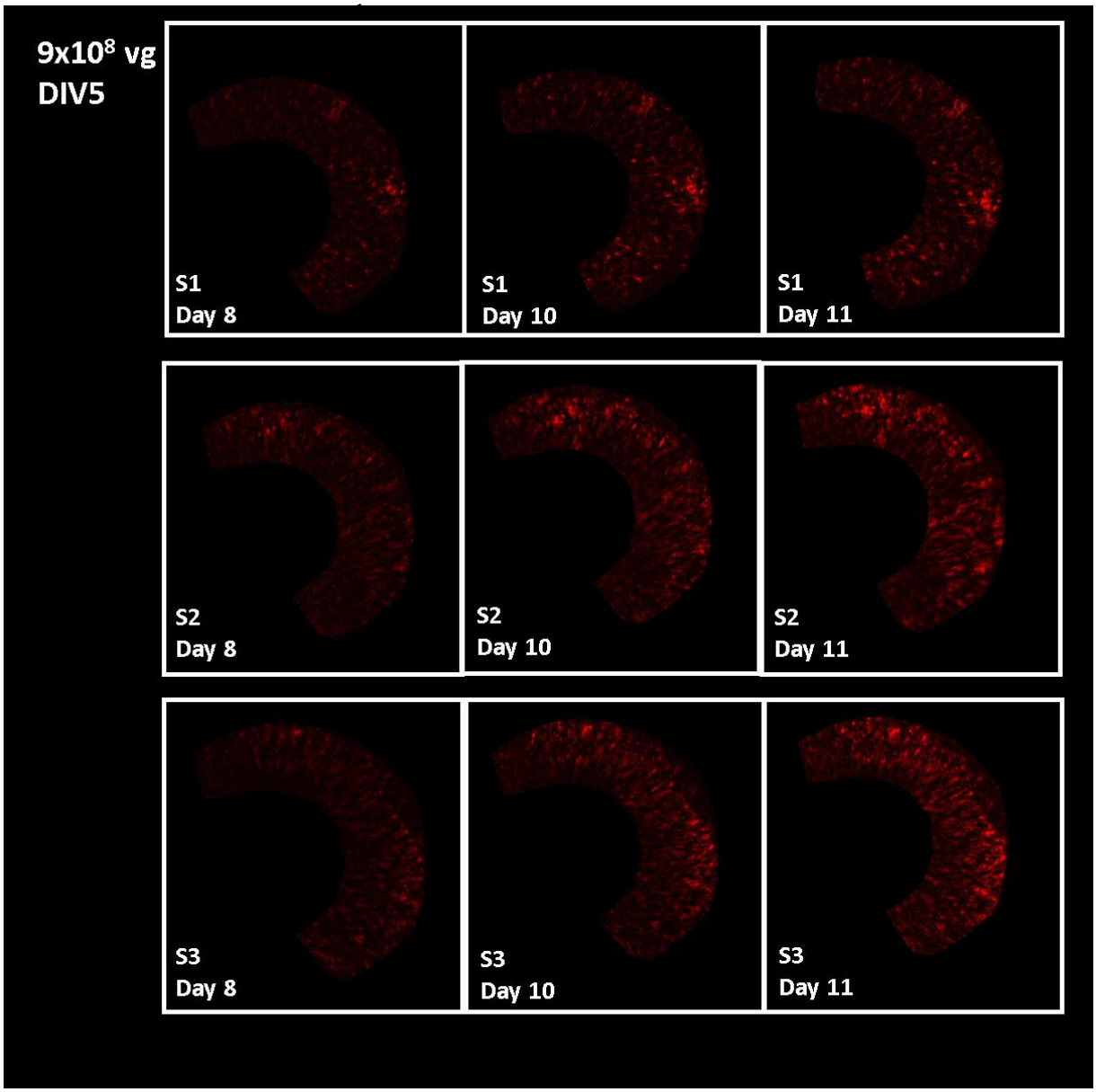

Figure 3.15. ROIs (corresponding to CA1b-CA3b regions) from slices treated with of 9 x 10^8 vg virus load of AAV-hM4D at DIV5 for quantification of mCherry fluorescence over time. Wide-field fluorescence imaging.

First, the total area of fluorescence was measured of three OHSC to evaluate the evolution of mCherry signal over time (Fig. 3.16). In general, steady increase of total area was noticed over three time points in all three samples. Samples showed relatively similar mCherry signal area at 8 days after infection (DIV13) but displayed vastly different signal area by 11 days after infection (DIV16). On average, total area increased by 5.9 times (p = 0.045) from DIV13 to DIV16. Also, the increase in fluorescent area was greater between period of 10 – 11 days (DIV15 – DIV16) compared to 8 – 10 days (DIV13 – DIV15) after infection. Increase in fluorescent area could signify more cells expressing hM4D-mCherry

over time. Also, it could correspond with hM4D-mCherry transportation into distal parts of the cell (axon and dendrites).

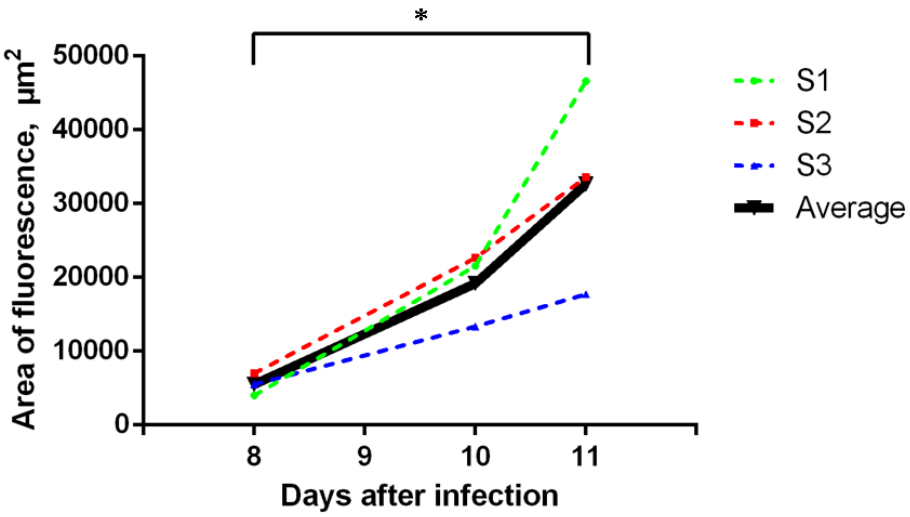

Figure 3.16. Total area of mCherry fluorescence signal in CA1b-CA3b regions 8-11 days after AAV-hM4D infection. N = 3, * $p < 0.05$.

Then, total fluorescence intensity was evaluated over time (Fig. 3.17). We observed similar trend compared to the total fluorescent area with higher increase of intensity during the period of 10 – 11 days (DIV15 – DIV16) compared to 8 – 10 days (DIV13 – DIV15). Average intensity increased by 6.7 times ($p = 0.040$) from 8 to 11 days (DIV13 – DIV16) after the infection. Overall, data indicated significant increase in the amount of fluorescent protein mCherry. This might be due to the increasing activity of CamKIIα promoter during the same period of hippocampal development (Kelly and Vernon, 1985).

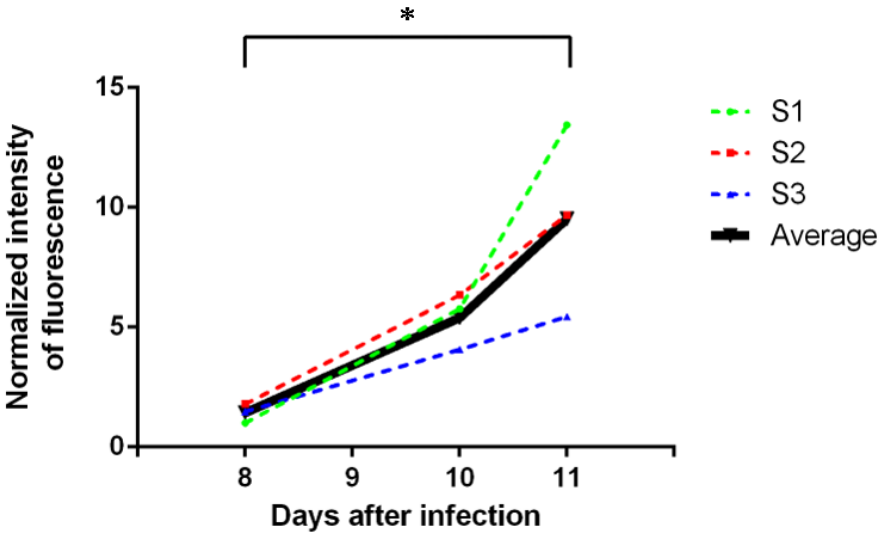

Figure 3.17. Total fluorescence intensity in CA1b-CA3b regions 8-11 days after AAV-hM4D infection. N = 3, *$p < 0.05$. Normalization was done by dividing the total fluorescence intensity of all points by the value of lowest total intensity.

Finally, to evaluate whether fluorescence intensity in a single neuron is increasing over time, we evaluated average fluorescence intensity per pixel of the mCherry signal area (Fig. 3.18). Mean intensity value significantly increased by 1.15 times ($p = 0.002$) from 8 to 11 days after infection. Even though, this change is minute, it signifies that increase of average intensity is greater than the increase of average area. Furthermore, this clarifies that the synthesis of new fused hM4D-mCherry proteins takes place in neurons over time.

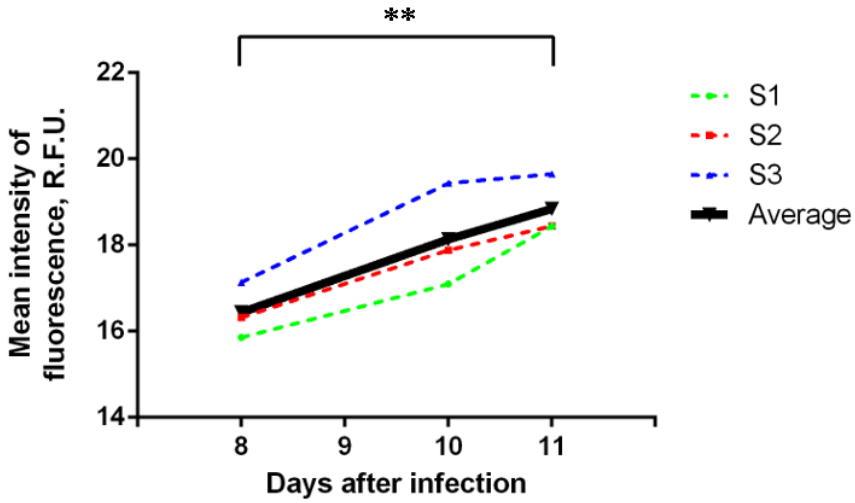

Figure 3.18. Mean fluorescence intensity in CA1b-CA3b regions 8-11 days after AAV-hM4D infection. R.F.U. – relative fluorescence units. N = 3, **$p < 0.005$.

Overall, our data demonstrated that mCherry fluorescence (and presumably the number of artificial receptors capable of inhibiting neural activity) increased in neurons from 8 to 11 days after DIV5 infection of 9 x 10^8 vg virus load AAV-hM4D. Since day 11 after infection showed the highest mCherry signal, we decided that DIV16 is sufficient to perform activation of DREADD by CNO.

3.3.3. Defining AAV-hM4D virus load for optimal hM4D-mCherry expression

For our initial experiments we chose high (9 x 10^8 vg) AAV-hM4D virus load to ensure high chance of infection. Next, we compared 9 x 10^8 vg virus load with to 3,6 x 10^8 vg virus load to reduce hM4D-mCherry expressing neuron density and to enable visual isolation of individual hM4D-mCherry-expressing neurons. To assess morphological characteristics of dendritic spines and axonal boutons, individual neurons with minimally overlapping processes and high fluorescent signal intensity are required. Using 9 x 10^8 vg virus load (Fig.3.13) we observed overlapping neurons with no clear definition. Therefore, we compared mCherry fluorescence 11 days after (DIV16) AAV-hM4D application of different (9 x 10^8 vg and 3,6 x 10^8) virus loads (Fig. 3.19).

Figure 3.19. Timeline to define AAV-hM4D virus load for optimal density of hM4D-Cherry-expressing neurons after DIV5 treatment.

Three slices of 9 x 10^8 vg virus load and two of 3.6 x 10^8 vg were analyzed. The density of neurons expressing hM4D-mCherry was lower when slices were infected with 3.6 x 10^8 vg virus load (Fig. 3.20).

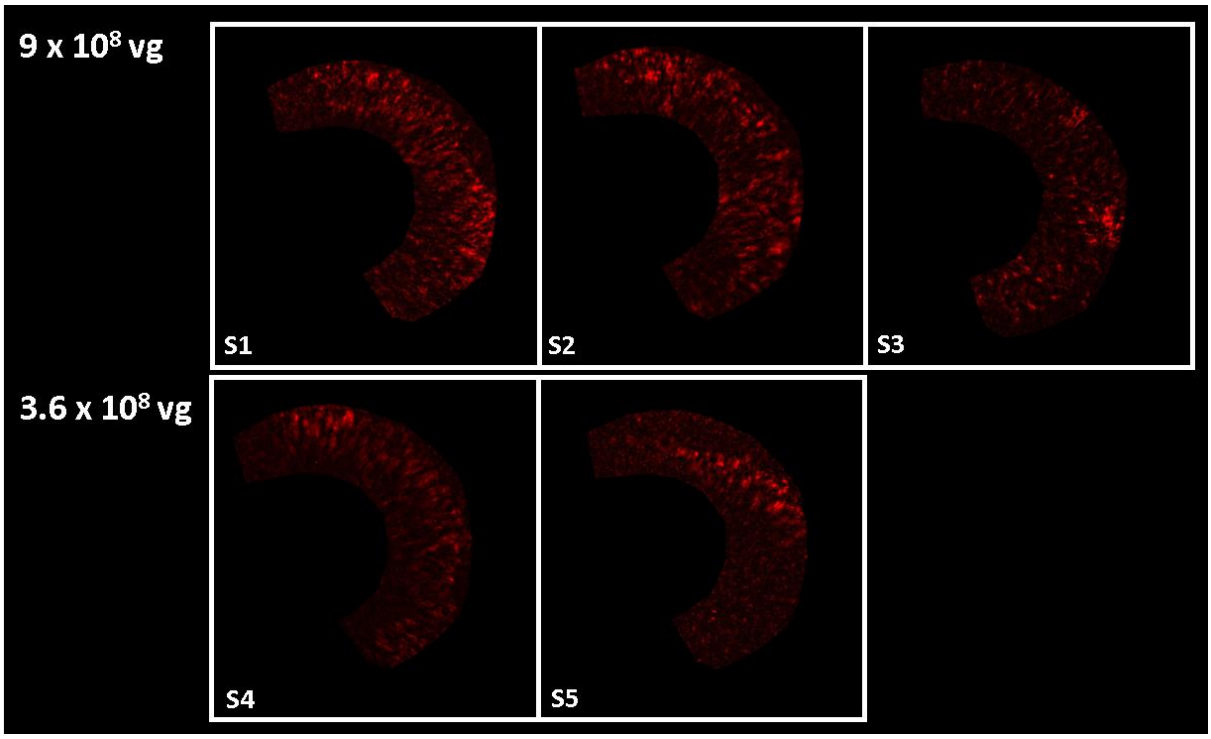

Figure 3.20. ROIs (corresponding to CA1b-CA3b regions) from slices treated with 3.6 x 10^8 vg and 9 x 10^8 vg virus loads at DIV5. 11 days after infection (DIV16). Wide-field fluorescence imaging.

We applied the same ROI (described in 3.3.2) to all five samples to ensure uniform measurement area and the selection of identical locations of CA1b-CA3b regions. We compared virus loads 11 days after AAV infection (DIV16) to get the highest signal intensity within individual neurons. As before, we evaluated mCherry fluorescent area, total fluorescence intensity and mean signal intensity.

We measured total area of hM4D-mCherry fluorescence using data acquired from five slices (Fig. 3.21). As expected, lower AVV-hM4D virus load reduced the area of the fluorescence on average two times. This decrease of total area might be caused by two factors. First, lower AAV-hM4D virus load might have lowered the number of infected pyramidal neurons. Second, lower AAV-hM4D virus load might have slowed down the expression of mCherry in individual neurons, thus less hM4D-mCherry would have been distributed inside the neuron, therefore reducing total area.

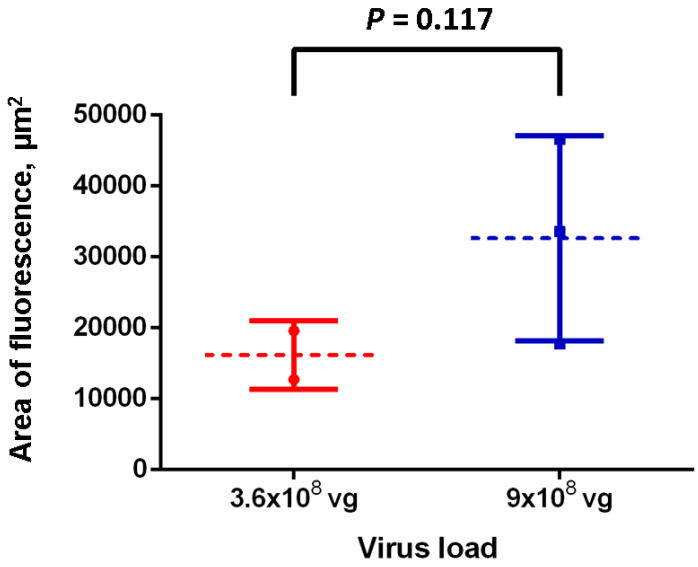

Figure 3.21. Total area of hM4D-mCherry fluorescence in organotypic slices infected with different virus loads 11 days after infection. 3,6 x 10^8 vg N = 2, 9 x 10^8 vg N = 3.

We measured total fluorescence intensity of 3,6x10^8 vg and 9x10^8 vg virus loads (Fig. 3.22). Difference of total intensity between different virus load groups was 2.1 times on average (p = 0.100). To check if the decline in total fluorescence intensity was caused only by the reduction of hM4D-mCherry-expressing neuron number area of fluorescence, mean fluorescent intensity was measured.

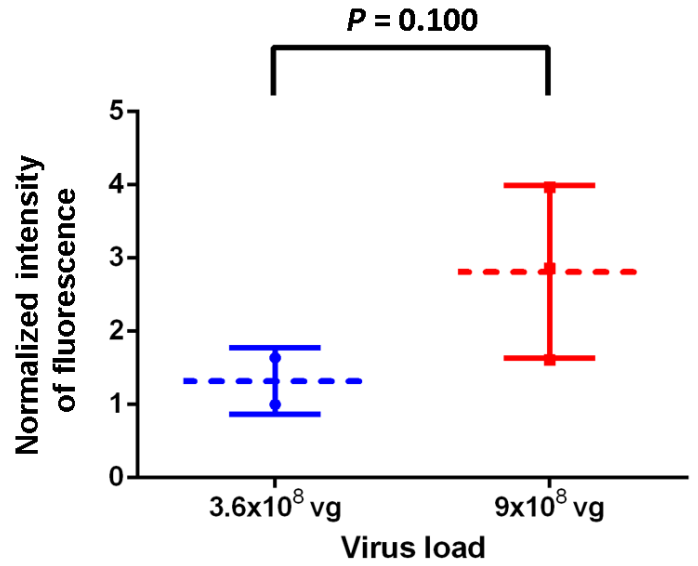

Figure 3.22. Total intensity of hM4D-mCherry fluorescence in organotypic slices infected with different virus loads 11 days after infection. 3,6 x 10^8 vg N = 2, 9 x 10^8 vg N = 3. Normalization was done by dividing the total fluorescence intensity of all points by the value of lowest total intensity.

We measured mean intensity in different virus load groups to check how reduction in virus load affected the intensity of the fluorescence within hM4D-mCherry-expressing neurons (Fig. 3.23). The reduction of virus load reduced the mean intensity only by 1.03 times (p = 0.074).

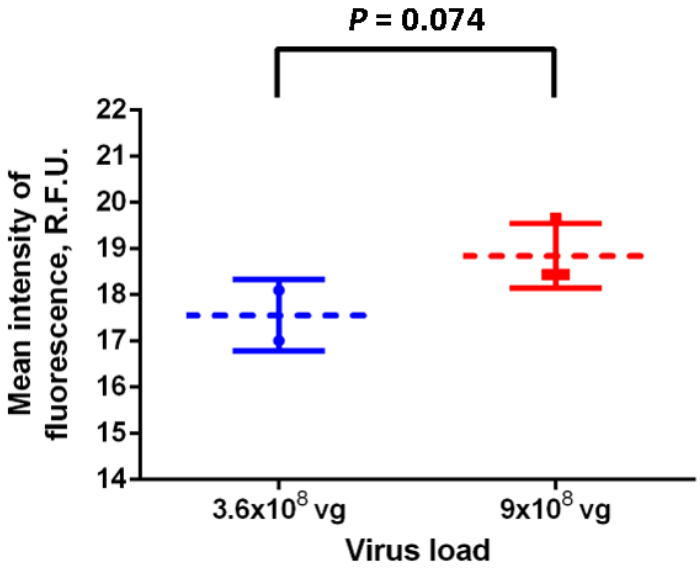

Figure 3.23. Mean intensity of hM4D-mCherry fluorescence in organotypic slices infected with different virus loads 11 days after infection. R.F.U. – relative fluorescence units. 3,6 x 10^8 vg N = 2, 9 x 10^8 vg N = 3.

Overall, the reduction of virus load lowered the area of hM4D-mCherry fluorescent signal by 50.4% on average. In contrast, the reduction of mean intensity was only 8.9%. Hence, smaller virus load (3,6 x 10^8 vg) reduced the number of hM4D-mCherry-expressing neurons and had low impact on individual neuron fluorescent intensity. This increased chances of observing isolated neuron with non-overlapping axons and dendrites. Based on this data lower (3.6 x 10^8 vg) virus load was chosen for further experiments.

3.3.4. High resolution visualization of neurons expressing hM4D-mCherry after 3,6 x 10^8 vg virus load

We have established that effective hM4D-mCherry expression requires at least 11 days after infection, but further 24 h are needed to activate the DREADD and extra three days are required to observe any changes in axon bouton and dendritic spine density and

morphology (unpublished data from our team). Hence, 3,6 x 10^8vg virus load slices analyzed in chapter 3.3.3 were cultured until DIV20, fixed and prepared for confocal imaging (Fig. 3.24) (preparation described in chapter 2.2.2.).

Figure 3.24. Timeline used for preparation of slices with 3,6 x 10^8vg AAV-hM4D virus load after DIV5 treatment for confocal imaging.

Immunofluorescent staining was applied to amplify mCherry fluorescent signal with minimal increase in background fluorescence (Supp. Fig. 2). Amplifying the signal is crucial due to low quantum yield of the mCherry compared to other frequently utilized fluorescent proteins (Shaner et al., 2005). Acquired images allowed us to observe hippocampal excitatory pyramidal neurons (Fig. 3.25 A). hM4DmCherry-expressing neurons were located close to each other with rare non-overlapping neurons (Fig. 3.25 A). Branching dendrites were seen but these were dense and overlapping (Fig. 3.25 B). However, fluorescent signal was too poor to visualize smaller structures, such as dendritic spines or axonal boutons (Fig. 3.25 B).

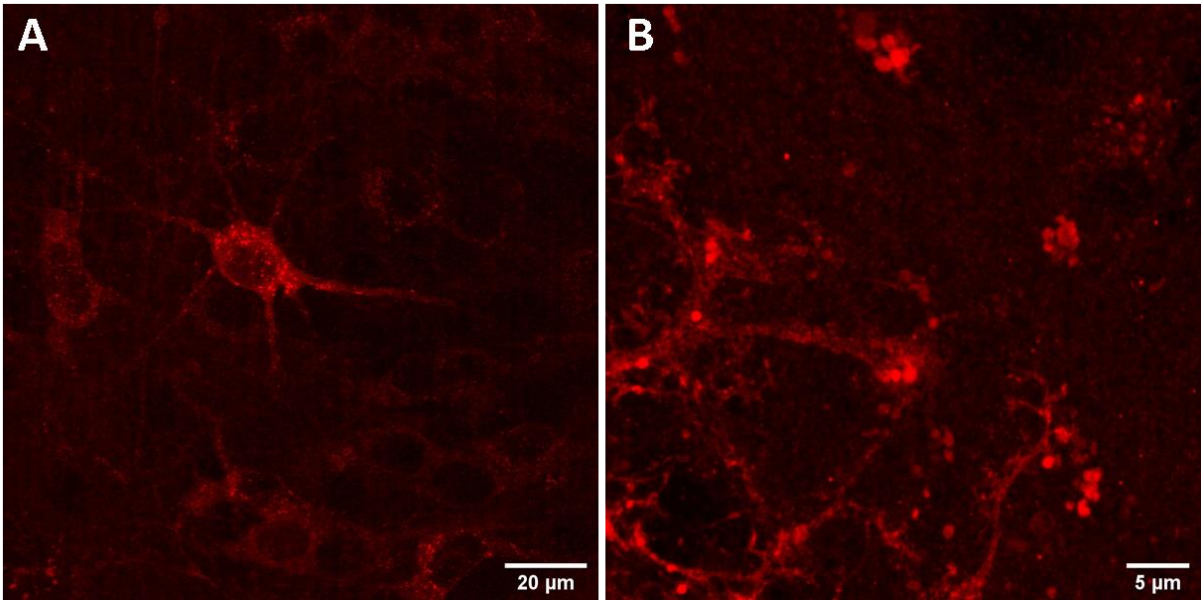

Figure 3.25. 3,6 x 10^8 vg virus load slice after DIV20. Excitatory pyramidal neuron in the CA1 region of the hippocampus. Immunofluorescent staining of mCherry was applied to amplify the signal. Neurons were visualized in red since neurons express mCherry signal amplified with Alexa568. A- excitatory pyramidal neuron. B- dense network of dendrites. A – projected from 16 planes. B – projected from 12 planes. Confocal fluorescence imaging.

Further reduction of viral load is required to reduce number of hM4D-mCherry-expressing neurons and visualize non-overlapping axons and dendrites.

3.3.5. Establishing increasing mCherry fluorescence in the neurons up to 15 days (DIV20) after infection

At this point we established that further reduction in virus load is needed to reduce density of hM4D-mCherry-expressing neurons and acquire sparsely labeled axon boutons and dendritic spines. Also, we showed the tendency for mCherry fluorescence to increase in individual cells over time. If the fluorescent signal of hM4D-mCherry kept increasing after 11 days post infection, increased culturing time might improve signal to noise ratio.

To reliably determine how hM4D-mCherry fluorescent signal intensity increases from 11 (DIV16) to 15 (DIV20) days after infection we isolated CA1b-CA3b regions (Supp. Fig. 3) and measured mean intensity of fluorescence. We used DIV5 infection of AAV-hM4D and 3,6 x 10^8 vg virus load (Fig. 3.26). This measurement was selected to analyze if increasing time of culturing after infection with AAV-hM4D by four days (from DIV16 to

DIV20) could increase fluorescence intensity in hM4D-mCherry-expressing neurons after DREADD activation at DIV16.

Figure 3.26. Timeline to analyze expression of hM4D-mCherry (3,6 x 10^8 vg virus load) from 11 (DIV16) to 15 (DIV20) days after DIV5 treatment with AAV-hM4D.

Mean intensity of fluorescence increased by 1.15 times (13 %) (p = 0.026) between day 11 (DIV16) and day 15 (DIV20) after infection (Fig. 3.27). This indicates that increase of time of culturing from 11 days to 15 days (from DIV16 to DIV20) increased mCherry signal intensity of hM4D-mCherry-expressing neurons.

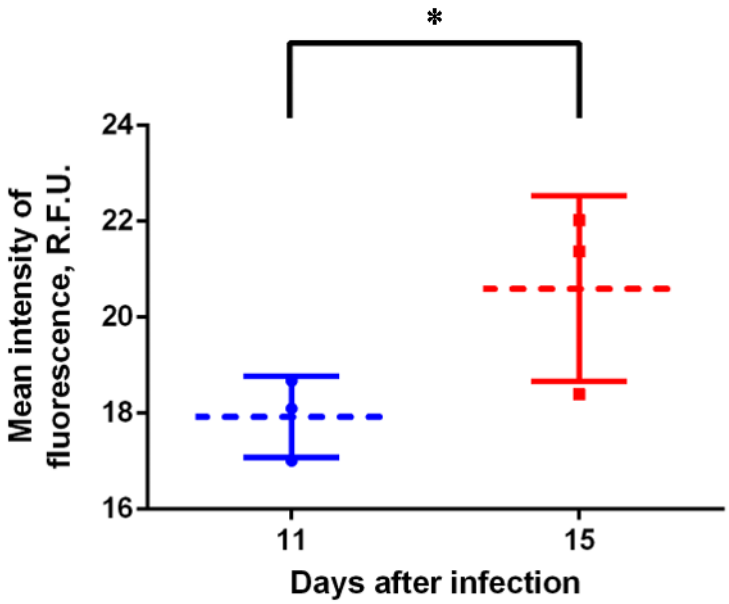

Figure 3.27. Mean intensity of hM4D-mCherry fluorescence in organotypic slices after 11 (DIV16) and 15 days (DIV20) of 3,6 x 10^8 vg virus load infection. 11 days after infection N = 3, 15 days after infection N = 3. R.F.U. – relative fluorescence units. *p < 0.05.

We measured mean intensity at 11 days (DIV16) after infection since it provides with sufficient expression of DREADDs (described in chapter 3.3.3.) and at 15 days (DIV20)

after infection since we image neurons four days after activation of DREADD. Overall, mean fluorescence intensity significantly increased from day 11 (DIV16) to day 15 (DIV21) of culturing which suggested increased mCherry fluorescence in neurons expressing hM4D-mCherry.

3.3.6. Reducing the density of hM4D-mCherry-expressing neurons and maximizing time for hM4D-mCherry expression

After analyzing hM4d-mCherry expression in infected neurons (in chapter 3.3.2 and 3.3.5) and the effect of reduced virus load for hM4D-mCherry expression in the slice, we further lowered virus load of AVV-hM4D to 1.8 x 10^8 vg to reduce the density of hM4D-mCherry-expressing neurons. This could reduce number of overlapping hM4D-mCherry-expressing neurons and help visualize axons and dendrites. We have previously observed that hM4D-mCherry signal in individual neurons increased up to 15 days after infection. Hence, we increased time of culturing to 14 days (DIV19) which corresponds with the last day of peak synaptic pruning (unpublished data from our group) (Fig. 3.28). This represents the maximum culturing period before we could apply CNO for the inhibition of neuronal activity. Neurons were then treated with CNO for 24 h and slices were fixed, stained to amplify mCherry signal and imaged at DIV23.

Figure 3.28. Experimental timeline showing reduced virus load (1.8 x 10^8 vg) after treatment of AAV-hM4D at DIV5 and increased time of culturing before CNO treatment to 14 days. .

Images of hM4D-mCherry-expressing CA1 pyramidal neurons were captured using confocal microscopy. Despite the lowered AAV-hM4D virus load on a slice to 1.8 x 10^8 vg, hM4D-mCherry-expressing neurons overlapped and were tightly packed (Fig. 3.29). Also, increased time of culturing to 18 days after infection (DIV23) with AVV-hM4D, did not

result in the accumulation of sufficient amount of mCherry to clearly visualize axons or dendrites (Fig. 3.29).

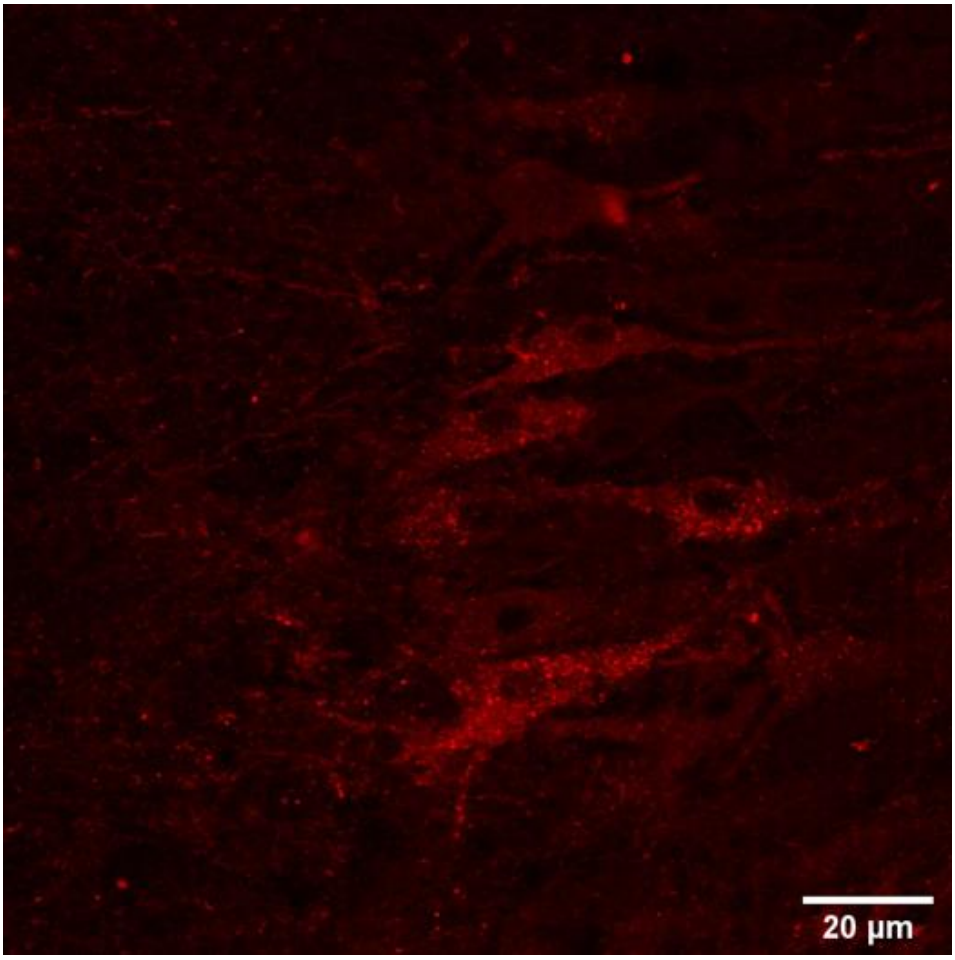

Figure 3.29. hM4D-mCherry-expressing excitatory pyramidal neurons in the CA1 region of the hippocampus. Slice was treated with 1.8 x 10^8 vg virus load and cultured for 18 days after infection (DIV23). mCherry signal was amplified with immunofluorescent staining. Image projected from 25 planes. Confocal fluorescence imaging.

3.3.7. Determining optimal day of AAV-hM4D infection for visualization of axonal boutons and dendritic spines

Based on our previous experiments and the increasing expression of our DREADD promoter CamKIIα we hypothesized that the day of infection was a more important for robust expression of DREADD than the following incubation time. To test this hypothesis the same (1.8 x 10^8 vg) virus load infections were performed on DIV5, 7, 12. Samples were then fixed,

immunofluorescent staining was performed to amplify mCherry signal and slices were imaged at DIV 23, 22, 22 accordingly (Fig. 3.30).

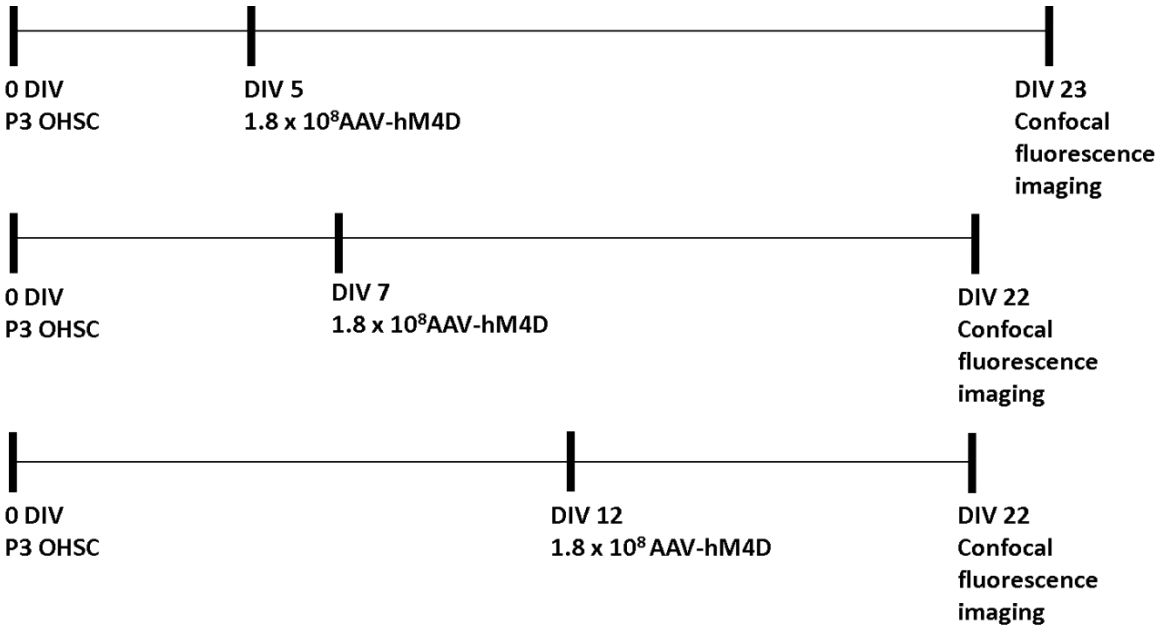

Figure 3.30. Experimental timeline used to compare the effect of date of AAV-hm4D infection. We used 1.8 x 10^8 vg virus load at DIV5, 7, 12 dates of infection.

We selected the brightest neurons in every experiment from the CA1 region of the hippocampus (Fig. 3.31). DIV5 infection showed poor mCherry signal in the somas of pyramidal neurons with almost no possibility to visualize neurites (Fig. 3.31). DIV7 infection exhibited a slight improvement with better defined shape and observable migration of mCherry into more distal parts of the neuron (Fig. 3.31). The sample infected at DIV12 provided the highest fluorescent intensity by far with fully homogeneously labeled somas and branching dendrites (Fig. 3.31). Interestingly, the sample infected at DIV12 was cultured only for 10 days after infection as compared with DIV5 which was cultured for 18 days. Overall, the time of infection had higher impact on the strength of hM4D-mCherry fluorescence compared to the length of culturing after the infection with AAV-hM4D.

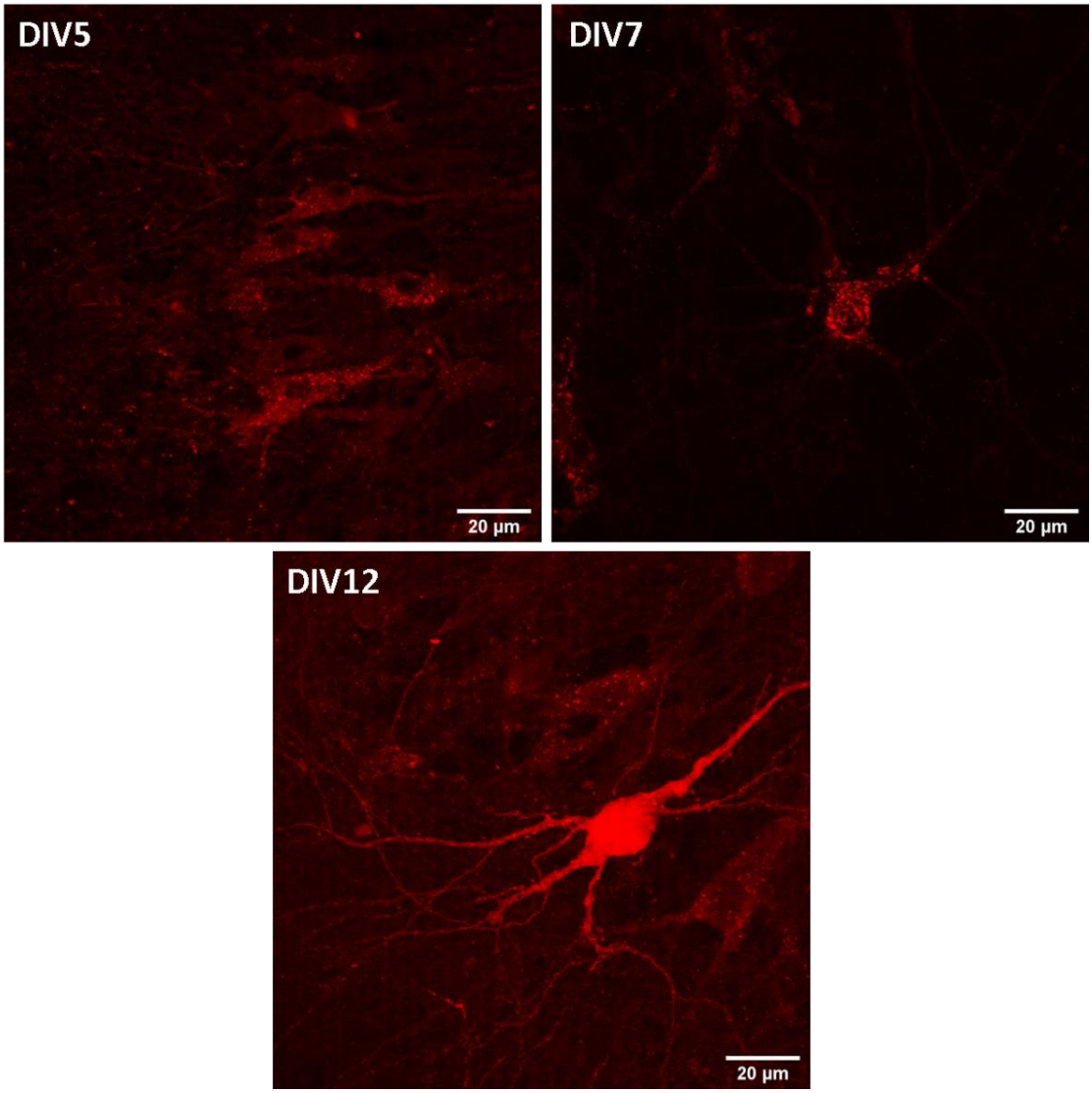

Figure 3.31. hM4D-mCherry-expressing neurons after DIV5, DIV7, DIV12 infection with 1.8 x 10^8 vg virus load. Pyramidal neurons expressing hM4D-mCherry located in CA1 region. mCherry signal was amplified using immunofluorescent staining. Top left corners show the date of AAV-hM4D infection. DIV5 image projected from 25 planes. DIV7 projected from 50 planes. DIV12 image projected from 60 planes. Confocal fluorescence imaging.

In the sample, which was infected at DIV12, branching dendrites were observed (Fig. 3.32 A), even dendritic spines could be distinguished (Fig. 3.32 B). Nevertheless, the quality of the signal was too poor to perform morphological analysis of dendritic spines.

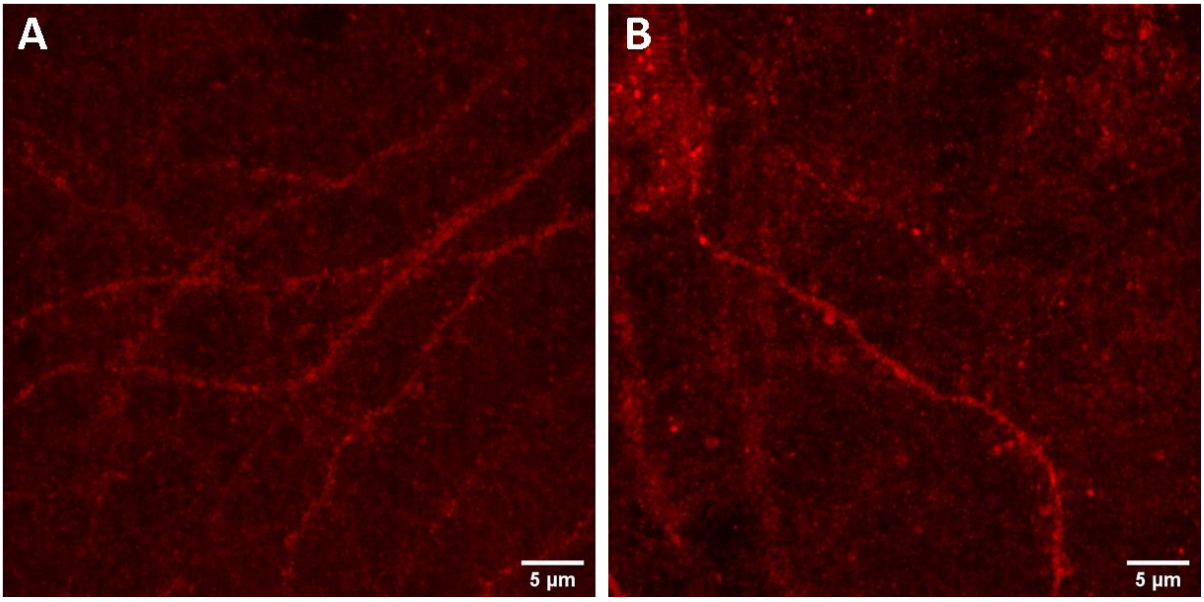

Figure 3.32. Visible dendrites after DIV12 infection with 1.8 x 10^8 vg virus load. Originating in neurons expressing hM4D-mCherry from CA1 region molecular layer. mCherry signal was amplified using immunofluorescent staining. A – branching secondary apical dendrites. B – dendritic spines can be observed protruding from the dendrite. A – projected from 47 planes. B – projected from 16 planes. Confocal fluorescence imaging.

Quantitative timeline of DREADD expression has been established with a notable increase in mCherry signal area and intensity throughout experimental period. Reduction in virus load from 9 x 10^8vg to 1.8 x 10^8 vg had minimal effect on the density of hM4D-mCherry-expressing neurons. Highest possible day of infection produced the best mCherry signal in the pyramidal neurons. In fact, the day of infection was discovered to be the most important factor for the expression of hM4d-mCherry. However, the day of infection could not be further delayed since neural activity has to be inhibited during the period of synaptic pruning.

Overall, we delayed the day of AAV-hM4D application to DIV12, increased the time culturing after infection to 15 days and reduced the virus load on a slice to 1.8 x 10^8 vg. Even though, these changes had improved the quality of the signal, morphological analysis of either dendritic spines or axonal boutons were impossible to perform due to insufficient resolution of the signal. Deficient imaging of smaller structures might be caused by high infected neuron count, low expression of hM4D-mCherry and a physical link between DREADD and fluorescent marker mCherry. Physical link allowed us to visualize only the area where the DREADD receptor was located. We had to conclude, that AAV8/2-CaMKIIα::Hm4Di(Gi)-

mCherry-WPRE-hgHp(A) DREADD construct was not suitable for high resolution imaging experiments, morphological analysis of dendritic spines or axonal boutons.

3.3.8. Co-localization of EGFP and mCherry fluorescence signals as a strategy to analyze infected neuron morphology

Even though our AVV-DREADD construct is not suitable for the quantification and morphological analysis of dendritic spines or axonal boutons, it can still be utilized to inhibit the activity of the neurons (Alexander et al., 2018). Visualizing could be performed by using different fluorescent marker. In our work we used *Thy1*::EGFP mice that have excitatory hippocampal neurons labelled with EGFP marker. EGFP exhibits excellent imaging properties with more than 2 times higher brightness and quantum yield than mCherry (Shaner et al., 2005). It does not have any known effect on the viability or activity of the neurons. Most importantly, EGFP in this mouse line is not bound by any intracellular proteins and diffuses freely and efficiently throughout the cell. The only challenge is to localize mCherry and EGFP in the same neuron and in the region of our interest (CA1, CA3). While reanalyzing images from the previous experiments a neuron with clear co-localization of mCherry and EGFP was found (Fig. 3.33).

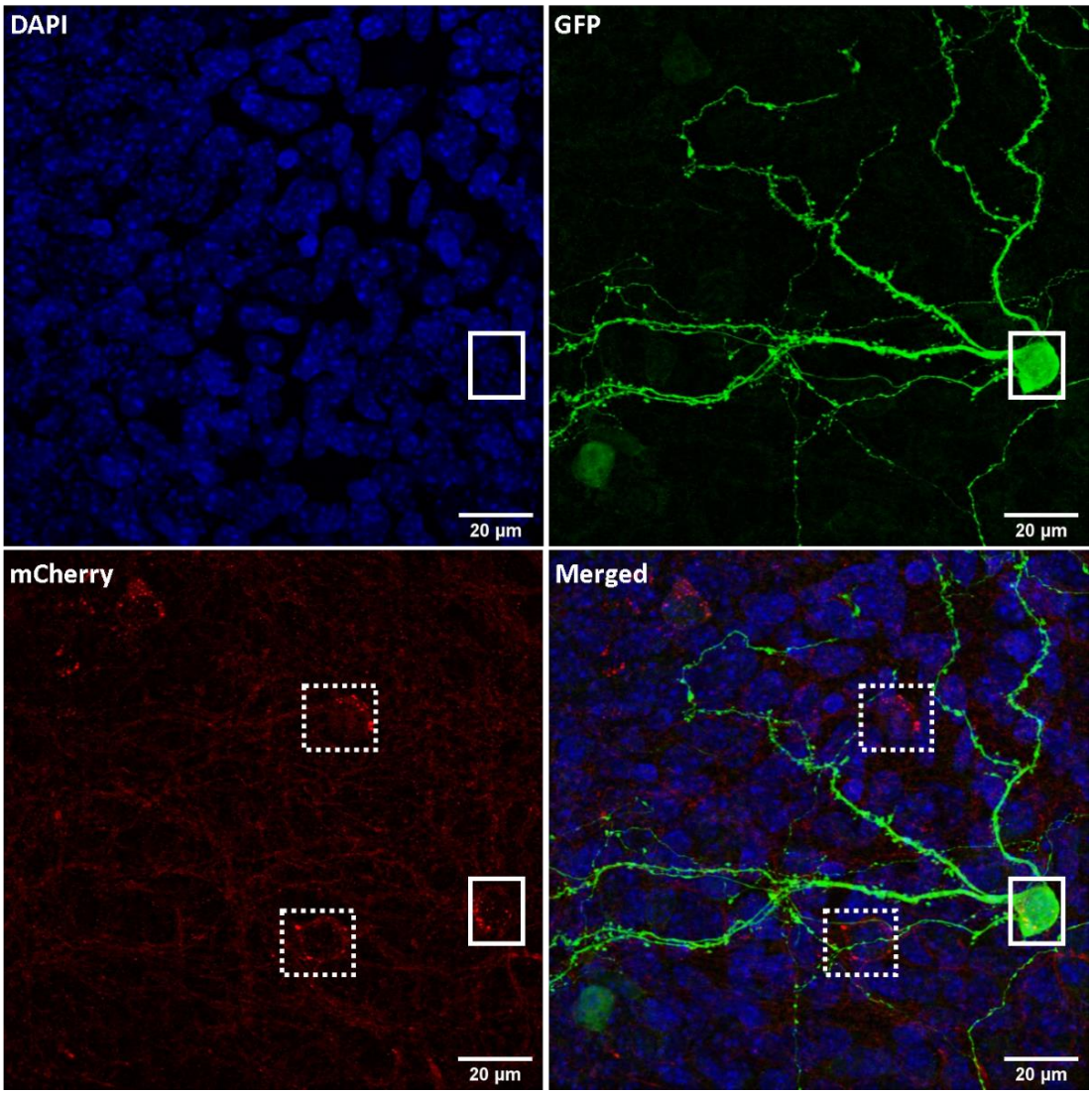

Figure 3.33. Co-localization of EGFP and mCherry signals. Slice was treated with AAV-hM4D at DIV7 with 1.8 x 10^8 vg and cultured for 15 days after infection. Solid line square shows neuron expressing mCherry and EGFP. Dotted line squares highlight neurons expressing only mCherry. Images projected from 29 planes. Confocal fluorescence imaging.

Unfortunately, this was a single neuron and subsequent experiments are required to test the feasibility of our approach. Nonetheless, this neuron shows how EGFP-mCherry co-localization can be used to obtain images of well-defined axonal boutons and dendritic spines. To achieve high number of EGFP-mCherry double positive neurons we have to increase number of both EGFP and mCherry expressing neurons. Furthermore, Feng and colleagues reports that that only less than 10% of the hippocampus excitatory neurons are expressing EGFP in heterozygous animals and the number of EGFP positive neurons could be increased by using homozygous mice (Feng et al., 2000a). Hence, future experiments are only going to

be performed using homozygous animals. Finally, to further increase chance of EGFP-mCherry co-localization 9 x 10^8 vg virus load of hM4D-mCherry is going to be used.

Summarizing all our experiments to improve the density of EGFP+/mCherry+ double positive neurons we defined the timeline of experiment presented in Fig. 3.34. Timeline encompasses DIV7 infection day with CNO treatment at 11 days post infection (DIV18). The highest used virus load of AAV-hM4D (9 x 10^8 vg) was selected to increase the density of DREADD-expressing pyramidal neurons. Homozygous EGFP animals were selected to increase number of EGFP expressing pyramidal neurons.

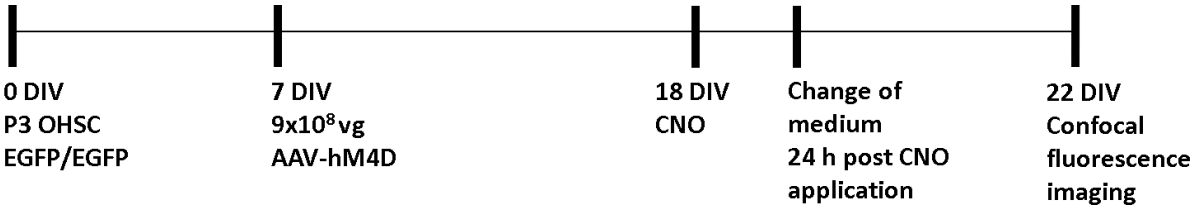

Figure 3.34. Experimental timeline constructed for mCherry-EGFP co-localization experiment. EGFP/EGFP animals were selected. We chose DIV7 day of AAV-hM4D infection with 9 x 10^8 vg. DREADD would be activated on DIV18 and could be imaged on DIV22.

To conclude, our data showed that AAV8/2-CaMKIIα::hM4Di(Gi)-mCherry-WPRE-hgHp(A) DREADD construct is not suitable for detailed imaging analysis of axonal boutons and dendritic spines. However, this AAV-hM4D construct can still be used in combination with different fluorescent labeling tools. Also, we provided timeline and conditions for future research.

4. DISCUSSION

In this study we developed tools and strategies to investigate the role of neural activity in synaptic pruning. First, we established the protocol for organotypic hippocampus slice cultures to have an experimental 3D model for morphological analysis of axonal boutons and dendritic spines. Second, we visualized active interactions between neurons and microglia. Third, we explored different conditions for expression of AAV8/2-CaMKIIα::hM4Di(Gi)-mCherry-WPRE-hgHp(A) DREADD construct. Finally, we proposed a co-localization of EGFP-mCherry signals as a strategy to analyze morphology of axonal boutons and dendritic spines of neurons with inhibited neuronal activity during the period of peak synaptic pruning.

In our OHSC protocol we used P3 *Thy1*::EGFP/+ mouse pups compared to Gogola and colleagues which used P6 – P9 animals (Gogolla et al., 2006). Using younger animals was more difficult from a technical standpoint since the tissue was more fragile. Nevertheless, the slices we made were undamaged and preserved hippocampal structure was seen up to DIV23 with no signs of degradation. Increasing number of EGFP-expressing neurons was seen during culturing, indicating healthy tissue development. Neurons matured and maintained viability with minimal cell death up to DIV23. This is similar to the results of Poindron and colleagues (Poindron et al., 2005), who cultured slices for DIV12 or Muller and colleagues (Muller et al., 1993), who reported healthy neurons in 2 – 3 week old slices. To achieve this, we significantly simplified and sped up preparation procedure. We believe that the changes we made improved previously published protocols (Gogolla et al., 2006; Simoni and Yu, 2006).

We visualized the interactions between microglia by utilizing *Thy1::EGFP*, *RC::LSL-tdTomato*, *Cx3cr1::Cre* triple transgene mouse line. Density of tdTomato-expressing microglia was controlled by application of tamoxifen. Our results were similar to Álvarez-Aznar and colleagues which reported 90% increase in tdTomato-expressing microglia after tamoxifen treatment (Álvarez-Aznar et al., 2020). We observed direct contact between neuron and microglia. This could allow to analyze active interactions between microglia and neurons and determine if microglia selectively approached and phagocytosed synapses with different activity. Weinhard and colleagues used OHSC from the same mouse line to show that microglia engulf and trogocytose synaptic material (Weinhard et al., 2018). With emerging reasearch (Hong et al., 2016) highlighting the importance of microglia for

brain development and pathological conditions, it become increasingly important to visualize neurons and microglia in one setting. We believe, that experimental setting with visible neurons and microglia could provide new insights into role of microglia in activity-mediated synaptic pruning.

We optimized conditions for AAV-hM4D expression and morphological assessment of axonal boutons and dendritic spines using AAV8/2-CaMKIIα::hM4Di(Gi)-mCherry-WPRE-hgHp(A) DREADD construct. We defined that the application of AAV-hM4D could be performed no earlier than DIV5. This contradicted the findings of Avaliani and colleagues which showed DREADD-expressing neurons after DIV0 infection (Avaliani et al., 2016) but were similar to results of Călin and colleagues which used infection at DIV3-5 (Călin et al., 2018). However, Avaliani used much higher virus load (2.49×10^{10} compared to our 9×10^{8} vg) and older animals for their OHSC (P6 – P8) (Avaliani et al., 2016). After that we established that OHSC had to be cultured for at least 11 days after infection for impactful activation of hM4D. These results were similar to Călin and Zou both of which reported two-week culturing period before activation (Călin et al., 2018; Zou et al., 2016). Aiming for sparse but sufficiently bright labelling of neurons, we reduced the density of hM4D-mCherry-expressing neurons and preserved the majority of the mCherry signal in already expressing neurons by reducing the virus load from 9×10^{8} vg to 3.6×10^{8} vg. However, mCherry signal was too weak for the visualization of axonal boutons and dendritic spines. We showed that further reduction of virus load to 1.8×10^{8} vg and prolonging post-infection incubation up to 18 days did not improve the density and the signal intensity of AAV-hM4D for the visualization of axonal boutons and dendritic spines. Delaying the infection up to DIV7 or DIV12 showed significant improvement for the labelling of dendrites and dendritic spines. Still, the mCherry signal was too weak for morphological analysis of dendritic spines. Other researchers (Avaliani et al., 2016; Călin et al., 2018) who used comparable DREADD constructs obtained similar images of DREADD-expressing neurons without sufficient resolution to visualize axonal boutons or dendritic spines. These results might be caused by a physical link between artificial receptors and fluorescent reporter proteins or due to low activity of CaMKIIα promoter that regulates DREADD expression.

Finally, we developed a strategy to inhibit neuronal activity and to visualize axonal boutons and dendritic spines using co-localization of EGFP and mCherry fluorescence in the same neuron. EGFP provided with robust signal and clearly labeled axonal boutons and dendritic spines suitable for morphological analysis (Fig. 3.4). Meanwhile mCherry signal could be used to identify neurons expressing hM4D-mCherry. Similar co-localization strategy

was used by Scofield and colleagues to check if astrocytes were expressing their DREADD of choice (rAAV5/GFAP-HA-hm3D-IRES-mCitrine) (Scofield et al., 2015). We believe this strategy would be suitable to acquire high detail images of axonal boutons and dendritic spines that had inhibited activity and to demonstrate whether the synapses with lower activity are preferentially removed during synaptic pruning.

CONCLUSIONS

1. Organotypic hippocampal slice cultures proved to be a suitable setting for the visualization of maturing neurons during the period of synaptic pruning.
2. *Thy1*::EGFP, *RC*::LSL-tdTomato, *Cx3cr1*::Cre mouse line is suitable for the visualization of direct contacts between neurons and microglia in OHSC.
3. AAV8/2-CaMKIIα::hM4Di(Gi)-mCherry-WPRE-hgHp(A) DREADD can be successfully expressed in a subset of pyramidal neurons, but the resolution is not sufficient for the visualization of axonal boutons and dendritic spines. However, the morphology of inhibited neurons could be evaluated by analyzing EGFP-mCherry co-expressing neurons.

VILNIUS UNIVERSITY

LIFE SCIENCES CENTER

Arnas Kunevičius

Master's thesis

DEVELOPING TOOLS TO INVESTIGATE NEURONAL ACTIVITY IN SYNAPTIC PRUNING

SUMMARY

During development, synaptic pruning removes excess synapses and contributes to the formation of mature neuronal network. Synaptic pruning is performed by microglia that phagocytose synaptic material. It is essential to achieve optimal neural network and healthy nervous system. The impairments of synaptic pruning were linked to a variety of pathological conditions, including schizophrenia and autism spectrum disorders. Emerging data suggests that neuronal activity regulates synaptic pruning in competition-based mechanism. To investigate the role of neuronal activity in synaptic pruning we developed experimental approaches for the inhibition of neuronal activity and their visualization. First, we established organotypic hippocampal slice culture using *Thy1*::EGFP mice to provide robust labeling of excitatory pyramidal neurons of hippocampus in maturing brain tissue. Second, we used *Thy1*::EGFP, *RC*::LSL-tdTomato, *Cx3cr1*::Cre mice to visualize direct interactions between neurons and microglia. Third, we optimized conditions to use AAV8/2-CaMKIIα::hM4Di(Gi)-mCherry-WPRE-hgHp(A) designer receptor exclusively activated by designer drugs (DREADD) to inhibit neuronal activity and visualize inhibited neurons. We determined that this DREADD construct is not suitable to perform morphological analysis of axonal boutons and dendritic spines but could be used with other neuron visualization tools. Finally, we proposed a strategy to analyze morphology of axonal boutons and dendritic spines of neurons inhibited during peak of synaptic pruning utilizing co-localization of EGFP and mCherry signals.

VILNIUS UNIVERSITETAS

GYVYBĖS MOKSLŲ CENTRAS

Arnas Kunevičius

Magistro baigiamasis darbas

METODŲ, SKIRTŲ NEURONINIO AKTYVUMO ĮTAKAI SINAPSIŲ GENĖJIME TYRIMUI, TOBULINIMAS

SANTRAUKA

Nervų sistemos vystymosi metu sinapsių genėjimas atlieka svarbų vaidmenį šalinant perteklines sinapses bei formuojant brandų nervinį audinį. Šis procesas, kurį vykdo sinapses fagocituojančios mikroglijos ląstelės, yra būtinas optimaliam nervinio signalo perdavimui bei sveikos nervų sistemos susiformavimui, o genėjimo sutrikimai yra siejami su įvairiomis patologinėmis būklėmis, tokiomis kaip šizofreniją ar autizmo spektro sutrikimai. Naujausi duomenys rodo, jog sinapsių genėjimą reguliuoja neuroninis aktyvumas, todėl šiame darbe, siekdami tirti neuronų aktyvumo įtaką sinapsių genėjimui, mes tobulinome neuronų aktyvumo slopinimui bei nuslopintų neuronų vizualizacijai skirtus įrankius. Pirmiausia, naudodami genetiškai modifikuotas *Thy1::EGFP* peles, paruošėme organotipines hipokampo pjūvių kultūras, veikiančias kaip eksperimentinė aplinka besiformuojančiam nerviniam audiniui, kuriame galime stebėti neuronus. Vėliau mes panaudojome *Thy1*::EGFP, *RC*::LSL-tdTomato, *Cx3cr1*::Cre pelių liniją tiesioginės sąveikos tarp neuronų ir mikroglijos vizualizavimui. Taip pat optimizavome sąlygas AAV8/2-CaMKIIα::hM4Di(Gi)-mCherry-WPRE-hgHp(A) sintetinių receptorių specifiškai aktyvuojamų sintetinių ligandų (DREADD) konstrukto naudojimui slopinant neuronų aktyvumą bei vizualizuojant nuslopintus neuronus. Rezultatai parodė, jog šis DREADD konstruktas nėra tinkamas aksonų gumbelių bei dendritų spygliukų morfologinei analizei, tačiau galėtų būti naudojamas su kitais neuronų vizualizacijos įrankiais. Galiausiai šiame darbe pasiūlėme strategiją sinapsių genėjimo metu nuslopintų neuronų aksonų gumbelių bei dendritų spygliukų analizei panaudojant EGFP ir mCherry signalų kolokalizaciją.

REFERENCES

1. Agulhon, C., Boyt, K.M., Xie, A.X., Friocourt, F., Roth, B.L., and McCarthy, K.D. (2013). Modulation of the autonomic nervous system and behaviour by acute glial cell G $_q$ protein-coupled receptor activation *in vivo*. J. Physiol. *591*, 5599–5609.
2. Alexander, G.M., Rogan, S.C., Abbas, A.I., Armbruster, B.N., Pei, Y., Allen, J.A., Nonneman, R.J., Hartmann, J., Moy, S.S., Nicolelis, M.A., et al. (2009a). Remote control of neuronal activity in transgenic mice expressing evolved G protein-coupled receptors. Neuron *63*, 27–39.
3. Alexander, G.M., Rogan, S.C., Abbas, A.I., Armbruster, B.N., Pei, Y., Allen, J.A., Nonneman, R.J., Hartmann, J., Moy, S.S., Nicolelis, M.A., et al. (2009b). Remote control of neuronal activity in transgenic mice expressing evolved G protein-coupled receptors. Neuron *63*, 27–39.
4. Alexander, G.M., Brown, L.Y., Farris, S., Lustberg, D., Pantazis, C., Gloss, B., Plummer, N.W., Jensen, P., and Dudek, S.M. (2018). CA2 neuronal activity controls hippocampal low gamma and ripple oscillations. Elife *7*.
5. Álvarez-Aznar, A., Martínez-Corral, I., Daubel, N., Betsholtz, C., Mäkinen, T., and Gaengel, K. (2020). Tamoxifen-independent recombination of reporter genes limits lineage tracing and mosaic analysis using CreERT2 lines. Transgenic Res. *29*, 53–68.
6. Andersson, K.B., Winer, L.H., Mørk, H.K., Molkentin, J.D., and Jaisser, F. (2010). Tamoxifen administration routes and dosage for inducible Cre-mediated gene disruption in mouse hearts. Transgenic Res. *19*, 715–725.
7. Armbruster, B.N., Li, X., Pausch, M.H., Herlitze, S., and Roth, B.L. (2007). Evolving the lock to fit the key to create a family of G protein-coupled receptors potently activated by an inert ligand. Proc. Natl. Acad. Sci. U. S. A. *104*, 5163–5168.
8. Atasoy, D., and Sternson, S.M. (2018). Chemogenetic tools for causal cellular and neuronal biology. Physiol. Rev. *98*, 391–418.
9. Avaliani, N., Andersson, M., Runegaard, A.H., Woldbye, D., and Kokaia, M. (2016). DREADDs suppress seizure-like activity in a mouse model of pharmacoresistant epileptic brain tissue. Gene Ther. *23*, 760–766.
10. Bendel, O., Bueters, T., Von Euler, M., Ove Ögren, S., Sandin, J., and Von Euler, G. (2005). Reappearance of hippocampal CA1 neurons after ischemia is associated with recovery of learning and memory. J. Cereb. Blood Flow Metab. *25*, 1586–1595.
11. Bessis, A., Béchade, C., Bernard, D., and Roumier, A. (2007). Microglial control of neuronal death and synaptic properties. Glia *55*, 233–238.
12. Betz, W.J., and Bewick, G.S. (1992). Optical analysis of synaptic vesicle recycling at the frog neuromuscular junction. Science (80-.). *255*, 200–203.
13. Boehringer, R., Polygalov, D., Huang, A.J., Middleton, S.J., Robert, V., Wintzer, M.E., Piskorowski, R.A., Chevaleyre, V., and McHugh, T.J. (2017). Chronic Loss of CA2 Transmission Leads to Hippocampal Hyperexcitability. Neuron *94*, 642-655.e9.
14. Boyden, E.S., Zhang, F., Bamberg, E., Nagel, G., and Deisseroth, K. (2005). Millisecond-timescale, genetically targeted optical control of neural activity. Nat. Neurosci. *8*, 1263–1268.
15. Brown, G.C., and Neher, J.J. (2014). Microglial phagocytosis of live neurons. Nat. Rev. Neurosci. *15*, 209–216.
16. Călin, A., Stancu, M., Zagrean, A.M., Jefferys, J.G.R., Ilie, A.S., and Akerman, C.J. (2018). Chemogenetic recruitment of specific interneurons suppresses seizure activity. Front. Cell. Neurosci. *12*.
17. Campbell, E.J., and Marchant, N.J. (2018). The use of chemogenetics in behavioural

neuroscience: receptor variants, targeting approaches and caveats. Br. J. Pharmacol. *175*, 994–1003.
18. Cancedda, L., and Poo, M.-M. (2008). Synapse Formation and Elimination: Competition and the Role of Activity. In Encyclopedia of Neuroscience, (Springer Berlin Heidelberg), pp. 3932–3938.
19. Cooper, G.M. (2000). Pathways of Intracellular Signal Transduction.
20. Cowan, W.M., Fawcett, J.W., O'Leary, D.D., and Stanfield, B.B. (1984). Regressive events in neurogenesis. Science *225*, 1258–1265.
21. Davis, B.M., Salinas-Navarro, M., Cordeiro, M.F., Moons, L., and Groef, L. De (2017). Characterizing microglia activation: A spatial statistics approach to maximize information extraction. Sci. Rep. *7*, 1–12.
22. Engel, D., and Jonas, P. (2005). Presynaptic action potential amplification by voltage-gated Na+ channels in hippocampal mossy fiber boutons. Neuron *45*, 405–417.
23. Eroglu, C., and Barres, B.A. (2010). Regulation of synaptic connectivity by glia. Nature *468*, 223–231.
24. Espósito, M.S., Piatti, V.C., Laplagne, D.A., Morgenstern, N.A., Ferrari, C.C., Pitossi, F.J., and Schinder, A.F. (2005). Neuronal differentiation in the adult hippocampus recapitulates embryonic development. J. Neurosci. *25*, 10074–10086.
25. Feng, G., Mellor, R.H., Bernstein, M., Keller-Peck, C., Nguyen, Q.T., Wallace, M., Nerbonne, J.M., Lichtman, J.W., and Sanes, J.R. (2000a). Imaging Neuronal Subsets in Transgenic Mice Expressing Multiple Spectral Variants of GFP. Neuron *28*, 41–51.
26. Feng, G., Mellor, R.H., Bernstein, M., Keller-Peck, C., Nguyen, Q.T., Wallace, M., Nerbonne, J.M., Lichtman, J.W., and Sanes, J.R. (2000b). Imaging neuronal subsets in transgenic mice expressing multiple spectral variants of GFP. Neuron *28*, 41–51.
27. Fernández-Arjona, M. del M., Grondona, J.M., Granados-Durán, P., Fernández-Llebrez, P., and López-Ávalos, M.D. (2017). Microglia morphological categorization in a rat model of neuroinflammation by hierarchical cluster and principal components analysis. Front. Cell. Neurosci. *11*.
28. Fricker, M., Neher, J.J., Zhao, J.W., Théry, C., Tolkovsky, A.M., and Brown, G.C. (2012). MFG-E8 mediates primary phagocytosis of viable neurons during neuroinflammation. J. Neurosci. *32*, 2657–2666.
29. Fu, R., Shen, Q., Xu, P., Luo, J.J., and Tang, Y. (2014). Phagocytosis of microglia in the central nervous system diseases. Mol. Neurobiol. *49*, 1422–1434.
30. Gaffield, M.A., and Betz, W.J. (2007). Imaging synaptic vesicle exocytosis and endocytosis with FM dyes. Nat. Protoc. *1*, 2916–2921.
31. Ge, S., Goh, E.L.K., Sailor, K.A., Kitabatake, Y., Ming, G.L., and Song, H. (2006). GABA regulates synaptic integration of newly generated neurons in the adult brain. Nature *439*, 589–593.
32. Gerlach, J., Donkels, C., Münzner, G., and Haas, C.A. (2016). Persistent Gliosis Interferes with Neurogenesis in Organotypic Hippocampal Slice Cultures. Front. Cell. Neurosci. *10*, 131.
33. Gogolla, N., Galimberti, I., DePaola, V., and Caroni, P. (2006). Preparation of organotypic hippocampal slice cultures for long-term live imaging. Nat. Protoc. *1*, 1165–1171.
34. Grommes, C., Lee, C.Y.D., Wilkinson, B.L., Jiang, Q., Koenigsknecht-Talboo, J.L., Varnum, B., and Landreth, G.E. (2008). Regulation of microglial phagocytosis and inflammatory gene expression by Gas6 acting on the Axl/Mer family of tyrosine kinases. J. NeuroImmune Pharmacol. *3*, 130–140.
35. Gubler, U., Monahan, J.J., Lomedico, P.T., Bhatt, R.S., Collier, K.J., Hoffman, B.J., Böhlen, P., Esch, F., Ling, N., Zeytin, F., et al. (1983). Cloning and sequence analysis of

cDNA for the precursor of human growth hormone-releasing factor, somatocrinin. Proc. Natl. Acad. Sci. U. S. A. *80*, 4311–4314.
36. Gurevich, V. V., and Gurevich, E. V. (2017). Molecular mechanisms of GPCR signaling: A structural perspective. Int. J. Mol. Sci. *18*.
37. Guru, A., Post, R.J., Ho, Y.-Y., and Warden, M.R. (2015). Making Sense of Optogenetics. Int. J. Neuropsychopharmacol. 1–8.
38. Hammond, S.L., Leek, A.N., Richman, E.H., and Tjalkens, R.B. (2017). Cellular selectivity of AAV serotypes for gene delivery in neurons and astrocytes by neonatal intracerebroventricular injection. PLoS One *12*.
39. Hashimoto, K., and Kano, M. (2013). Synapse elimination in the developing cerebellum. Cell. Mol. Life Sci. *70*, 4667–4680.
40. Hashimoto, K., Ichikawa, R., Kitamura, K., Watanabe, M., and Kano, M. (2009a). Translocation of a "Winner" Climbing Fiber to the Purkinje Cell Dendrite and Subsequent Elimination of "Losers" from the Soma in Developing Cerebellum. Neuron *63*, 106–118.
41. Hashimoto, K., Yoshida, T., Sakimura, K., Mishina, M., Watanabe, M., and Kano, M. (2009b). Influence of parallel fiber–Purkinje cell synapse formation on postnatal development of climbing fiber–Purkinje cell synapses in the cerebellum. Neuroscience *162*, 601–611.
42. Hashimoto, K., Tsujita, M., Miyazaki, T., Kitamura, K., Yamazaki, M., Shin, H.-S., Watanabe, M., Sakimura, K., and Kano, M. (2011). Postsynaptic P/Q-type Ca2+ channel in Purkinje cell mediates synaptic competition and elimination in developing cerebellum. Proc. Natl. Acad. Sci. *108*, 9987–9992.
43. Heck, N., and Benavides-Piccione, R. (2015). Editorial: Dendritic spines: From shape to function. Front. Neuroanat. *9*, 1–3.
44. Hong, S., Dissing-Olesen, L., and Stevens, B. (2016). New insights on the role of microglia in synaptic pruning in health and disease. Curr. Opin. Neurobiol. *36*, 128–134.
45. Jang, S., Kim, H., Kim, H.-J., Lee, S.K., Kim, E.W., Namkoong, K., and Kim, E. (2018). Long-Term Culture of Organotypic Hippocampal Slice from Old 3xTg-AD Mouse: An ex vivo Model of Alzheimer's Disease. Psychiatry Investig. *15*, 205–213.
46. Jann, M.W., Lam, Y.W.F., and Chang, W.H. (1994). Rapid formation of clozapine in guinea-pigs and man following clozapine-N-oxide administration. Arch. Int. Pharmacodyn. Ther. *328*, 243–250.
47. Jawaid, S., Kidd, G.J., Wang, J., Swetlik, C., Dutta, R., and Trapp, B.D. (2018). Alterations in CA1 hippocampal synapses in a mouse model of fragile X syndrome. Glia *66*, 789–800.
48. Johnson, J.M., and Betz, W.J. (2008). The color of lactotroph secretory granules stained with FM1-43 depends on dye concentration. Biophys. J. *94*, 3167–3177.
49. Kelly, P.T., and Vernon, P. (1985). Changes in the subcellular distribution of calmodulin-kinase II during brain development. Dev. Brain Res. *18*, 211–224.
50. Kettenmann, H., Hanisch, U.-K., Noda, M., and Verkhratsky, A. (2011). Physiology of Microglia. Physiol. Rev. *91*, 461–553.
51. van Keulen, S.C., and Rothlisberger, U. (2017). Exploring the inhibition mechanism of adenylyl cyclase type 5 by n-terminal myristoylated Gαi1. PLoS Comput. Biol. *13*.
52. Koyama, R., Wu, Y., Bialas, A.R., Thompson, A., Welsh, C.A., Frouin, A., Chen, C., and Stevens, B. (2017). A new organotypic model of synaptic competition reveals activity-dependent localization of C1q. BioRxiv 118646.
53. Kraszewski, K., Mundigl, O., Daniell, L., Verderio, C., Matteoli, M., and De Camilli, P. (1995). Synaptic vesicle dynamics in living cultured hippocampal neurons visualized with CY3-conjugated antibodies directed against the lumenal domain of synaptotagmin.

J. Neurosci. *15*, 4328–4342.
54. Kravitz, A. V., and Bonci, A. (2013). Optogenetics, physiology, and emotions. Front. Behav. Neurosci. *7*.
55. Lai, K.O., and Ip, N.Y. (2013). Structural plasticity of dendritic spines: The underlying mechanisms and its dysregulation in brain disorders. Biochim. Biophys. Acta - Mol. Basis Dis. *1832*, 2257–2263.
56. Laplagne, D.A., Kamienkowski, J.E., Espósito, M.S., Piatti, V.C., Zhao, C., Gage, F.H., and Schinder, A.F. (2007). Similar GABAergic inputs in dentate granule cells born during embryonic and adult neurogenesis. Eur. J. Neurosci. *25*, 2973–2981.
57. Lehrman, E.K., Wilton, D.K., Litvina, E.Y., Welsh, C.A., Chang, S.T., Frouin, A., Walker, A.J., Heller, M.D., Umemori, H., Chen, C., et al. (2018). CD47 Protects Synapses from Excess Microglia-Mediated Pruning during Development. Neuron *100*, 120-134.e6.
58. Leslie, J.H., and Nedivi, E. (2011). Activity-regulated genes as mediators of neural circuit plasticity. Prog. Neurobiol. *94*, 223–237.
59. Li, W. (2012). Eat-me signals: Keys to molecular phagocyte biology and "appetite" control. J. Cell. Physiol. *227*, 1291.
60. Li, G., and Pleasure, S.J. (2013). Migration in the Hippocampus. In Cellular Migration and Formation of Neuronal Connections, (Elsevier Inc.), pp. 331–343.
61. Linsley, J.W., Tripathi, A., Epstein, I., Schmunk, G., Mount, E., Campioni, M., Oza, V., Barch, M., Javaherian, A., Nowakowski, T.J., et al. (2019). Automated four-dimensional long term imaging enables single cell tracking within organotypic brain slices to study neurodevelopment and degeneration. Commun. Biol. *2*, 1–13.
62. Llinas, R., and Nicholson, C. (1975). Calcium Role in Depolarization-Secretion Coupling: An Aequorin Study in Squid Giant Synapse (tetraethylammonium/tetrodotoxin/suppression potential).
63. López, A.J., Kramár, E., Matheos, D.P., White, A.O., Kwapis, J., Vogel-Ciernia, A., Sakata, K., Espinoza, M., and Wood, M.A. (2016a). Promoter-Specific Effects of DREADD Modulation on Hippocampal Synaptic Plasticity and Memory Formation. J. Neurosci. *36*, 3588.
64. López, A.J., Kramár, E., Matheos, D.P., White, A.O., Kwapis, J., Vogel-Ciernia, A., Sakata, X.K., Espinoza, M., and Wood, M.A. (2016b). Promoter-Specific Effects of DREADD Modulation on Hippocampal Synaptic Plasticity and Memory Formation.
65. Lorenzetto, E., Caselli, L., Feng, G., Yuan, W., Nerbonne, J.M., Sanes, J.R., and Buffelli, M. (2009). Genetic perturbation of postsynaptic activity regulates synapse elimination in developing cerebellum. Proc. Natl. Acad. Sci. *106*, 16475–16480.
66. Low, L.K., Liu, X.-B., Faulkner, R.L., Coble, J., and Cheng, H.-J. (2008). Plexin signaling selectively regulates the stereotyped pruning of corticospinal axons from visual cortex. Proc. Natl. Acad. Sci. U. S. A. *105*, 8136–8141.
67. Lu, Q., Rau, T.F., Harris, V., Johnson, M., Poulsen, D.J., and Black, S.M. (2011). Increased p38 mitogen-activated protein kinase signaling is involved in the oxidative stress associated with oxygen and glucose deprivation in neonatal hippocampal slice cultures. Eur. J. Neurosci. *34*, 1093–1101.
68. Luche, H., Weber, O., Nageswara Rao, T., Blum, C., and Fehling, H.J. (2007). Faithful activation of an extra-bright red fluorescent protein in "knock-in" Cre-reporter mice ideally suited for lineage tracing studies. Eur. J. Immunol. *37*, 43–53.
69. Lyon, L. (2013). Optogenetics. Mater. Methods *3*.
70. Markwardt, S.J., Wadiche, J.I., and Overstreet-Wadiche, L.S. (2009). Input-specific GABAergic signaling to newborn neurons in adult dentate gyrus. J. Neurosci. *29*, 15063–15072.

71. Mayilyan, K.R., Weinberger, D.R., and Sim, R.B. (2008). The complement system in schizophrenia. Drug News Perspect. *21*, 200–210.
72. Michaelides, M., and Hurd, Y.L. (2015). Chemogenetics: DREADDs. In Neuroscience in the 21st Century, (Springer New York), pp. 1–10.
73. Miyazawa, K., Jeon, J.K., Noguchi, T., Ito, K., and Hashimoto, K. (1987). Distribution of tetrodotoxin in the tissues of the flatworm Planocera multitentaculata (Platyhelminthes). Toxicon *25*, 975–980.
74. Montminy, M.R., Gonzalez, G.A., and Yamamoto, K.K. (1990). Regulation of camp-inducible genes by creb. Trends Neurosci. *13*, 184–188.
75. Muller, D., Buchs, P.A., and Stoppini, L. (1993). Time course of synaptic development in hippocampal organotypic cultures. Dev. Brain Res. *71*, 93–100.
76. Murthy, V.N., Schikorski, T., Stevens, C.F., and Zhu, Y. (2001). Inactivity produces increases in neurotransmitter release and synapse size. Neuron *32*, 673–682.
77. Nagel, G., Szellas, T., Huhn, W., Kateriya, S., Adeishvili, N., Berthold, P., Ollig, D., Hegemann, P., and Bamberg, E. (2003). Channelrhodopsin-2, a directly light-gated cation-selective membrane channel. Proc. Natl. Acad. Sci. U. S. A. *100*, 13940–13945.
78. Nakatomi, H., Kuriu, T., Okabe, S., Yamamoto, S. ichi, Hatano, O., Kawahara, N., Tamura, A., Kirino, T., and Nakafuku, M. (2002). Regeneration of hippocampal pyramidal neurons after ischemic brain injury by recruitment of endogenous neural progenitors. Cell *110*, 429–441.
79. Neher, E., and Sakaba, T. (2008). Multiple Roles of Calcium Ions in the Regulation of Neurotransmitter Release. Neuron *59*, 861–872.
80. Nicotera, P., and Rossi, A.D. (1994). Nuclear Ca2+: physiological regulation and role in apoptosis. Mol. Cell. Biochem. *135*, 89–98.
81. Oesterhelt, D., and Stoeckenius, W. (1973). Functions of a new photoreceptor membrane. Proc. Natl. Acad. Sci. U. S. A. *70*, 2853–2857.
82. Okazawa, H., Motegi, S., Ohyama, N., Ohnishi, H., Tomizawa, T., Kaneko, Y., Oldenborg, P.-A., Ishikawa, O., and Matozaki, T. (2005). Negative Regulation of Phagocytosis in Macrophages by the CD47-SHPS-1 System. J. Immunol. *174*, 2004–2011.
83. Oliver, A.E., Baker, G.A., Fugate, R.D., Tablin, F., and Crowe, J.H. (2000). Effects of temperature on calcium-sensitive fluorescent probes. Biophys. J. *78*, 2116–2126.
84. Paolicelli, R.C., Bolasco, G., Pagani, F., Maggi, L., Scianni, M., Panzanelli, P., Giustetto, M., Ferreira, T.A., Guiducci, E., Dumas, L., et al. (2011). Synaptic pruning by microglia is necessary for normal brain development. Science (80-.). *333*, 1456–1458.
85. Paredes, R.M., Etzler, J.C., Watts, L.T., Zheng, W., and Lechleiter, J.D. (2008). Chemical calcium indicators. Methods *46*, 143–151.
86. Park, H., and Poo, M. (2013a). Neurotrophin regulation of neural circuit development and function. Nat. Rev. Neurosci. *14*, 7–23.
87. Park, H., and Poo, M. (2013b). Neurotrophin regulation of neural circuit development and function. Nat. Rev. Neurosci. *14*, 7–23.
88. Pati, S., Salvi, S.S., Kallianpur, M., Vaidya, B., Banerjee, A., Maiti, S., Clement, J.P., and Vaidya, V.A. (2019). Chemogenetic activation of excitatory neurons alters hippocampal neurotransmission in a dose-dependent manner. ENeuro.
89. Piatti, V.C., Davies-Sala, M.G., Espósito, M.S., Mongiat, L.A., Trinchero, M.F., and Schinder, A.F. (2011). The timing for neuronal maturation in the adult hippocampus is modulated by local network activity. J. Neurosci. *31*, 7715–7728.
90. Poindron, P., Piguet, P., and Förster, E. (2005). New methods for culturing cells from nervous tissues (Karger).
91. Presumey, J., Bialas, A.R., and Carroll, M.C. (2017). Complement System in Neural

Synapse Elimination in Development and Disease. In Advances in Immunology, (Academic Press Inc.), pp. 53–79.
92. Rajagopal, S., and Shenoy, S.K. (2018). GPCR desensitization: Acute and prolonged phases. Cell. Signal. *41*, 9–16.
93. Riccomagno, M.M., and Kolodkin, A.L. (2015). Sculpting neural circuits by axon and dendrite pruning. Annu. Rev. Cell Dev. Biol. *31*, 779–805.
94. Richards, D.A., Guatimosim, C., and Betz, W.J. (2000). Two endocytic recycling routes selectively fill two vesicle pools in frog motor nerve terminals. Neuron *27*, 551–559.
95. Richards, D.A., Bai, J., and Chapman, E.R. (2005). Two modes of exocytosis at hippocampal synapses revealed by rate of FM1-43 efflux from individual vesicles. J. Cell Biol. *168*, 929–939.
96. Rivest, S. (2018). A "don't eat me" immune signal protects neuronal connections. Nature *563*, 42–43.
97. Roth, B.L. (2016). DREADDs for Neuroscientists. Neuron *89*, 683–694.
98. Rubenstein, J.L.R., and Rakic, P. (2013). Cellular Migration and Formation of Neuronal Connections (Elsevier Inc.).
99. Sassone-Corsi, P. (2012). The Cyclic AMP pathway. Cold Spring Harb. Perspect. Biol. *4*.
100. Schafer, D.P., Lehrman, E.K., Kautzman, A.G., Koyama, R., Mardinly, A.R., Yamasaki, R., Ransohoff, R.M., Greenberg, M.E., Barres, B.A., and Stevens, B. (2012). Microglia Sculpt Postnatal Neural Circuits in an Activity and Complement-Dependent Manner. Neuron *74*, 691–705.
101. Schuldiner, O., and Yaron, A. (2015). Mechanisms of developmental neurite pruning. Cell. Mol. Life Sci. *72*, 101–119.
102. Sci, W.C.-A.J.M., and 1939, undefined A law of denervation. Ci.Nii.Ac.Jp.
103. Scofield, M.D., Boger, H.A., Smith, R.J., Li, H., Haydon, P.G., and Kalivas, P.W. (2015). Gq-DREADD Selectively Initiates Glial Glutamate Release and Inhibits Cue-induced Cocaine Seeking. Biol. Psychiatry *78*, 441–451.
104. Seo, J.W., Kim, J.H., Kim, J.H., Seo, M., Han, H.S., Park, J., and Suk, K. (2012). Time-dependent effects of hypothermia on microglial activation and migration. J. Neuroinflammation *9*, 694.
105. Shaner, N.C., Steinbach, P.A., and Tsien, R.Y. (2005). A guide to choosing fluorescent proteins.
106. SHIMOMURA, O., JOHNSON, F.H., and SAIGA, Y. (1962). Extraction, purification and properties of aequorin, a bioluminescent. J. Cell. Comp. Physiol. *59*, 223–239.
107. Simoni, A. De, and Yu, L.M. (2006). Preparation of organotypic hippocampal slice cultures: interface method. Nat. Protoc. 2006 13 *1*, 1439–1445.
108. Šišková, Z., and Tremblay, M.-È. (2013). Microglia and Synapse: Interactions in Health and Neurodegeneration. Neural Plast. *2013*.
109. Sternson, S.M., and Roth, B.L. (2014). Chemogenetic Tools to Interrogate Brain Functions. Annu. Rev. Neurosci. *37*, 387–407.
110. Thestrup, T., Litzlbauer, J., Bartholomäus, I., Mues, M., Russo, L., Dana, H., Kovalchuk, Y., Liang, Y., Kalamakis, G., Laukat, Y., et al. (2014). Optimized ratiometric calcium sensors for functional in vivo imaging of neurons and T lymphocytes. Nat. Methods *11*, 175–182.
111. Tierney, A.L., and Nelson, C.A. (2009). Brain Development and the Role of Experience in the Early Years. Zero Three *30*, 9–13.
112. Tillo, M., Ruhrberg, C., and Mackenzie, F. (2012). Emerging roles for semaphorins and VEGFs in synaptogenesis and synaptic plasticity. Cell Adh. Migr. *6*, 541–546.
113. Toth, A.B., Terauchi, A., Zhang, L.Y., Johnson-Venkatesh, E.M., Larsen, D.J., Sutton, M.A., and Umemori, H. (2013). Synapse maturation by activity-dependent ectodomain

shedding of SIRPα. Nat. Neurosci. *16*, 1417–1425.
114. Trzaskowski, B., Latek, D., Yuan, S., Ghoshdastider, U., Debinski, A., and Filipek, S. (2012). Action of Molecular Switches in GPCRs - Theoretical and Experimental Studies. Curr. Med. Chem. *19*, 1090–1109.
115. Tuscher, J.J., Taxier, L.R., Fortress, A.M., and Frick, K.M. (2018). Chemogenetic inactivation of the dorsal hippocampus and medial prefrontal cortex, individually and concurrently, impairs object recognition and spatial memory consolidation in female mice. Neurobiol. Learn. Mem. *156*, 103–116.
116. Tuteja, N. (2009). Signaling through G protein coupled receptors. Plant Signal. Behav. *4*, 942–947.
117. Tye, K.M., Prakash, R., Kim, S.Y., Fenno, L.E., Grosenick, L., Zarabi, H., Thompson, K.R., Gradinaru, V., Ramakrishnan, C., and Deisseroth, K. (2011). Amygdala circuitry mediating reversible and bidirectional control of anxiety. Nature *471*, 358–362.
118. Urban, D.J., and Roth, B.L. (2015). DREADDs (Designer Receptors Exclusively Activated by Designer Drugs): Chemogenetic Tools with Therapeutic Utility. Annu. Rev. Pharmacol. Toxicol. *55*, 399–417.
119. Vlasov, K., Van Dort, C.J., and Solt, K. (2018). Optogenetics and Chemogenetics. In Methods in Enzymology, (Academic Press Inc.), pp. 181–196.
120. Wadiche, L.O., Bromberg, D.A., Bensen, A.S.L., and Westbrook, G.L. (2005). GABAergic signaling to newborn neurons in dentate gyrus. J. Neurophysiol. *94*, 4528–4532.
121. Wake, H., Moorhouse, A.J., and Nabekura, J. (2012). Functions of microglia in the central nervous system-beyond the immune response. Neuron Glia Biol. *7*, 47–53.
122. Wakita, M., Kotani, N., and Akaike, N. (2015). Tetrodotoxin abruptly blocks excitatory neurotransmission in mammalian CNS. Toxicon *103*, 12–18.
123. Watanabe, M., and Kano, M. (2011). Climbing fiber synapse elimination in cerebellar Purkinje cells. Eur. J. Neurosci. *34*, 1697–1710.
124. Weinhard, L., di Bartolomei, G., Bolasco, G., Machado, P., Schieber, N.L., Neniskyte, U., Exiga, M., Vadisiute, A., Raggioli, A., Schertel, A., et al. (2018). Microglia remodel synapses by presynaptic trogocytosis and spine head filopodia induction. Nat. Commun. *9*, 1228.
125. Weissleder, C., Fung, S.J., Wong, M.W., Barry, G., Double, K.L., Halliday, G.M., Webster, M.J., and Weickert, C.S. (2016). Decline in proliferation and immature neuron markers in the human subependymal zone during aging: Relationship to EGF- and FGF-related transcripts. Front. Aging Neurosci. *8*.
126. Wu, Y., Dissing-Olesen, L., MacVicar, B.A., and Stevens, B. (2015). Microglia: Dynamic Mediators of Synapse Development and Plasticity. Trends Immunol. *36*, 605–613.
127. Yan, K., Gao, L.N., Cui, Y.L., Zhang, Y., and Zhou, X. (2016). The cyclic AMP signaling pathway: Exploring targets for successful drug discovery (review). Mol. Med. Rep. *13*, 3715–3723.
128. Yi Liu, Wenbin Guo, Yan Zhang, Luxian Lv, Feihu Hu, Renrong Wu, and Jingping Zhao (2018). Decreased Resting-State Interhemispheric Functional Connectivity Correlated with Neurocognitive Deficits in Drug-Naive First-Episode Adolescent-Onset Schizophrenia. Int. J. Neuropsychopharmacol. *21*, 33–41.
129. Yizhar, O., Fenno, L.E., Davidson, T.J., Mogri, M., and Deisseroth, K. (2011). Optogenetics in Neural Systems. Neuron *71*, 9–34.
130. Yu, F., and Schuldiner, O. (2014). Axon and dendrite pruning in Drosophila. Curr. Opin. Neurobiol. *27*, 192–198.
131. Zhan, Y., Paolicelli, R.C., Sforazzini, F., Weinhard, L., Bolasco, G., Pagani, F.,

Vyssotski, A.L., Bifone, A., Gozzi, A., Ragozzino, D., et al. (2014). Deficient neuron-microglia signaling results in impaired functional brain connectivity and social behavior. Nat. Neurosci. *17*, 400–406.
132. Zhao, X.F., Alam, M.M., Liao, Y., Huang, T., Mathur, R., Zhu, X., and Huang, Y. (2019). Targeting microglia using Cx3cr1-Cre lines: Revisiting the specificity. ENeuro *6*, 1–11.
133. Zhong, Z.A., Sun, W., Chen, H., Zhang, H., Lay, Y.A.E., Lane, N.E., and Yao, W. (2015). Optimizing tamoxifen-inducible Cre/loxp system to reduce tamoxifen effect on bone turnover in long bones of young mice. Bone *81*, 614–619.
134. Zhu, H., and Roth, B.L. (2014). Silencing Synapses with DREADDs. Neuron *82*, 723–725.
135. Zhu, H., Pleil, K.E., Urban, D.J., Moy, S.S., Kash, T.L., and Roth, B.L. (2014). Chemogenetic inactivation of ventral hippocampal glutamatergic neurons disrupts consolidation of contextual fear memory. Neuropsychopharmacology *39*, 1880–1892.
136. Zou, D., Chen, L., Deng, D., Jiang, D., Dong, F., McSweeney, C., Zhou, Y., Liu, L., Chen, G., Wu, Y., et al. (2016). DREADD in Parvalbumin Interneurons of the Dentate Gyrus Modulates Anxiety, Social Interaction and Memory Extinction. Curr. Mol. Med. *16*, 91–102.
137. Zucker, R.S. (1999). Calcium- and activity-dependent synaptic plasticity. Curr. Opin. Neurobiol. *9*, 305–313.
138. Zufferey, R., Donello, J.E., Trono, D., and Hope, T.J. (1999). Woodchuck Hepatitis Virus Posttranscriptional Regulatory Element Enhances Expression of Transgenes Delivered by Retroviral Vectors. J. Virol. *73*, 2886–2892.

SUPPLEMENTARY DATA

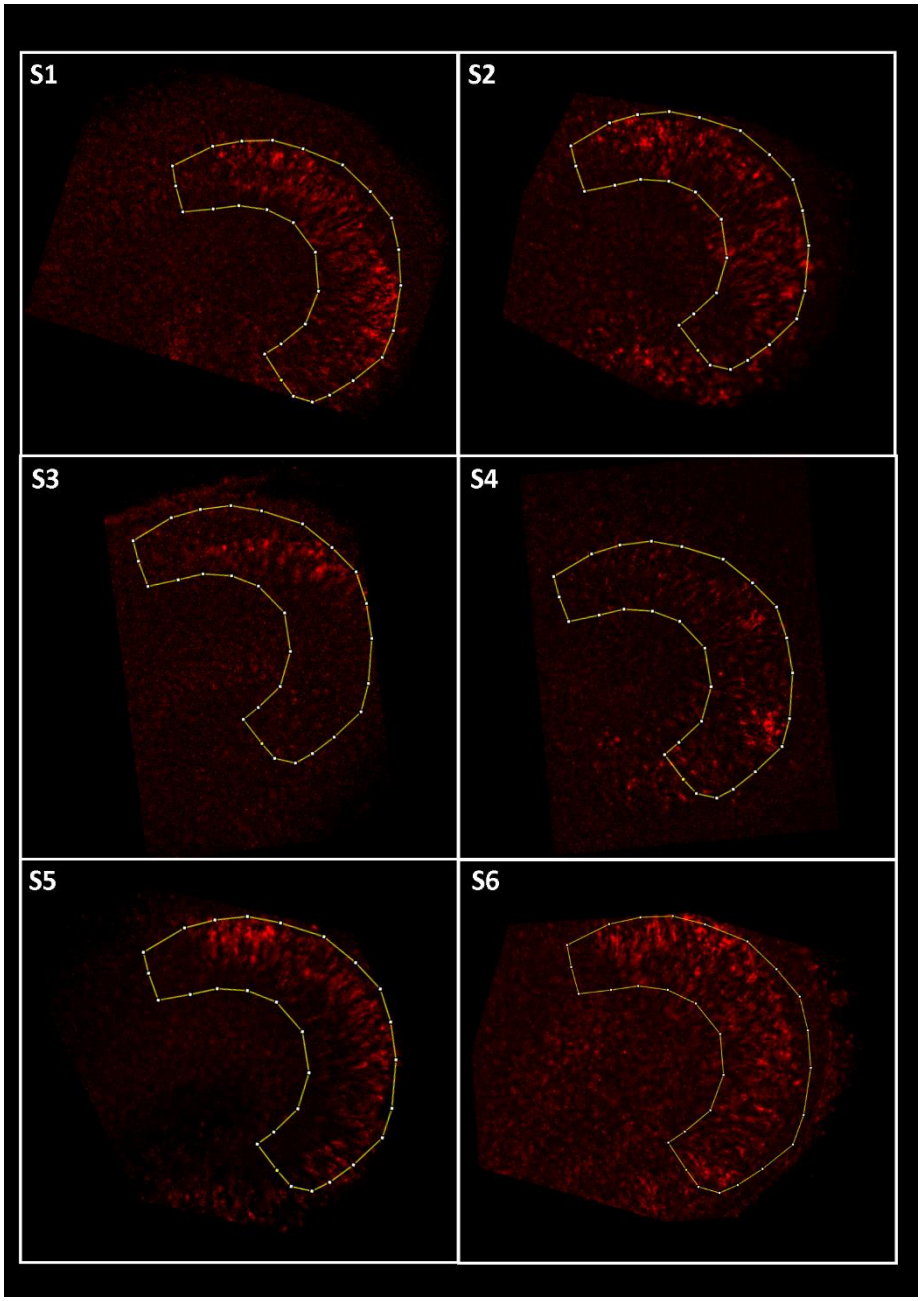

Supplementary Figure 1. Designed ROI applied to rotated OHSC images. This ensures uniform selection of CA1b-CA3b regions. Slices after 11 days of culturing with 9 x 10^8 vg and 3.6 x 10^8 vg virus loads. Wide-field fluorescence imaging.

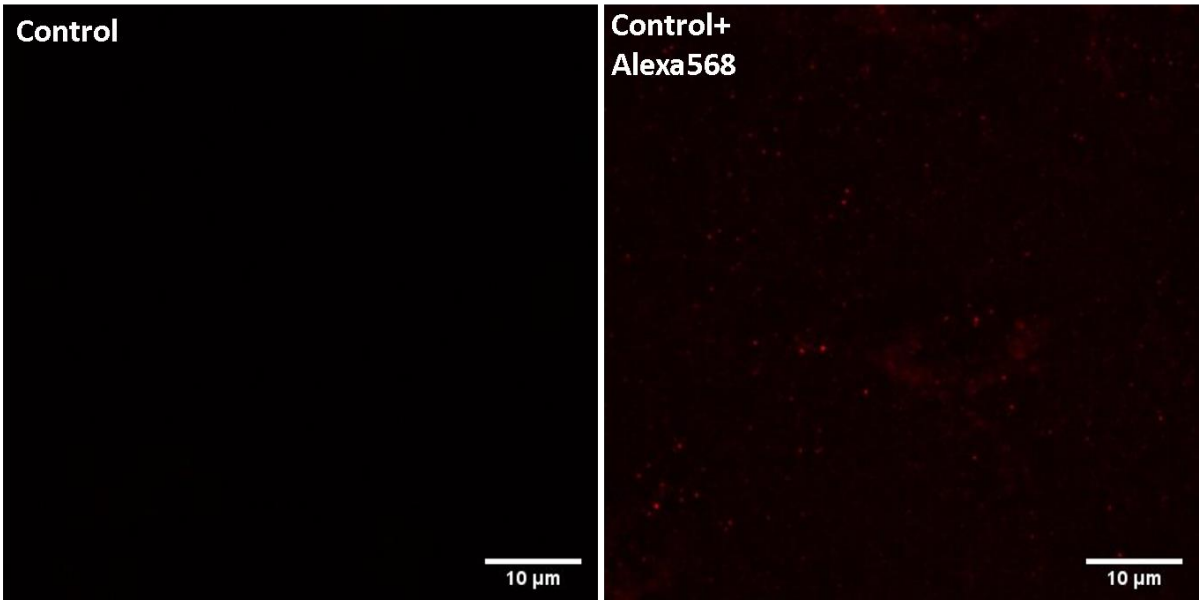

Supplementary Figure 2. The effect of Alexa568 antibody staining on background signal. Slices after culturing for DIV20 with 3,6 x 10^8 vg virus load infected at DIV5. Alexa 568 staining was performed to amplify mCherry signal. Control sample received no treatment. Confocal fluorescence imaging.

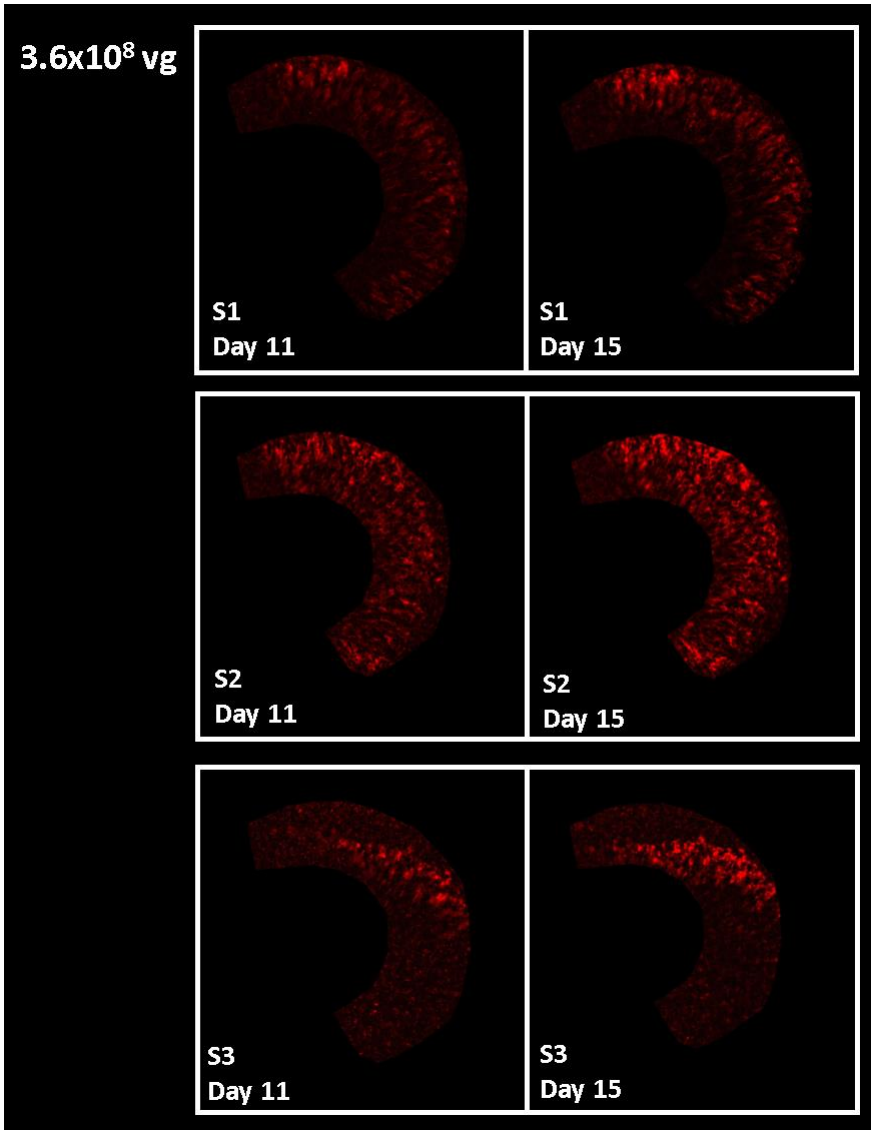

Supplementary Figure 3. Change of hM4D-mCherry expression in ROIs that corresponded to CA1b-CA3b region at 11 (DIV16) and 15 (DIV20) days after DIV5 infection with 3,6 x 10^8 vg. Wide-field fluorescence imaging.

ACKNOWLEDGMENT

Most importantly, I would like to thank research supervisor dr. Urtė Neniškytė and research advisor Lina Saveikytė for help, novel ideas and opportunity to learn from these amazing researchers.

Of course, I would like to say a big thank you for the entire UNL team. I wish everyone could work with such an incredible team of people.

Finally, I would like to thank my partner Viktorija for patience and understanding.